SUPER-RESOLUTION OPTICAL NANOPATTERNING BEYOND THE FAR-FIELD DIFFRACTION LIMIT USING PHOTOCHROMIC MOLECULES AND ABSORBANCE MODULATION OPTICAL LITHOGRAPHY

by

Apratim Majumder

A dissertation submitted to the faculty of
The University of Utah
in partial fulfillment of the requirements for the degree of

Doctor of Philosophy

Department of Electrical and Computer Engineering

The University of Utah

May 2018

The University of Utah Graduate School

STATEMENT OF DISSERTATION APPROVAL

The dissertation of Apratim Majumder

has been approved by the following supervisory committee members:

Rajesh Menon	,	Chair	12/08/2016 Date Approved
Carlos H. Mastrangelo	,	Member	12/08/2016 Date Approved
Ajay Nahata	,	Member	12/08/2016 Date Approved
David Schurig	,	Member	12/08/2016 Date Approved
Ashutosh Tiwari	,	Member	12/08/2016 Date Approved

and by Gianlucca Lazzi , Chair/Dean of the Department/College/School of Electrical and Computer Engineering and by David B. Kieda, Dean of The Graduate School.

ABSTRACT

Following the progress of shrinking down the sizes of integrated circuit elements, optical lithography, which is the state of the art of patterning ever-small structures, has now almost reached its final limit. This limit to the size of the smallest feature that can be patterned using photolithography is imposed by the diffraction limit of light, generally accepted to be about half the wavelength of illumination. Absorbance Modulation Optical Lithography (AMOL) is a technique of super-resolution maskless photolithography with the potential to localize light to sub-diffraction limited spaces. AMOL uses a unique family of organic molecules called photochromes that can switch between two isomeric states based on the wavelength of photon that the states absorb, a long wavelength photon (of wavelength λ_2) and a short wavelength photon (of wavelength λ_1). When a thin layer of this photochromic molecule, is subjected to simultaneous illumination by a focal spot at λ_1 and a ring-shaped spot at λ_2, it is rendered opaque everywhere except at very close to the center of the optical node in the ring shaped λ_2 spot. This competing behavior of the absorbance of the layer to the two wavelengths and the state transitions allows only λ_1 photons to penetrate through the λ_2 node, creating a nanoscale illumination spot, the dimensions of which are far below the diffraction limit. A recording medium placed under this layer, such as photoresist can record this illumination.

In this dissertation, the development of AMOL as a cost effective super-resolution

photolithography process is addressed. Firstly, an improvement to the AMOL process is affected by the removal of a barrier layer that was present in previous demonstrations in between the AML and the photoresist. Secondly, experimental verification of the AMOL feature-scaling trend is presented. Next, a comprehensive model to simulate the AMOL process is constructed using finite element method based full electromagnetic wave solutions. A couple of methods to realize AMOL patterning at very low light intensity levels are also demonstrated with both simulation and experimental verifications. Lastly, an optical system is described that is capable of extending the AMOL process to patterning aperiodic arbitrary features.

To Ma, Babai, and Amma

“The only solutions that are ever worth anything are the solutions that people find themselves.”

– Satyajit Ray

TABLE OF CONTENTS

ABSTRACT iii

ACKNOWLEDGEMENTS x

Chapters

1 INTRODUCTION TO SUPER RESOLUTION LITHOGRAPHY 1

1.1 A Brief History of Lithography 1
1.2 The Diffraction Limit of Light 6
1.3 A Brief Overview of Super-Resolution Optical Microscopic Techniques 8
1.4 Introduction to Super-Resolution Optical Lithographic Techniques 10
1.5 Dissertation Outline 12
1.6 References 20

2 INTRODUCTION TO ABSORBANCE MODULATION OPTICAL LITHOGRAPHY 23

2.1 Description of the AMOL System 23
2.2 Photochromic Molecules Used in AMOL 25
2.3 Literature Survey on AMOL 26
2.4 Advantages of AMOL 26
2.5 References 31

3 BARRIER-FREE ABSORBANCE MODULATION FOR SUPER-RESOLUTION OPTICAL LITHOGRAPHY 33

3.1 Abstract 34
3.2 References and Links 34
3.3 Introduction 35
3.4 Experiments 36
3.5 Conclusion 40
3.6 Acknowledgement 40

4 MODELING ABSORBANCE MODULATION OPTICAL LITHOGRAPHY 41

4.1 Motivation 41
4.2 Background Information 41
4.3 Modeling Approach 44
4.4 References 53

5 ABSORBANCE MODULATION MODELING METHOD 55

5.1 Introduction 55
5.2 Model Construction in COMSOL 55
5.3 Boundary Values 56
5.4 Algorithm 56
5.5 AMOL System Equations 57
5.6 References 62

6 A COMPREHENSIVE SIMULATION MODEL OF THE PERFORMANCE OF PHOTOCHROMIC FILMS IN ABSORBANCE-MODULATION-OPTICAL-LITHOGRAPHY 63

6.1 Abstract 64
6.2 Introduction 64
6.3 Modeling and Simulations 65
6.4 Results 66
6.5 Conclusion 70
6.6 Acknowledgement 70
6.7 References 71
6.8 Supplemental Material 72

7 REVERSE ABSORBANCE-MODULATION-OPTICAL-LITHOGRAPHY FOR OPTICAL PATTERNING AT LOW LIGHT LEVELS 77

7.1 Abstract 78
7.2 Introduction 78
7.3 Simulation Results 80
7.4 Experimental Results 81
7.5 Conclusion 82
7.6 Acknowledgement 82
7.7 References 82
7.8 Supplemental Material 84

8 AMOL AT LOW LIGHT INTENSITY USING QUANTUM YIELD MATCHED PHOTOCHROMES 91

8.1 Introduction 91
8.2 Photochromic Molecules with Better Matched Quantum Yields 91
8.3 Simulation Results 92
8.4 Experimental Results 93
8.5 References 98

9 OPTICAL SETUP FOR PERFORMING TWO-DIMENSIONAL OPTICAL PATTERNING USING AMOL 99

9.1 Introduction 99
9.2 Description of Optical Setup 99
9.3 Three-Axis Scanning Stage 101
9.4 Dichroic Mirror 101
9.5 Optical Vortex 102
9.6 Optical Vortex Formation Using Vortex Phase Plate 103
9.7 Examples of Patterning 105
9.8 Conclusion and Future Work 105
9.9 References 112

ACKNOWLEDGEMENTS

I feel blessed to have been able to undertake a journey such as this, which may well be one of the most memorable, eventful and fulfilling ones of my life. In this regard, I shall always be indebted to the University of Utah and the department of Electrical and Computer Engineering for allowing me to live my dream. My heartfelt gratitude and humblest respects to my doctoral adviser, Professor Rajesh Menon, for allowing me the opportunity to pursue my doctorate studies under his tutelage and guidance, and for providing the most valuable of insights, support, encouragement and much needed leadership, without which success would have been impossible. Also, to the members of my doctoral supervising committee, Dr. Ajay Nahata, Dr. Carlos H. Mastrangelo, Dr. David Schurig, and Dr. Ashutosh Tiwari, I extend my gratitude.

I express my gratitude to my Ma, who has long struggled to give me an able platform from which I have been able to chart my course. She has always encouraged me in all my pursuits. To my dearest Babai, for encouraging me to explore the different faculties in life, and providing guidance and knowledge. To Amma, who I deeply miss at this moment, for all her love and warmth. To you, my love and respects.

I would like to thank my colleagues and labmates, Farhana Masid, Precious Cantu, Peng Wang, Xiaowen Wan, Ganghun Kim, Nabil Mohammad, Bing Shen, and Chaitanya Ullal for their friendship and support at the workplace. Their presence

brought life to the Menon Group. Special thanks to Farhana for being such a close friend and for the sumptuous meals she cooked for me, and for sharing the tough moments we had to grind through when it seemed that nothing in the laboratory ever worked or made sense.

It is a rare fortune to be in a foreign land and still be able to be part of a family, born not out of blood, but spirit. My family here in Salt Lake City consists both of friends old, Niladri and Aishwaryadev, and friends new, Palash da, Sudipta, Dipanjan, Rambo, Sayan, Prateep, Payel, Tinni, and Debolina. Palash da was my host when I first set foot in Salt Lake City and over time has mentored me in various aspects of my life, even as far as teaching me how to drive. With him, Dipanjan, and Rambo, my first roommates, the foundations to a small group of Bengalis was laid that over time grew manifold. The time spent with my last roommates, Aishwaryadev and Prateep, is dear to my heart and to be reminisced for long. Finally, Sudipta is my dearest friend, my closest confidant, and the person with whom I share my most favorite interests. She will always be very special to me.

Finally, I would like to express my gratitude to my school in Kolkata, India, South Point High School, where I spent my formative years, my childhood, and to the teachers there, who instilled in me the interest to pursue higher education and the courage to know. Also, to all my friends in school who will always have the most special place in my heart. I would also like to thanks my relatives for their constant support, love, and good wishes.

These five years have proved to me how the toughest of undertakings are also the most rewarding.

CHAPTER 1

INTRODUCTION TO SUPER RESOLUTION LITHOGRAPHY

It is almost impossible to imagine the present-day world without the immense amount of technology that defines its very existence. Undoubtedly, among all the different inventions of the last few centuries that have shaped this world, one of the most powerful ones is that of the semiconductor. Semiconductor physics and the fruits that it bears in the shape of integrated circuits, micro- and nanotechnology have laid the foundation on which stands today the citadel of modern science. This great triumph of semiconductor technology is attributed to man's ability to understand, control, and manipulate things at a scale so small that it is imperceptible to his senses. Richard Feynman in 1959 grasped and elucidated the importance of this problem in his lecture "There's plenty of room at the bottom" [1] and since then science has not deterred until that room has been filled to the brim.

1.1 A Brief History of Lithography

1.1.1 Lithography

One of the primary processes by which these integrated circuits and their family of similar devices are fabricated is called lithography. However, in contrast to how modern the science to which this term contributes these days, is how ancient the origin of the term really is. The word "lithography" comes from the Ancient Greek word

"lithos" meaning "stone" and "graphein" meaning "to write" and originally referred to a technique of printing [2]. It was a method by which prints could be made onto paper or similar smooth surfaces from a block of stone or metal plate that contained the master. The invention of this printing technique dates back to 1796 and it is credited to Alois Senefelder, a German author and actor [3]. This was a method of transferring and replicating images and recording patterns and, in essence, the use of lithography in the context of the semiconductor industry has remained much the same. Coincidentally, it may be observed that the invention of printing and the printing press in the 14th – 15th century was as important as the invention of the semiconductor to this day and age. However, when mentioned solely in the latter context, lithography strictly refers to the method of recording and replicating patterns used to fabricate integrated circuits onto silicon and metallic substrates. As such, the scale in which these patterns exist lends the prefixes "micro-" and "nano-" to the term and going forward we shall concern ourselves with the science of micro- and nanolithography.

The technique by which micro- and nanolithography is carried out involves the use of light to record patterns and images onto photosensitive substances. It is similar to the method by which light with spatial information is recorded onto photosensitive media to produce photographs. The science of photography, which becomes relevant to this discussion now due to the involvement of light in the lithographic process, itself dates as far back as the 17th century. The pioneering work of a number of scientists must be mentioned, the combined effort of whom led to the invention of photography – Robert Boyle, for his discovery of the photoreactivity of silver nitrate, the photoreactive compound used in primitive photographic plates; Thomas Wedgewood for lending practicality to this discovery; and finally Nicephore Niepce and Louis

Daguerre for ultimately perfecting the technique of photography to produce the world's first photograph in 1839 or, as it was known back then, the daguerreotype [4]. In his light-exposure-and-etch-based technique of lithography, a close relative of the photographic process, Niepce used Bitumen of Judea, a natural asphalt that became less soluble upon exposure to light. This was the world's first photoresist. At this point, it becomes more appropriate to substitute the prefix "photo-" to the term in order to acknowledge the role of light in the process and concern ourselves with the discussion of photolithography. The invention of the transistor in 1947 [5] and subsequently the integrated circuit in 1958 gave impetus to the growth of microfabrication and photolithography was the science that enabled it [6]. Photoresists and optical systems that could efficiently expose and record patterns in them to be later etched into silicon substrates became commercial. Research efforts were focused on light sources to improve imaging and in the years that followed, until today, photolithography assumed the role of the workhorse of the semiconductor industry.

1.1.2 The Lithographic Process

The general process of photolithography involves the recording of a pattern in a photosensitive chemical compound called the photoresist. Subsequently, transfer of this pattern to a final recording and preserving layer is achieved by means of etching. The general steps involved are illustrated in Fig. 1.1. A substrate, usually a silicon wafer by itself or a silicon wafer with a thin layer of a functional layer of metal like gold or aluminum in which the final pattern is to be preserved, is first cleaned and prepared as shown in Fig. 1.1(a). On top of this layer, a layer of the photoresist is applied. The photoresist is selectively irradiated by light containing some predefined pattern. Such spatially patterned light can be created using photomasks as well as

using maskless techniques. These will be described in the following section. Selectively exposing regions of the photoresist to light causes a change in the chemistry of those regions. For positive-tone photoresists the exposed regions become more soluble in a developer compared to the nonexposed regions while in negative-tone photoresists, the effect is reversed. Either way, once treated with developer, the photoresist is patterned with the spatial pattern that existed in the incident illumination. Following this step, the photoresist can now act as a mask to protect the functional layer underneath as shown in Fig. 1.1(b). The sample may now be subjected to various etching techniques that etch into the functional layer in the regions not protected by the photoresist mask, thereby transferring the pattern from the photoresist. This method is called etching. An alternative way of pattern transfer may be performed by coating the substrate with the functional layer at this stage instead of at the beginning and then stripping away the photoresist while selectively lifting off regions of the functional layer. This method is called lift-off. Finally, the photoresist may be removed completely using photoresist solvents such as acetone and isopropanol.

1.1.3 Creating the Spatial Light Pattern

The spatial pattern in the illumination that is used to selectively expose the photoresist layer can be achieved by two ways: (a) using a mask to selectively block the light thereby imparting a spatial pattern to it and (b) using a maskless spatial patterning scheme.

1.1.3.1 Mask-based Photolithography

This method uses a mask that consists of a fused silica (glass) substrate with predefined patterns of an opaque material such as chrome. The incident illumination is blocked by the chrome pattern allowing only the light elsewhere to pass through the glass and selectively expose the photoresist. Thus, the pattern on the mask is imaged on to the photoresist. This scheme is shown in Fig 1.2(a).

1.1.3.2 Maskless Photolithography

There may be a variety of ways to impart spatial pattern in an otherwise uniform illumination with a plane wavefront without the use of a mask. One of the simplest is to allow two plane waves of the illumination to interfere at the surface of the photoresist. This interference of light creates alternating regions of high and low light intensities called interference fringes that can then expose the photoresist only under the high intensity fringes. This scheme is shown in Fig 1.2(b).

1.1.4 Projection Optical Lithography

In the semiconductor industry, the mask-based photolithography approach has served for decades. This process is utilized in an optical stepper and scanner tool where the image in the mask is demagnified onto the surface of the photoresist using powerful optics. This is called projection photolithography. As Fig 1.3 illustrates, the original image of the chrome-and-glass mask is reduced by projecting it through lens-based optics on to the surface of the photoresist. One major drawback of this method is that the original pattern is fixed in the mask that may only be projected onto the sample. If a change in the design is desired a new mask must be fabricated. This incurs significant overhead and increases cost of the overall process. Hence, it is

undesirable. Since the concept of projection and lens-based demagnification of an object has been introduced, the concept of the diffraction limit of light will be discussed in the next section.

1.2 The Diffraction Limit of Light

1.2.1 Definition of the Diffraction Limit

As described in the previous section, the most prevalent method in the semiconductor industry to perform photolithography is to adopt the lens-based technique of image projection. This method enables the optical scanners to demagnify the original mask pattern while projecting the image onto the photoresist layer. This ability of optical systems to shrink down patterns is vital to the growth of the semiconductor industry since smaller feature sizes directly correlate to a larger number of components (transistors, etc.) per unit area, lower power consumption, faster performance, and so forth. However, optical systems cannot focus light to infinitely small points. There is a fundamental limit imposed by the laws of optics on the smallest size of the focal spot that can be produced by any lens-based system. This phenomenon, a direct result of the diffraction of light and discovered by Ernst Abbe in 1873, is termed the diffraction limit [7]. This condition states that the size of the smallest spot ($\boldsymbol{d}$) that can be produced by any optical system is given by

$$\boldsymbol{d} = \frac{\boldsymbol{\lambda}}{\boldsymbol{2NA}} = \frac{\boldsymbol{\lambda}}{\boldsymbol{2nsin\theta}} \qquad (\mathbf{1.1})$$

where $\boldsymbol{\theta}$ is the half angle of illumination, $\boldsymbol{n}$ the refractive index of the surrounding medium, $\boldsymbol{\lambda}$ is the wavelength of illumination, and $\boldsymbol{NA}$ is the numerical aperture of the

system. This condition is illustrated in Fig 1.4.

1.2.2 Impact of the Diffraction Limit to Photolithography

The diffraction limit imposes a fundamental restriction on the size of the smallest feature that can be patterned using lens-based optics. In keeping with that restriction, the ways by which equation 1.1 can be used to shrink down feature sizes is either by employing illumination sources with smaller wavelengths or by increasing the NA of the system. Both of these approaches have been adopted in the semiconductor industry. Fig 1.5 shows how the reduction is affected in the semiconductor industry by reducing the wavelength of the illumination system. Currently 193 nm technology is in use [8, 9]. The projected use of Extreme Ultraviolet (EUV) at 13.5 nm technology is yet to be realized because of the high expense and complexities involved. EUV is readily absorbed in air and fused silica and hence requires cumbersome and expensive vacuum systems and optics for it to succeed. This has been a roadblock in lowering the illumination wavelength past the Deep Ultraviolet (DUV) technology at 193 nm.

Thus, in order to continue scaling down features without employing EUV, a number of techniques have been invented in the semiconductor industry that can affect feature size and spacing reduction at lower complexities [10]. The most successful is the method of double patterning. Different approaches to this include the Litho-Etch-Litho-Etch (LELE) [11], the Litho-Freeze [12], and the Self-Aligned Double Patterning (SADP) scheme [13]. These have been illustrated in Fig 1.6. The LELE process requires subsequent etch steps after each lithography step and the final pattern once etched has separation below the diffraction limit even though the individual lithography steps do not require this condition to be met. The Litho-Freeze process chemically “freezes” the photoresist after the first lithographic exposure so

that it is not affected by the second exposure. The SADP process is a bit more complex and requires additional processing steps. Following the first exposure, a masking material known as the spacer is deposited and etched to create sidewalls on the resist profile. The resist is then removed and finally the spacers are used to etch into the functional layer.

The ideal technique would be to use Double Exposures (DE) where two lithographic exposures can be performed successively while translating the sample and then performing only one final etch step. Currently, this is not possible in the industry because DE materials exhibiting sufficient nonlinearity in their exposure process do not exist. If one were to attempt DE in conventional photoresists, the two exposures separated by a spacing less than the diffraction limit would simply add up, resulting in complete overexposure of the photoresist and complete resist removal once developed. DE are promised by methods of super resolution lithography and will be discussed in the following sections. They are inherently inspired by the number of super-resolution optical microscopic techniques that have recently surfaced and become well recognized in the past couple of decades. The next section presents a brief description of these methods.

1.3 A Brief Overview of Super-Resolution Optical Microscopic Techniques

Recently the diffraction limit has been circumvented in optical microscopy. Since photolithography and optical microscopy are very similar processes, differing only in the direction of light travel (for microscopy it is from the sample to the optics and for lithography it is from the optics to the sample), it is worthwhile to briefly discuss the techniques by which the feat was achieved.

1.3.1 Breaking the Diffraction Limit in Optical Microscopy

A number of techniques have been developed recently by which features much smaller than the diffraction limit can be resolved using optical microscopy. These include Stimulated-Emission-Depletion (STED) microscopy [14], Photo-Activated-Localization Microscopy (PALM) [15], and Stochastic-Optical-Reconstruction Microscopy (STORM) [16]. Each of these techniques are able to achieve resolution many times lower than what the diffraction limit dictates. PALM and STORM mainly use low photon excitation and subsequent localization of fluorophores to achieve this feat. The 2014 Nobel Prize in Chemistry was awarded to William H. Moerner for his discovery of controlled photo-switching of single molecule fluorescent proteins, the fluorescence of which could be turned on and off at will, Eric Betzig for the discovery of time-separated fluorescence that when multiplexed allows super-resolution imaging, and to Stefan W. Hell for demonstrating the idea of forcefully depleting fluorescence from the periphery of the excitation spot thereby allowing the imaging of features far beyond the diffraction barrier [17-19]. The technique of STED is described in the following section since the work in this dissertation is inspired primarily by STED.

1.3.2 Stimulated-Emission-Depletion (STED) Microscopy

In conventional fluorescence microscopy, a cluster of fluorophores is illuminated by an excitation beam spot that is diffraction limited. This causes the fluorophores to emit from the entire region that was under the excitation spot. Hence, the emitted spot is also diffraction limited. However, in STED microscopy, after the excitation step, a red-shifted ring-shaped spot called the STED beam illuminates the fluorophores before the fluorescence can take place. All the fluorophores under the

STED beam are forcibly depleted and returned to the ground state leaving only the ones at the dark node of the ring-shaped STED beam to fluoresce. This is illustrated in Fig. 1.7. It can be seen that the dimensions of the fluorescence spot in STED is not determined by the diffraction limit anymore since both the excitation and the STED beams are diffraction limited but the dimensions of the final fluorescence is not. This is controlled by the ratio of the intensities of the two beams. It can be understood that increasing the intensity of the STED beam converts more and more fluorophores at the vicinity of the node to deplete, thereby shrinking the dimension of the emission spot. STED offers an increase in resolution of at least an order of magnitude at minimum, improving from the confocal fluorescence microscope resolution of 200 nm down to 20 nm [20-27] and has even been demonstrated to reach up to 6 nm [28].

1.4 Introduction to Super-Resolution Optical Lithography Techniques

The approach of microscopy to breaking the diffraction limit has been emulated in the field of photolithography. This has led to the development of a number of innovative techniques that have been shown capable of patterning features with dimensions smaller than what is allowed by the diffraction limit.

1.4.1 Techniques for Breaking the Diffraction Limit in Photolithography

A number of techniques have been developed that aim to break the diffraction limit for photolithography, as described in this section. One such is by the use of multiphoton absorption of pulsed 800 nm light to initiate photopolymerization followed by single-photon absorption at the same wavelength to induce depolymerization reaction at the periphery of the first polymerization step. The

resulting final feature dimension was shown to be about 40 nm or, in this case, $\lambda/20$ [30]. However, this technique has a number of drawbacks. Firstly, it has to employ a specialized resin capable of exhibiting the required photopolymerization and subsequent depolymerization reactions, and thus conventional industry standard photoresists cannot be used. Secondly, multiphoton polymerization involves both the use of long near infrared (NIR) wavelengths like 800 nm and extremely high light intensity, which is undesirable. Another technique reported the use of two wavelengths, where single photon absorption to the longer wavelength (473 nm) initiated polymerization while absorption at the shorter wavelength (364 nm) initiated depolymerization of the resin. A focused spot of the polymerizing beam and a ring of the inhibiting beam was employed to pattern features with dimensions below the diffraction limit. Feature sizes about 64 nm were reported [31]. This method also involves the use of a specific resin and, as a result, it cannot be directly integrated into traditional lithographic systems. In comparison to the two techniques mentioned above, Absorbance Modulation Optical Lithography, which was developed about the same time [32-38], has a number of advantages. A brief overview of the method is presented here and will be dealt with in detail in the next chapter.

1.4.2 Overview of Absorbance Modulation Optical Lithography

Absorbance Modulation Optical Lithography (AMOL) employs the use of a thin layer of spectrally selective, reversible photochromic molecules called the absorbance modulation layer (AML). This layer is rendered transparent to a short wavelength (λ_1, usually ~ 325 nm) upon absorbing photons at that wavelength and rendered opaque to it by absorbing photons at a longer (λ_2, 633-647 nm) wavelength. A focal spot at the

shorter wavelength (hereby referred to as the exposing beam), when collocated with a ring-shaped spot at the longer wavelength (hereby referred to as the confining beam), allows the formation of a subdiffraction aperture directly under the peak of the exposing beam whereby λ_1 photons can penetrate the film. A recording medium like photoresist when placed under the AML, can now be exposed by photons of λ_1 and the exposed region is confined to dimensions below the diffraction limit. Feature sizes as small as 30 nm, corresponding to $\lambda/10$, were reported [38-40]. The obvious advantages of AMOL lie in the fact that the recording medium, being separate from the functional medium responsible for subdiffraction light confinement, allows the use of any type of industry standard photoresist as well as the use of low light intensities since all absorption is single photon. The schematic of AMOL is shown in Fig. 1.8.

1.5 Dissertation Outline

The primary goal of this dissertation is to demonstrate the viability of AMOL to patterning features below the diffraction limit and to develop it as an industry alternative low-cost super-resolution lithography process at low light intensities. In Chapter 1, an overview and historical perspective of the lithographic process is presented. In Chapter 2, the motivation of this work is discussed along with an overview of the AMOL process. The structures of the photochromic molecules used in AMOL are also introduced here. Chapter 3 describes a process improvement to AMOL whereby lithographic patterning of subdiffraction patterns are successfully demonstrated without a barrier layer. This chapter also provides experimental demonstration of the AMOL feature-scaling trend. Chapter 4 describes the approach adapted to constructing a finite-element method-based full electromagnetic wave solution model that can effectively simulate the AMOL process. Chapter 5 provides

further discussion on the model construction with specific mathematical formulations for the AMOL system equations. Chapter 6 presents the results of the simulations and elucidates the effect of different illumination and material parameters on the AMOL process. Chapters 7 and 8 describe two techniques of performing AMOL at low light intensities. In Chapter 7, this is achieved by reversing the illumination scheme to take advantage of the mismatch in the quantum yield of the photoreaction. In Chapter 8, descriptions of photochromes with better matched quantum yields are presented. Simulation and experimental results are demonstrated in both cases. Lastly, Chapter 9 presents the description of an optical system that is capable of extending the AMOL process to patterning aperiodic arbitrary features.

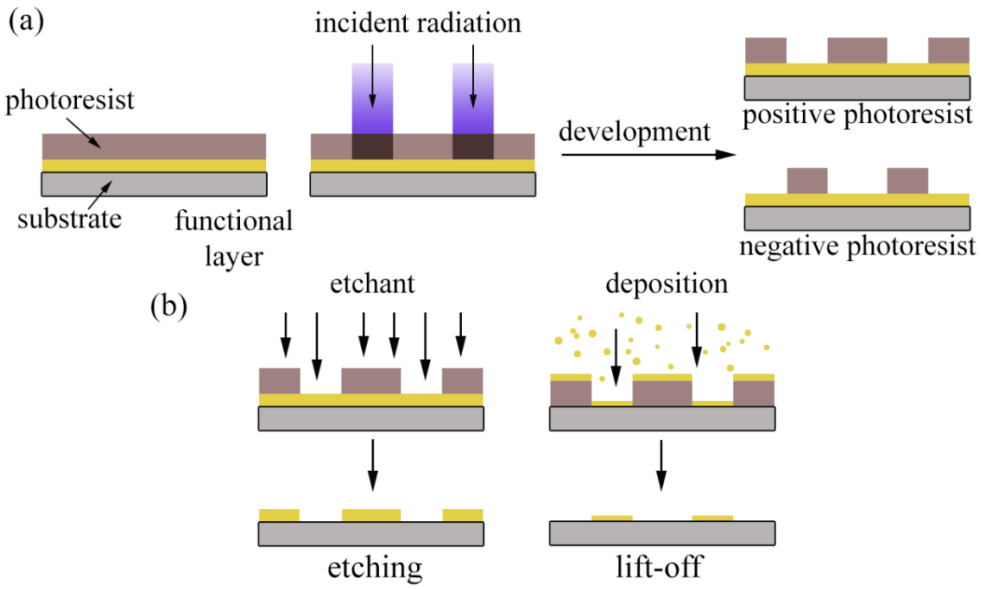

Figure 1.1: Schematic of the general photolithographic process. (a) The photolithographic process shows the recording of a spatial pattern in incident radiation into photoresist and subsequent photoresist patterns based on their types. (b) General etch processes that lead to the transfer of the photoresist pattern to the functional layer.

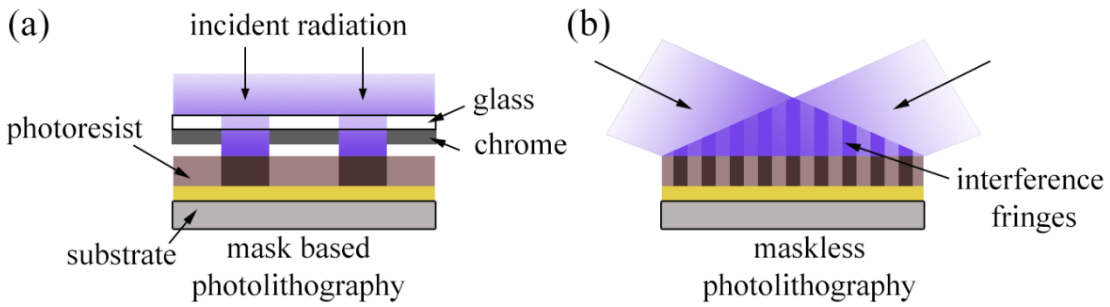

Figure 1.2: Different techniques of creating spatial patterns in light. (a) The mask-based approach involves the use of a mask with a predetermined image defined by chrome patches on the glass fused silica surface (b) Means of generating maskless spatial light patterning by creating interference fringes at the plane of interference of two plane waves from opposite directions.

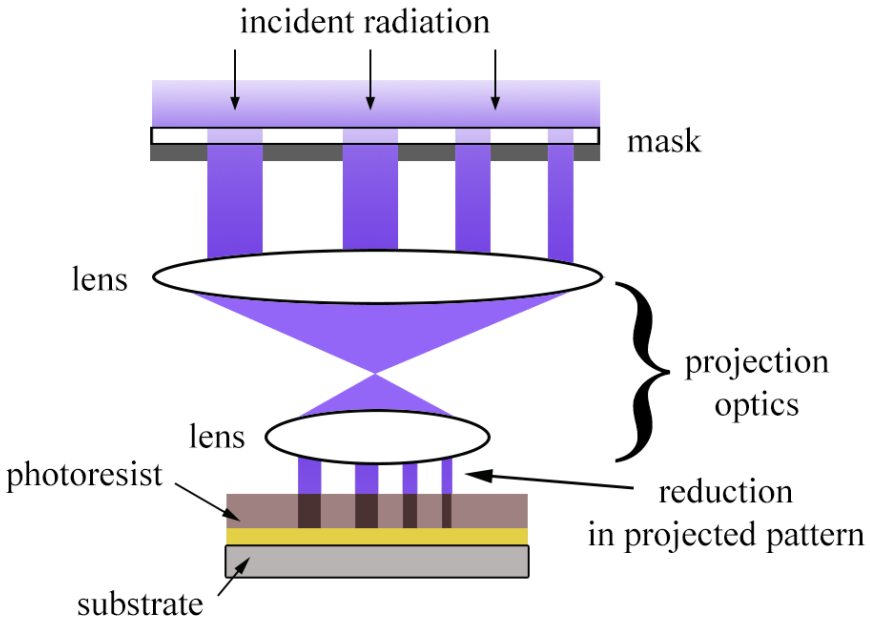

Figure 1.3: Schematic of projection photolithography. The pattern in the mask is projected to a lens-based system onto the plane of the photoresist layer in the sample.

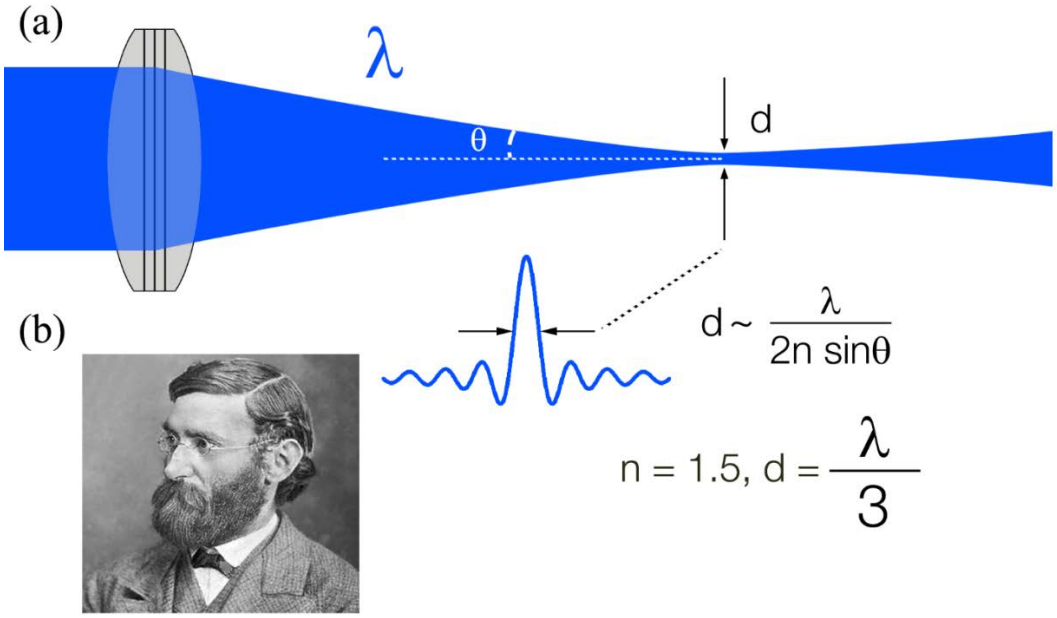

Figure 1.4: Diffraction limit of light. (a) The definition of the diffraction limit of light. (b) Ernst Abbé.

(a)

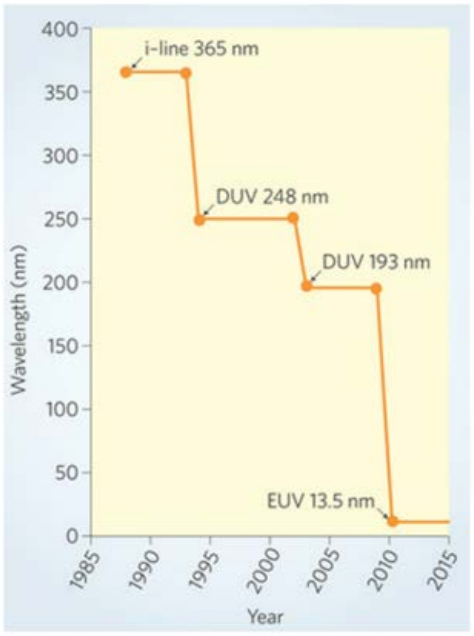

(b)

Figure 1.5: Feature scaling and lithographic scanner. (a) Feature scaling versus wavelength reduction in the semiconductor industry [8]. (b) A DUV scanner.

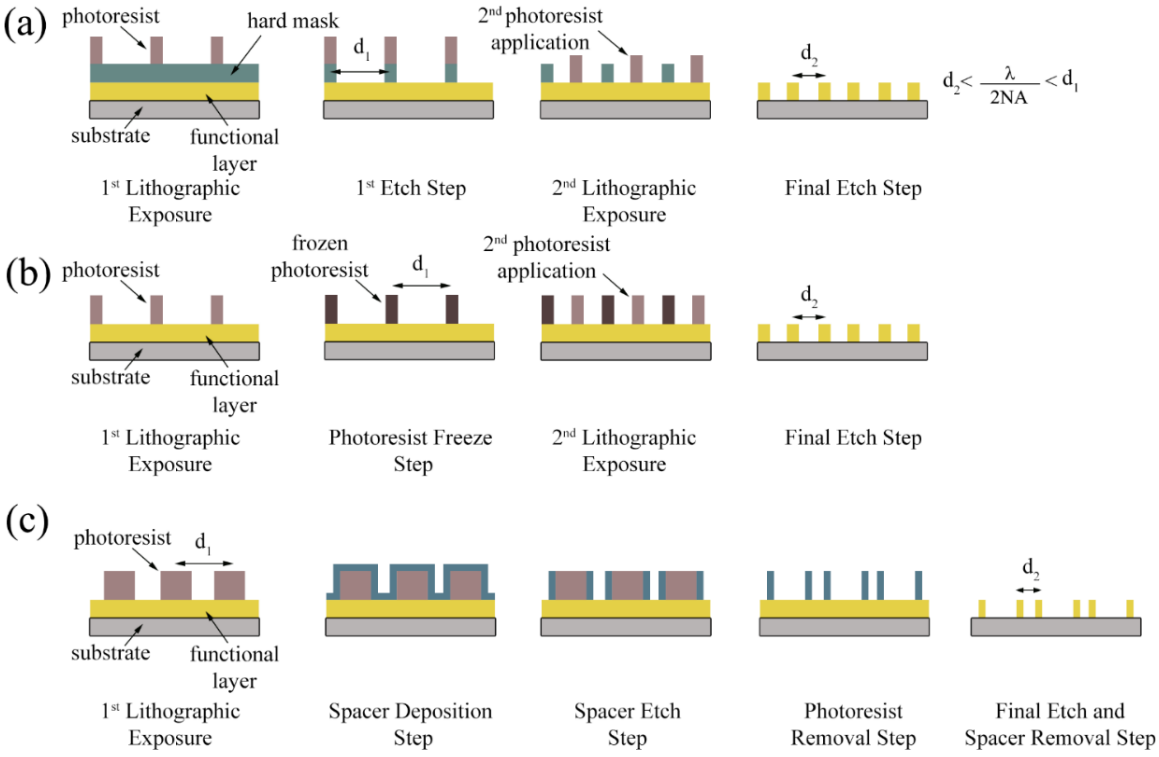

Figure 1.6: Lithographic processes. (a) Litho-Etch-Litho-Etch (LELE) process. (b) Litho-Freeze process. (c) Self-Aligned Double Patterning (SADP) process.

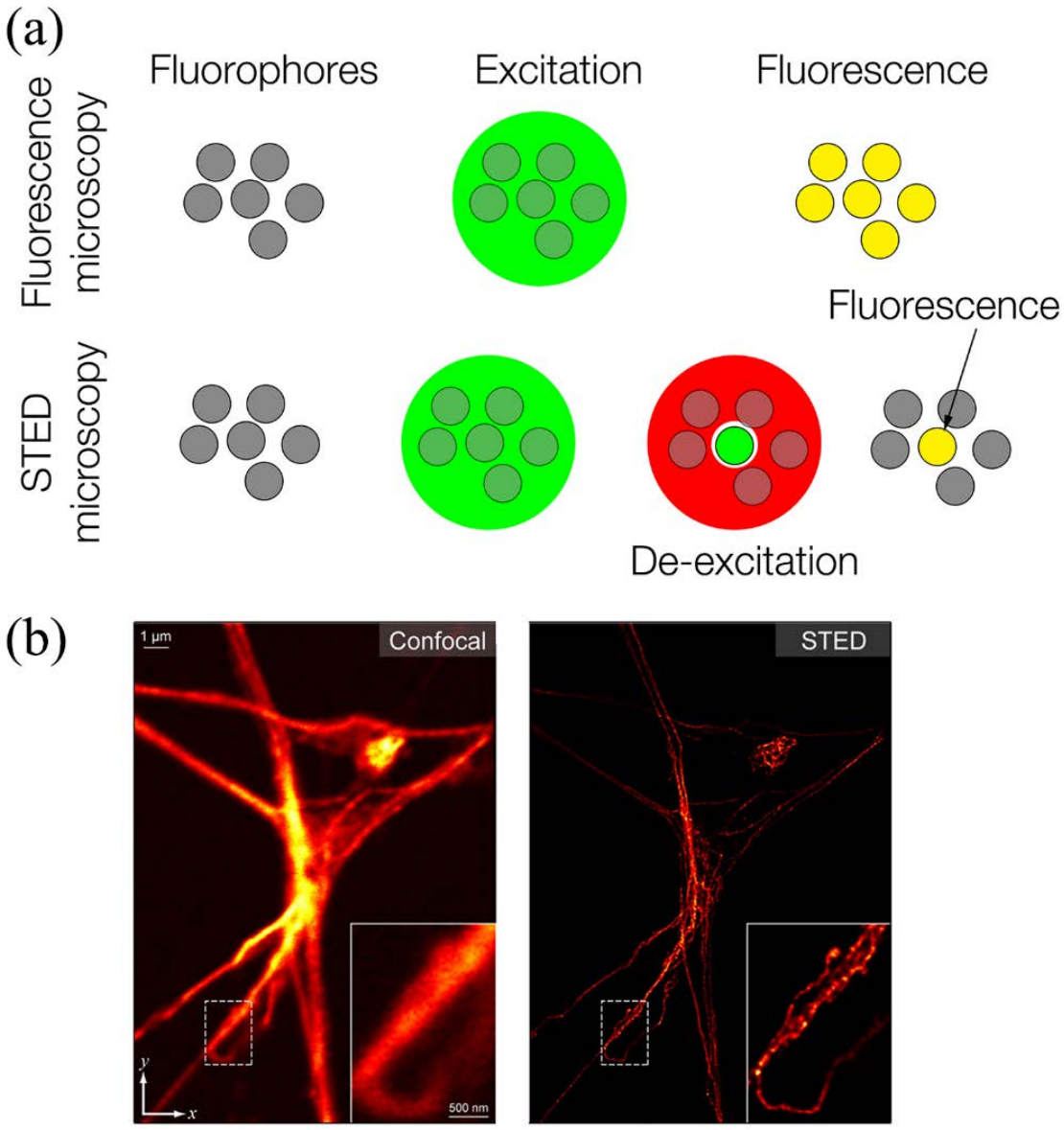

Figure 1.7: STED microscopy. (a) Schematics of conventional fluorescence and STED microscopy. (b) Resolution enhancement in the image of a neuron by STED microscopy compared to confocal [29].

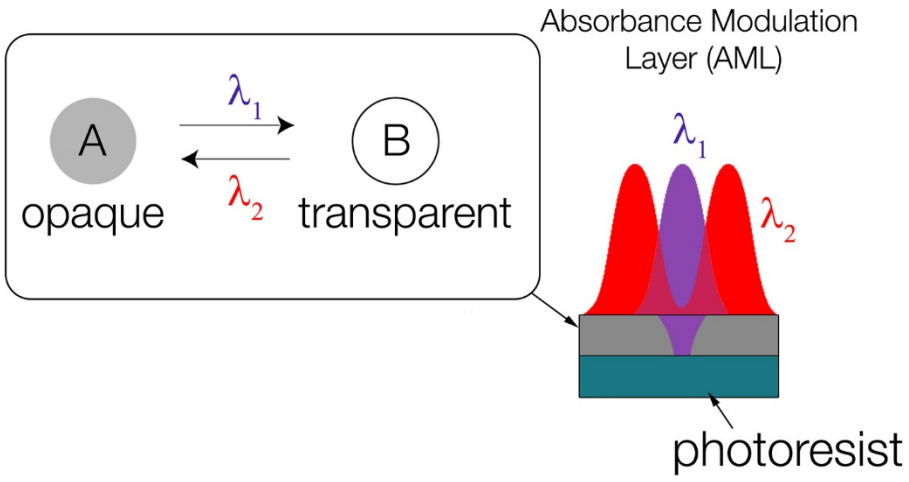

Figure 1.8: Schematic of Absorbance Modulation Optical Lithography (AMOL).

1.6 References

1. R. P. Feynman, "There's plenty of room at the bottom (data storage)," *J. Microelectromech. Sys.*, vol. 1, no. 1, pp. 60-66, Mar. 1992.

2. P. Weaver, *The Technique of Lithography*, London, B. T. Basford, 1964, pp. 49.

3. P. B. Meggs, *A History of Graphic Design*, 5th ed. John Wiley & Sons, 1998, pp. 146.

4. J. Hannavy, *Encyclopedia of Nineteenth-Century Photography*, 1st ed. Routledge, 2007, pp. 365.

5. W. Brinkman, D. Haggan, and W. Troutman, "A history of the invention of the transistor and where it will lead us," *IEEE J. Solid-State Circuits*, vol. 32, no. 12, Dec. 1997, pp. 1858-1865.

6. M. Riordan and L. Hoddeson, *Crystal Fire: The Invention of the Transistor and the Birth of the Information Age*, 1st ed. New York, W.W. Norton & Company, 1997, pp. 103.

7. E. Abbé, "Beitragezurtheorie des mikroskops und der mikroskopischenwahrnehmung," *Arch. Mikrosk. Anat. Entwichlungsmech* vol. 9 no. 1, Mar. 1873, pp. 413-418.

8. C. Wagner and N. Harned, "EUV lithography: Lithography gets extreme," *Nat. Phot.*, vol. 4, no. 1, Jan. 2010, pp. 24-26.

9. S. Wurm, "EUV lithography development and research challenges for the 22 nm half-pitch," *J. Photopoly. Sci. Technol.*, vol. 22, no. 1, Jul. 2009, pp. 31-42.

10. P. Zimmerman, "Double patterning lithography: Double the trouble or double the fun?" *SPIE Newsroom*, Jul. 2009, pp. 1-3. DOI:10.1117/2.1200906.1691.

11. M. Drapeau, V. Wiaux, E. Hendrickx, S. Verhaegen, and T. Machida, "Double patterning design split implementation and validation for the 32nm node," *Proc. SPIE*, vol. 6521, Mar. 2007, pp. 652109. DOI:10.1117/12.712139.

12. M. Hori, T. Nagai, A. Nakamura, T. Abe, G. Wakamatsu, T. Kakizawa, Y. Anno, M. Sugiura, S. Kusumoto, Y. Yamaguchi, and T. Shimokawa, "Sub-40nm half-pitch double patterning with resist freezing process," *Proc. SPIE*, vol. 6923, Mar. 2008, pp. 69230. DOI:10.1117/12.772403.

13. W. Shiu, H. Liu, J.Wu, T. Tseng, C. Te Liao, C. Liao, J. Liu, and T.Wang, "Advanced self-aligned double patterning development for sub-30-nm DRAM manufacturing," *Proc. SPIE*, vol. 7274, Mar. 2009, pp. 72740E-1-7.

14. S. W. Hell and J. Wichmann, "Breaking the diffraction resolution limit by stimulated emission: Stimulated-emission-depletion fluorescence microscopy,"

Opt. Lett., vol. 19, no. 11, Jun. 1994, pp. 780–782.

15. E. Betzig, J. K. Trautman, T. D. Harris, J. S. Weiner, and R. L. Kostelak, "Breaking the diffraction barrier - optical microscopy on a nanometric scale," *Science*, vol. 251, no. 5000, Mar. 1991, pp.1468–1470.

16. M. Rust, M. Bates, and X. Zhuang, "Sub-diffraction-limit imaging by stochastic optical reconstruction microscopy (STORM)," *Nat. Methods*, vol. 3, no. 10, Aug. 2006, pp. 793–796.

17. I. Sample, "Nobel prize for chemistry awarded to trio for pioneering microscope work," *The Guardian*, Oct. 2014.

18. R. van Noorden, "Nobel for microscopy that reveals inner world of cells," *Nat. News*, Oct. 2014.

19. S. Mirsky, "2014 Nobel Prize in Chemistry," *Scientific American*, Oct. 2014.

20. B. Harke, J. Keller, C. K. Ullal, V. Westphal, A. Schönle, and S. W. Hell, "Resolution scaling in STED microscopy," *Opt. Exp.*, vol. 16, no. 6, Mar. 2008, pp. 4154-4162.

21. P. N. Hedde, R. M. Dörlich, R. Blomley, D. Gradl, E. Oppong, A. C.B. Cato, and G. U. Nienhaus, "Stimulated emission depletion-based raster image correlation spectroscopy reveals biomolecular dynamics in live cells," *Nat. Communicat.*, vol. 4, no. 2093, Jun. 2013, pp. 1-8. DOI:10.1038/ncomms3093.

22. L. Lanzanó, *et al.*, "Encoding and decoding spatio-temporal information for super-resolution microscopy," *Nat. Communicat.*, vol. 6, no. 6701, Apr. 2015, pp. 1-9. DOI:10.1038/ncomms7701.

23. J. Hanne *et al.*, "STED nanoscopy with fluorescent quantum dots," *Nat. Communicat.*, vol. 6, no. 7127, May, 2015, pp. 1-6. DOI:10.1038/ncomms8127.

24. T. Tony Yang *et al.*, "Superresolution pattern recognition reveals the architectural map of the ciliary transition zone," *Scientific Reports*, vol. 5, no. 14096, Sep. 2015, pp. 1-13. DOI:10.1038/srep14096.

25. I. C. Hernandez *et al.*, "Two-photon excitation STED microscopy with time-gated detection," *Scientific Reports*, vol. 6, no. 19419, Jan. 2016, pp. 1-9. DOI:10.1038/srep19419.

26. G. Vicidomini, G. Moneron, K. Y. Han, V. Westphal, H. Ta, M. Reuss, J. Engelhardt, C. Eggeling, and S. W. Hell, "Sharper low-power STED nanoscopy by time gating," *Nat. Methods*, vol. 8, Jun. 2011, pp. 571-573. DOI:10.1038/nmeth.1624.

27. K. I .Willig, B. Harke, R. Medda, and S. W. Hell, "STED microscopy with continuous wave beams," *Nat. Methods*, vol. 4, Oct. 2007, pp. 915-918.

DOI:10.1038/nmeth1108.

28. E. Rittweger, K. Y. Han, S. E. Irvine, C. Eggeling, and S. W. Hell, "STED microscopy reveals crystal colour centres with nanometric resolution," *Nat. Phot.*, vol. 3, Feb. 2009, pp. 144-147.

29. U. Deffke, R. Medda, D. Wildanger, and L. Kastrup, "Outsmarting optical boundaries," *Official website of the Max Planck Gesellschaft*, 2009, pp. 75-81.

30. L. Li, R. R. Gattass, E. Gershgoren, H. Hwang, and J. T. Fourkas, "Achieving λ/20 resolution by one-color initiation and deactivation of polymerization," *Science*, vol. 324, no. 5929, May, 2009, pp. 910-913.

31. T. F. Scott, B. A. Kowalski, R. R. McLeod *et al*,. "Two-color single-photon photoinitiation and photoinhibition for subdiffraction photolithography," *Science*, vol. 324, no. 5929, May, 2009, pp. 913-917.

32. R. Menon and H. I. Smith, "Absorbance-modulation optical lithography," *J. Opt. Soc. Am. A*, vol. 23, no. 9, Sep. 2006, pp. 2290-2294.

33. R. Menon, H-Y Tsai and H. I. Smith, "Patterning and imaging at the nanoscale with far-field optics via absorbance modulation," *Photonic Metamaterials: From Random to Periodic, OSA Technical Digest*, Optical Society of America, Jackson Hole, Wyoming United States, June 2007, pp. WA3. DOI:10.1364/META.2007.WA3.

34. R. Menon, H-Y Tsai, and S. W. Thomas III, "Far-field generation of localized light fields using absorbance modulation," *Phys. Rev. Lett.*, vol. 98, no. 043905, Jan. 2007, pp. 043905-1-4. DOI:10.1103/PhysRevLett.98.043905.

35. H-Y. Tsai, G. M. Wallraff, and R. Menon, "Spatial-frequency multiplication via absorbance modulation," *Appl. Phys. Lett.*, vol. 91, no. 9, Aug. 2007, pp. 094103-1-4. DOI:10.1063/1.2775092.

36. H-Y. Tsai, H. I. Smith, and R. Menon, "Reduction of focal-spot size using dichromats in absorbance modulation," *Opt. Lett.*, vol. 33, no. 24, Dec. 2008, pp. 2916-2918. DOI:10.1364/OL.33.002916.

37. H-Y. Tsai, E. E. Moon, and R. Menon, "Far-field optical imaging at the nanoscale via absorbance modulation," *Novel Techniques in Microscopy, OSA Technical Digest*, Vancouver, Canada, April 2009, pp. NMA2-1-3.

38. T. L. Andrew, H-Y. Tsai, and R. Menon, "Confining light to deep sub-wavelength dimensions to enable optical nanopatterning," *Science*, vol. 324, no. 5929, May, 2009, pp. 917-921.

CHAPTER 2

INTRODUCTION TO ABSORBANCE MODULATION OPTICAL LITHOGRAPHY

Absorbance Modulation Optical Lithography (AMOL) is a maskless lithography technique with the ability to pattern features beyond the diffraction limit. It was first invented by Menon et al. at the Research Laboratory of Electronics (RLE) at the Massachusetts Institute of Technology (MIT) and was subsequently developed at the University of Utah. This chapter provides an introduction, overview, and background of AMOL and its developments with descriptions to the challenges that are addressed in this dissertation.

2.1 Description of the AMOL System

The inspiration for the AMOL technique comes from the super-resolution nanoscopy technique of STED microscopy as described in the previous chapter. In STED, an excitation beam and a depletion beam are used in conjunction to limit the region from which fluorescence is emitted in a cluster of fluorophores. The resulting spot is smaller than what the diffraction limit of light would allow in a conventional system. AMOL uses a similar philosophy. The role, equivalent to that played by the fluorophores in STED, is played by photochromic molecules in AMOL. Photochromic molecules have the ability to switch between two states based on the wavelength of illumination. This is shown in Fig. 2.1. This photochromic state transition is brought

about by two wavelengths. One of them is a short wavelength (λ_1, usually ~ 325 nm as is used in the experiments in this dissertation) and the other is a long wavelength (λ_2, 633-647 nm, 647 nm is used for all experiments described in this dissertation). Let these two states be called the open and the closed states (O and C as labeled in Fig. 2.1). The reason for this nomenclature will be described in the following section, which deals with the detail of the chemistry of the photochromic molecules. State C absorbs λ_2 to convert to state O. State O, similarly, absorbs λ_1 to convert to state C. In addition, state C is transparent to λ_1 while state O is opaque to it. A thin film of these molecules is prepared, usually by dissolving them in a polymer and solvent. This film is called the absorbance modulation layer (AML). Now, if a focal spot at λ_1 is collocated with a ring-shaped spot at λ_2, akin STED, the region of the AML directly underneath the peak of λ_1 will convert to the C state and become transparent to λ_1. The surrounding regions absorb λ_2 photons, remain in state O, and are opaque to λ_1. Therefore, λ_1 photons can penetrate through an extremely narrow aperture created in the AML and reach the other side. If one were to place a recording medium like photoresist under the AML, one could expose the photoresist with a point spread function (PSF) of λ_1 that is much smaller than the diffraction limit. It is important to note that the spatial patterns in the two wavelengths, namely the focal spot and rings are diffraction limited but the PSF that penetrates through the AML is governed by the photochemistry of the layer and is thus inherently able to circumvent the diffraction limit. Therefore, using the principle of AMOL, one can create a nano-scale optical probe the dimensions of which are far smaller than the optical diffraction limit. The idea for AMOL was first published in Ref. 1 and the most significant results were demonstrated in Ref. 2. As shown in Fig. 2.2 [2] features down to ~ 30 nm could be patterned by AMOL, which is a tenth of the λ_1 (exposing wavelength).

2.2 Photochromic Molecules Used in AMOL

The first observation of photochromic behavior in organic molecules was first observed in the late 19th century [3]. Photochromism is defined as the reversible transition between isomeric states of a molecule brought about by the illumination and subsequent absorption of selective photons of specific wavelengths. The photochromic molecules that are used for the experiments described in this dissertation belong to a family of photochromes called diarylethenes. Some of the salient features of this family are thermal irreversibility, resilience of photofatigue, thereby enabling multitude of phototransitions to occur without noticeable degradation in molecular structures and high photoreactivity, which allows one to work with low light intensities. Two specific types of diarylethenes have been explored in this dissertation as shown in Fig. 2.3. These are the 1,2-bis(5,5-dimethyl-2,2-bithiophen-yl) perfluorocyclopent-1-ene, known colloquially as BTE, and the 1,2-bis(2-methyl-5-(p-cyanophenyl)-3-thienyl)-3,3,4,4,5,5-hexafluoro-1-cyclopentene, otherwise referred to as cPTE. For both these molecules, one of the isomeric states exhibit a central benzene ring that is "open." The other isomeric state is closed-ring in comparison. Hence, for simplicity these two states are referred to as the open (O) and the closed (C) states as alluded to in the previous section. These molecules are synthesized by our colleagues at the University of Massachusetts Amherst, under the guidance of Prof. Trisha L. Andrew. The description of the methods for synthesizing these molecules can be found in Ref. 4 as well as the supplementary information to Ref. 2. Since the scope of this dissertation is restricted to the application of the molecules to perform super-resolution lithography, the discussion of their synthesis is not undertaken here.

2.3 Literature survey on AMOL

The idea of AMOL was first published in Ref. 1. The work in this paper lay the groundwork for further theoretical and experimental study on the technique. Following this, a number of publications proved the validity of the method experimentally [5-7] of which one of the more significant ones was the demonstration of spatial-frequency multiplication which is otherwise not possible for linear lithographic exposure systems [7]. The most significant results were published in Ref. 2, which also introduced the concept of scaling. Since the subwavelength aperture that is created in the AML is a result of the dual wavelength exposure system and the photochemistry of the molecules, this paper described the idea that similar to STED, the size of this aperture could be controlled by the ratio of the intensities of the two beams. This is unlike a traditional lithographic exposure, where the size of the patterned feature is directly controlled by the absolute intensity of the exposing beam. A diagrammatic explanation is provided in Fig. 2.4(a) with simplistic preliminary results of simulations predicting the scaling trend in Fig. 2.4(b). Masid et al. [8] showed that the AML could be reused thereby reducing the consumption of the photochromic molecules per exposure. The AMOL process was characterized through simulations using simple scalar theory [9] as well as vector analyses [10, 11] that provided insights to the governing dynamics of the technique. The effect of plasmonic reflective under-layers to improve the process latitude of AMOL has also been investigated [12,13].

2.4 Advantages of AMOL

AMOL is a culmination of a number of fields of study such as chemistry, which governs the synthesis and characterization of the photochromic molecules for the

AML, optics which governs the light-matter interaction and the optical setups responsible for carrying out lithographic exposures, material science, and metrology that are responsible for governing the interaction between the different chemical layers that make up an AMOL exposure stack, and computer programming which is used to model and simulate the AMOL process for in-depth study.

There are a number of advantages to AMOL. It is an optical lithography system with the ability to consistently pattern sub-100 nm features. Being an optical system, it avoids the disadvantages that come with electron-beam-based patterning techniques, like the effect of stray charges, charge accumulation and sensitivity to interparticle fields. Additionally, the AML being a separate layer, AMOL can be readily combined with industry standard photoresists that come from a thoroughly mature field of study with a broad body of research literature and academic understanding. AMOL also uses much lower intensity light as compared to competing superresolution techniques, a lot of which rely on multiphoton absorption [14, 15]. AMOL can be parallelized to offer improved throughput and fast patterning. Finally, it is a maskless technique, thereby allowing for flexibility with the design process steps. In the next section, the primary challenges and issues related to AMOL that this dissertation aims to address and explore, will be discussed.

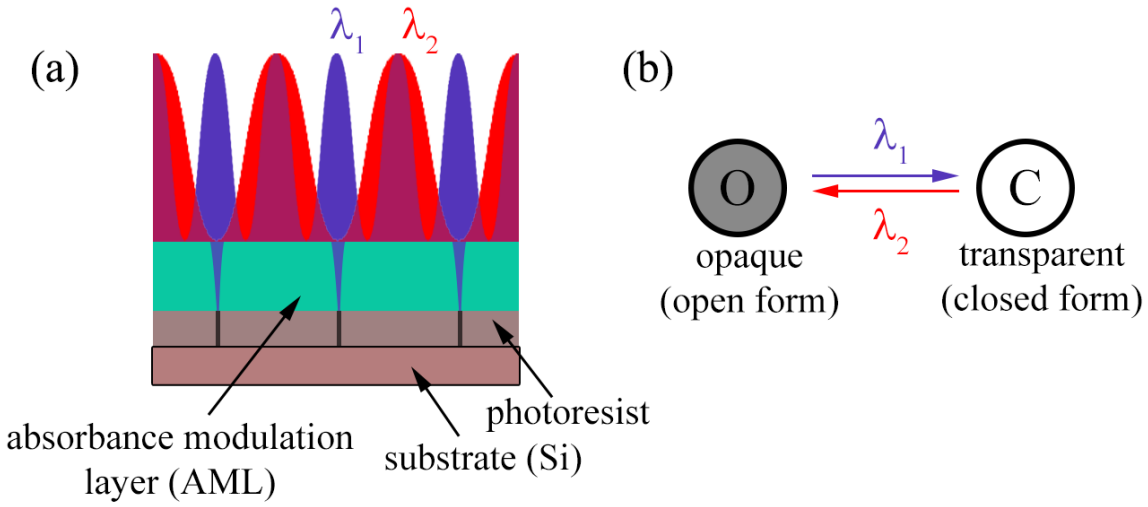

Figure 2.1: AMOL exposure. (a) Schematic of AMOL exposure (b) The two isomeric forms of the photochromic molecules used in AMOL interconvert among themselves based on the illumination wavelength.

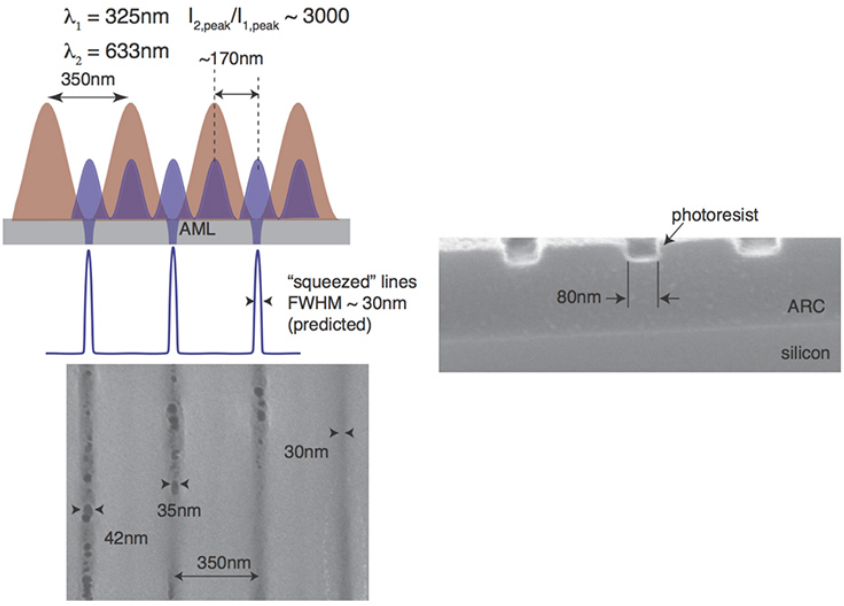

Figure 2.2: Confinement of light to deep subwavelength dimensions using the AMOL process. Lithographic patterning of features with linewidths as small as ~ 30 nm, separated by a period equal to that of the λ_2 standing wave, while having been exposed by λ_1 had been demonstrated in [2].

(a)

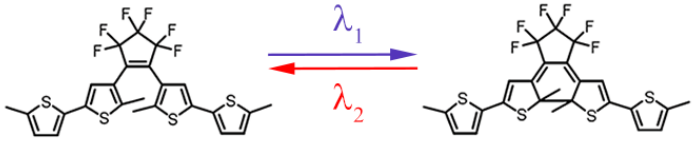

opaque
(open form)

transparent
(closed form)

1,2-bis(5,5-dimethyl-2,2-bithiophen-yl) perfluorocyclopent-1-ene
(BTE)

(b)

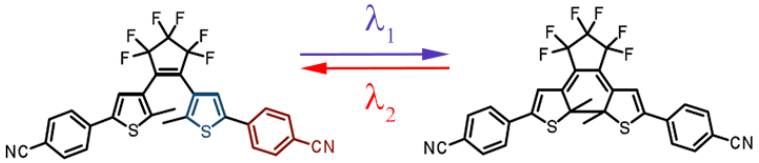

opaque
(open form)

transparent
(closed form)

1,2-bis(2-methyl-5-(p-cyanophenyl)-3-thienyl)-3,3,4,4,5,5-hexafluoro-1-cyclopentene
(cPTE)

Figure 2.3: Diarylethene molecules (a) 1,2-bis(5,5-dimethyl-2,2-bithiophen-yl) perfluorocyclopent-1-ene (BTE) and (b) 1,2-bis(2-methyl-5-(p-cyanophenyl)-3-thienyl)-3,3,4,4,5,5-hexafluoro-1-cyclopentene (cPTE).

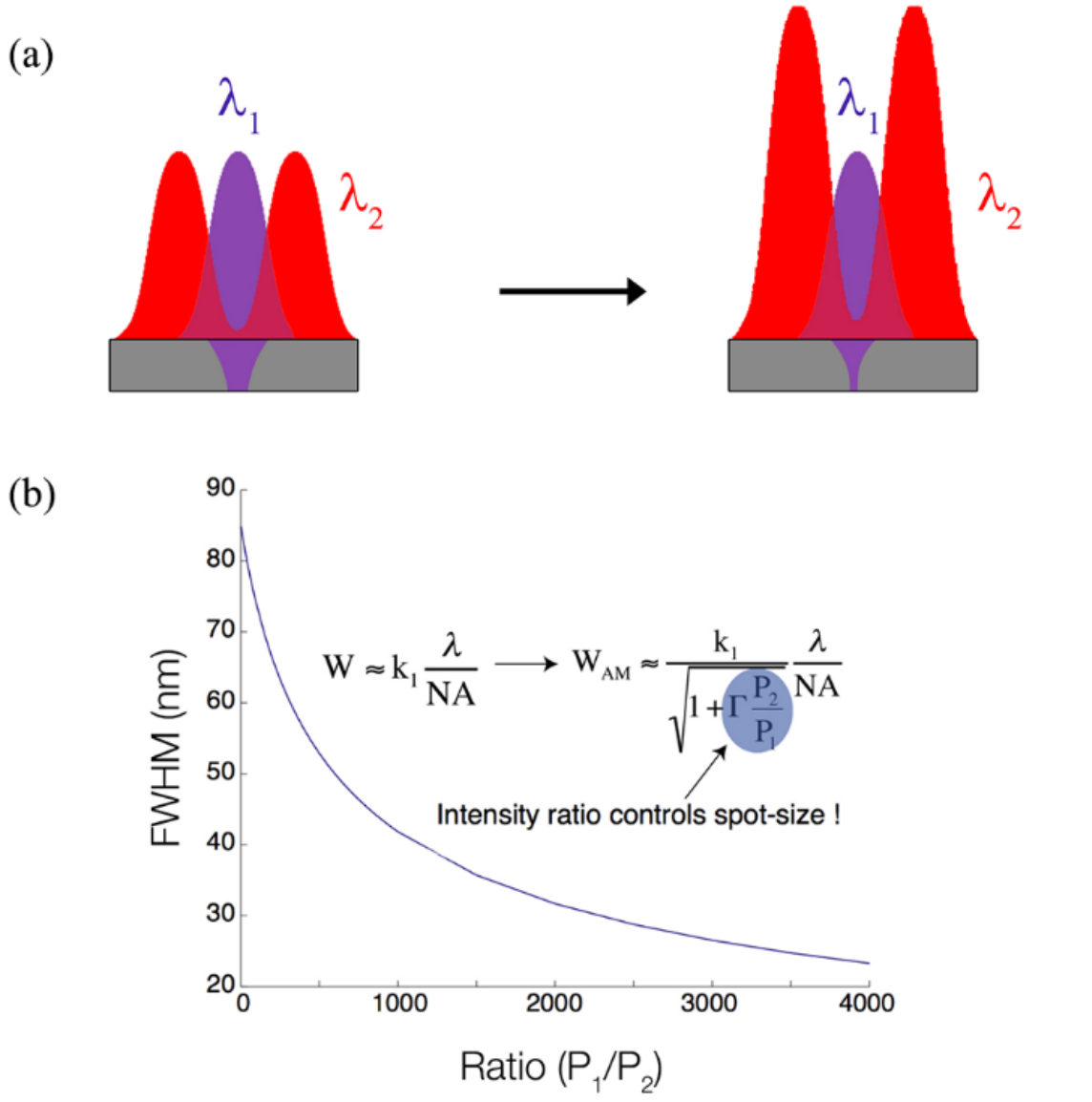

Figure 2.4: Feature scaling in AMOL: In AMOL, the size of the exposure spot is controlled by the ratio of the intensities of the two wavelengths instead of the absolute intensity of the exposing beam. This is shown as a schematic in (a) and preliminary simulation results showing the decrease in the full-width-half-maximum (FWHM) of the linewidth as a function of the ratio of the intensites [2] is shown in (b).

2.5 References

1. R. Menon and H. I. Smith, "Absorbance-modulation optical lithography," *J. Opt. Soc. Am. A*, vol. 23, no. 9, Sep. 2006, pp. 2290-2294.

2. T. L. Andrew, H-Y. Tsai, and R. Menon, "Confining light to deep sub-wavelength dimensions to enable optical nanopatterning," *Science*, vol. 324, no. 5929, May, 2009, pp. 917-921.

3. T. L. Andrew, "Design and synthesis of organic chromophores for imaging, lithography and organic electronics," Doctoral Dissertation, Massachusetts Institute of Technology, Feb. 2011, pp. 110-115.

4. R. Menon, H-Y Tsai, and H. I. Smith, "Patterning and imaging at the nanoscale with far-field optics via absorbance modulation," *Photonic Metamaterials: From Random to Periodic, OSA Technical Digest*, Optical Society of America, Jackson Hole, Wyoming United States, June 2007, pp. WA3. DOI:10.1364/META.2007.WA3.

5. R. Menon, H-Y Tsai, and S. W. Thomas III, "Far-field generation of localized light fields using absorbance modulation," *Phys. Rev. Lett.*, vol. 98, no. 043905, Jan. 2007, pp. 043905-1-4. DOI:10.1103/PhysRevLett.98.043905.

6. H-Y. Tsai, G. M. Wallraff, and R. Menon, "Spatial-frequency multiplication via absorbance modulation," *Appl. Phys. Lett.*, vol. 91, no. 9, Aug. 2007, pp. 094103-1-4. DOI:10.1063/1.2775092.

7. F. Masid, T. L. Andrew, and R. Menon, "Optical patterning of features with spacing below the far-field diffraction limit using absorbance modulation," *Opt. Exp.*, vol. 21, no. 4, Feb. 2013, pp. 5209-5214.

8. G. Pariani, R. Castagna, R. Menon, C. Bertarelli, and A. Bianco, "Modeling absorbance-modulation optical lithography in photochromic films," *Opt. Lett.*, vol. 38, no. 16, Aug. 2013, pp. 3024-3027.

9. J. E. Foulkes and R. J. Blaikie, "Influence of polarization on absorbance modulated subwavelength grating structures," *J. Vac. Sci. Tech. B*, vol. 27, 2009, pp. 2941-2946.

10. J. E. Foulkes, "Absorbance modulation optical lithography: Simulating the performance of an adaptable absorbance mask in the near-field," Doctoral Dissertation, University of Canterbury, 2010.

11. J. E. Foulkes and R. J. Blaikie, "Performance enhancements to absorbance-modulation optical lithography. I. Plasmonic reflector layers," *J. Opt. Soc. Am. A*, vol. 28, no.11, Nov. 2011, pp. 2209-2217.

12. J. E. Foulkes and R. J. Blaikie, "Performance enhancements to absorbance-modulation optical lithography. II. Plasmonic reflector superlenses," *J. Opt. Soc.*

Am. A, vol. 28, no.11, Nov. 2011, pp. 2218-2225.

13. C. W. Holzwarth, J. E. Foulkes, and R. J. Blaikie, "Increased process latitude in absorbance-modulated lithography via a plasmonic reflector," *Opt. Exp.*, vol. 19, no. 18, Aug. 2011, pp. 17790-17798.

14. L. Li, R. R. Gattass, E. Gershgoren, H. Hwang, and J. T. Fourkas, "Achieving λ/20 resolution by one-color initiation and deactivation of polymerization," *Science*, vol. 324, no. 5929, May, 2009, pp. 910-913.

15. T. F. Scott, B. A. Kowalski, R. R. McLeod *et al.*, "Two-color single-photon photoinitiation and photoinhibition for subdiffraction photolithography," *Science*, vol. 324, no. 5929, May, 2009, pp. 913-917.

CHAPTER 3

BARRIER FREE ABSORBANCE MODULATION FOR SUPER-RESOLUTION OPTICAL LITHOGRAPHY

Reprinted with permission from: A. Majumder, F. Masid, B. J. Pollock, T. L. Andrew, and R. Menon, "Barrier free absorbance modulation for super-resolution optical lithography," *Opt. Exp.*, vol. 23, no.9, Apr. 2015, pp. 12244-12250.

Barrier-free absorbance modulation for super-resolution optical lithography

Apratim Majumder,[1] Farhana Masid,[1] Benjamin Pollock,[2] Trisha L. Andrew,[2] and Rajesh Menon[1,*]

[1]*Department of Electrical and Computer Engineering, University of Utah, Salt Lake City, UT 84102, USA*
[2]*Department of Chemistry, University of Wisconsin-Madison, Madison, WI 53706, USA*
[*]*rmenon@eng.utah.edu*

Abstract: Absorbance-Modulation-Optical Lithography (AMOL) enables super-resolution optical lithography by simultaneous illumination of a photochromic film by a bright spot at one wavelength, λ_1 and a node at another wavelength, λ_2. A deep subwavelength region of the transparent photochromic isomer is created in the vicinity of the node. Light at λ_1 penetrates this region and exposes an underlying photoresist layer. In conventional AMOL, a barrier layer is required to protect the photoresist from the photochromic layer. Here, we demonstrate barrier-free AMOL, which considerably simplifies the process. Specifically, we pattern lines as small as 70nm using λ_1 = 325nm and λ_2 = 647nm. We further elucidate the minimum requirements for AMOL to enable multiple exposures so as to break the diffraction limit.

OCIS codes: (220.0220) Optical design and fabrication; (050.6624) Subwavelength structures; (220.3740) Lithography; (110.4235) Nanolithography; (110.5220) Photolithography.

References and links

1. F. M. Scellenberg, "Selected papers on resolution enhancement techniques in optical lithography," SPIE Milestone Services **178**, (2004).
2. E. Abbé, "Beitragezurtheorie des mikroskops und der mikroskopischenwahrnehmung," Arch. Mikrosk. Anat. Entwichlungsmech **9**(1), 413–418 (1873).
3. E. A. Ash and G. Nicholls, "Super-resolution aperture scanning microscope," Nature **237**(5357), 510–512 (1972).
4. E. Betzig, J. K. Trautman, T. D. Harris, J. S. Weiner, and R. L. Kostelak, "Breaking the diffraction barrier: optical microscopy on a nanometric scale," Science **251**(5000), 1468–1470 (1991).
5. L. Novotny, B. Hecht, and D. Pohl, "Implications of high resolution to near-field optical microscopy," Ultramicroscopy **71**(1–4), 341–344 (1998).
6. S. W. Hell and J. Wichmann, "Breaking the diffraction resolution limit by stimulated emission: stimulated-emission-depletion fluorescence microscopy," Opt. Lett. **19**(11), 780–782 (1994).
7. J. T. Fourkas, "Nanoscale photolithography with visible light," J. Phys. Chem. Lett. **1**(8), 1221–1227 (2010).
8. L. Li, R. R. Gattass, E. Gershgoren, H. Hwang, and J. T. Fourkas, "Achieving lambda/20 resolution by one-color initiation and deactivation of polymerization," Science **324**(5929), 910–913 (2009).
9. T. F. Scott, B. A. Kowalski, A. C. Sullivan, C. N. Bowman, and R. R. McLeod, "Two-color single-Photon photoinitiation and photoinhibition for subdiffraction photolithography," Science **324**(5929), 913–917 (2009).
10. T. Tsuujioka, M. Kume, Y. Horikawa, A. Ishikawa, and M. Irie, "Super-resolution disk with a photochromic mask layer," Jpn. J. Appl. Phys. **36**(Part 1, No. 1B), 526–529 (1997).
11. T. Tsujioka, M. Kume, and M. Irie, "Theoretical analysis of super-resolution optical disk mastering using a photoreactive dye mask layer," Opt. Rev. **4**(3), 385–389 (1997).
12. J. Fischer, G. von Freymann, and M. Wegener, "The materials challenge in diffraction-unlimited direct-laser-writing optical lithography," Adv. Mater. **22**(32), 3578–3582 (2010).
13. R. Wollhofen, J. Katzmann, C. Hrelescu, J. Jacak, and T. A. Klar, "120 nm resolution and 55 nm structure size in STED-lithography," Opt. Express **21**(9), 10831–10840 (2013).
14. Z. Gan, Y. Cao, R. A. Evans, and M. Gu, "Three-dimensional deep sub-diffraction optical beam lithography with 9 nm feature size," Nat. Commun. **4**(2061), 2061 (2013).
15. C. Fonseca, M. Somervell, S. Scheer, Y. Kuwahara, K. Nafus, R. Gronheid, S. Tarutani, and Y. Enomoto, "Advances in dual-tone development for pitch frequency doubling," Proc. SPIE **7640**, 76400E (2010).

16. R. Menon and H. I. Smith, "Absorbance-modulation optical lithography," J. Opt. Soc. Am. A **23**(9), 2290–2294 (2006).
17. T. L. Andrew, H.-Y. Tsai, and R. Menon, "Confining light to deep subwavelength dimensions to enable optical Nanopatterning," Science **324**(5929), 917–921 (2009).
18. F. Masid, T. L. Andrew, and R. Menon, "Optical patterning of features with spacing below the far-field diffraction limit using absorbance modulation," Opt. Express **21**(4), 5209–5214 (2013).
19. G. Pariani, R. Castagna, R. Menon, C. Bertarelli, and A. Bianco, "Modeling absorbance-modulation optical lithography in photochromic films," Opt. Lett. **38**(16), 3024–3027 (2013).
20. J. Foulkes and R. Blaikie, "Finite Element Simulation of Absorbance Modulation Optical Lithography," in *Proceedings of International Conference on Nanoscience and Nanotechnology (ICONN 2008)*, 184–187 (2008).
21. R. Menon, D. Gil, and H. I. Smith, "Experimental characterization of focusing by high-numerical-aperture zone plates," J. Opt. Soc. Am. A **23**(3), 567–571 (2006).
22. T. Ito, T. Yamada, Y. Inao, T. Yamaguchi, N. Mizutani, and R. Kuroda, "Fabrication of half-pitch 32 nm resist patterns using near-field lithography with a - Si mask," Appl. Phys. Lett. **89**(3), 033113 (2006).

1. Introduction

The capability of the semiconductor industry to continuously produce nano-scale patterns using conventional top-down photolithography is fast approaching its limits due to diffraction. Scaling the exposure wavelength to extreme ultraviolet (EUV, λ~13nm) is the industry-chosen approach for next-generation lithography. However, it is increasingly clear that this solution is considerably more expensive and does not provide sufficient throughput for many applications [1]. Resolution in photolithography is fundamentally limited by the diffraction limit to about $\lambda/2$, where λ is the illumination wavelength [2]. If one were able to circumvent this limit, inexpensive and mature long-wavelength sources and concomitant processes can be used for advanced lithography. Near-field-optical lithography has been proposed to overcome this limit by localizing the illumination to sub-wavelength regions [3–5]. However, the feature-size control for these techniques is fraught with problems, since the gap between the photomask and the photoresist needs to be controlled to nanometer precision over the field of exposure (several mm^2). An alternative and more promising approach exploits reversible photochemical transitions inspired by successes in stimulated-emission-depletion-microscopy (STED) [6]. In particular, these employ either a combination of 2-photon polymerization and 1-photon de-polymerization [7, 8] or single-photon photo-initiation-photo-inhibition [9] to drastically suppress the vicinity of a region where exposure occurs. Techniques that can separate the photo-switching element from the recording media [10, 11] have also been proposed. For all of these techniques, several materials challenges exist [12]. In addition to the ability to fabricate isolated structures with feature sizes below the diffraction limit, it must be realized that breaking the far-field diffraction limit requires patterning two neighboring features separated by a distance that is less than $\lambda/2$. There are examples of two-photon direct laser writing combined with STED lithography [13] that have been able to achieve a separation of 52nm between two lines [14]. However these processes involve very high intensities for the two-photon polymerization step, specialized resins and polymers, pulsed laser systems that are expensive, and also are relatively slow. In the semiconductor industry, multiple patterning is used to achieve sub-wavelength resolution. However, this involves an etching step after each exposure, which considerably reduces throughput, increases processing steps and requires precise overlay. Another option is to manipulate the chemical formulation of the photoresist to increase its nonlinearity or to enable dual-tone development [15].

Our approach, named Absorbance-Modulation-Optical Lithography (AMOL) [16] was able to pattern features with widths less than 1/10th of the exposure wavelength [17]. AMOL uses a thin photochromic film referred to as the Absorbance-Modulation Layer (AML) that is simultaneously illuminated with a writing beam focused to a spot of wavelength, λ_1 and a confining beam focused to a ring of wavelength, λ_2. λ_1 is typically in the UV region (325 nm) and converts the AML to a transparent form (transparent to λ_1), while λ_2, a visible wavelength reverses the reaction to render the AML opaque (opaque to λ_1). These competing effects restrict the transmission of λ_1 to the vicinity of the nodes of λ_2. A photoresist layer placed

below the AML records the λ_1 photons. Since the region through which λ_1 can penetrate the AML is primarily limited not by diffraction but by the photochemical equilibrium, the diffraction limit can be overcome. Thus the advantages of AMOL are: (a) it involves no intermittent etch step, (b) the non-linearity is introduced within the AML and hence, subsequent exposures can be spaced at separations less than the diffraction limit, (c) no chemical re-formulation of photoresist is required – one of the important points of this article is to show the compatibility of the AMOL process and the AML material formulation with commercially available photoresist in order to prove that AMOL can be easily adapted to current technologies and (d) no high light intensities are required.

In previous implementations of AMOL, a barrier layer (typically poly-vinyl alcohol or PVA) is utilized to protect the photoresist from the solvents used to spin-cast the AML. This barrier layer has to be thick enough to protect the photoresist but thin enough to prevent significant diffraction of the transmitted λ_1 photons. Furthermore, this layer has to be removed after exposure and prior to development of the photoresist. It would be extremely useful to develop a technique, where this barrier layer isn't necessary. Recently, a method was proposed to invert the sample stack to remove this barrier layer [18]. However, this method is only applicable for transparent samples and is not useful for silicon.

In this article, we present three important contributions. Firstly, we demonstrate barrier-free AMOL. Secondly, we validate previous numerical predictions of scaling of the feature size with the ratio of the peak intensities at λ_1 and at λ_2 [19, 20]. Thirdly, we elucidate the process requirements to allow AMOL to break the diffraction limit by enabling multiple exposures of closely spaced features.

2. Experiments

We developed a formulation of the AML that is chemically compatible with two conventional photoresists. The AML was formulated using the photochromic molecule 1,2-bis(5,5′ – dimethyl-2,2'-bithiophen-4-yl) perfluorocyclopent-1-ene (otherwise referred to as BTE) suspended in a polymer-matrix of polystyrene dissolved in Toluene with a 93.63% loading of the BTE in the solution. The photoresists used were the S1813 resist from Shipley and M91Y, a chemically amplified photoresist from JSR Micro. Both resists were extensively tested against toluene over extended periods (several hours) and was shown to have no deleterious impact.

The apparatus used to conduct the lithographic exposures for AMOL is illustrated in Fig. 1. We used a modified Mach-Zehnder interferometer (MZI), shown in Fig. 1(a) to expose our samples. The MZI consisted of the λ_2 (647 nm) laser beam being spatially filtered, collimated and then split by a beam-splitter, guided by mirrors and re-combined at the sample to generate a standing wave. The λ_1 (325 nm) beam was also spatially filtered, collimated and allowed to uniformly illuminate the sample. The AML of the sample was therefore illuminated by a standing wave at λ_2 and a uniform illumination at λ_1. This allowed for the regions of the AML that coincident with the nodes of the λ_2 standing wave to remain transparent, enabling a sub-wavelength exposure of the underlying photoresist. It may be noted that Fig. 1 is a simple illustration to demonstrate the barrier-layer free AMOL process and the diagrammatic representation of the light intensity inside the depth of the photoresist layer and the AML are not strictly accurate. The figure is for illustrative purposes only, as the aim of this article is primarily focused at demonstrating the barrier-free AMOL process and the line-width scaling and accurate AMOL models exist in literature [19, 20].

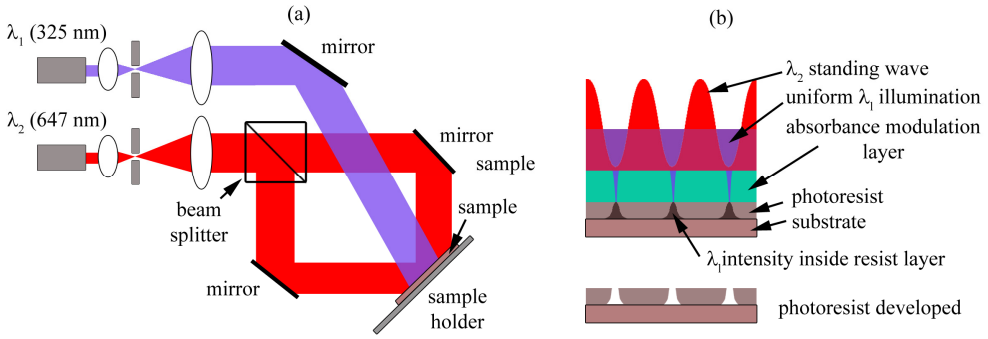

Fig. 1. Experimental set-up to perform AMOL. (a) Schematic of the modified Mach-Zehnder interferometer. Light at λ_2 = 647nm interferes with itself to produce a standing wave while light at λ_1 = 325nm uniformly illuminates the sample. The period of the λ_2 standing wave is 457nm. (b) The sample stack is illuminated by a standing wave at λ_2 and a uniform illumination at λ_1. The competing action of both wavelengths through the absorbance modulation layer exposes the photoresist.

2.1 Linewidth scaling

The silicon wafer substrates were RCA1 and Piranha cleaned and then spin-coated first with a monolayer of hexamethyldisilazane (HMDS) at 6000RPM for 60s with immediate application of the photoresist. Shipley 1813, pre-diluted using Propylene glycol monomethyl ether acetate in the ratio 1:5 by weight, was spun at 4500RPM for 60s with subsequent baking on a hot plate at 115°C for 60s to create a ~500nm-thick layer. Lastly the AML was spin-coated on top of the resist at 730RPM for 60s with subsequent air-drying for 10 minutes, resulting in a thickness of ~650 nm. An illustration of the sample stack is shown in Fig. 1(b). After exposure, the AML was stripped by vigorously rinsing in Toluene for 15s followed by blowing with dry N_2. Dipping in Microposit MF 325 developer for 60 s developed the Shipley 1813 photoresist. Finally, the sample was sputter coated with a thin layer (3-4 nm) of Au/Pd alloy using a Gatan 682 PECS desktop sputter system for inspection in a scanning-electron microscope (FEI Quanta 600 FE-ESEM).

One of the most important features of AMOL is the dependence of the linewidth on the ratio of the peak-intensities of the two wavelengths, instead of the absolute value of the intensity of either [17]. We mapped the line-spread function (LSF) that is recorded in the photoresist (illustrated by circles in Fig. 2(a)) following a previously described technique [21]. Exposures were carried out at four different peak-intensity ratios (I_2/I_1): 2000, 1000, 500 and 100. For each of these ratios, the linewidth is plotted with respect to the inverse of the normalized dose, as shown in Fig. 2(a). We can clearly see that the LSF gets constricted as the ratio is increased. Scanning electron micrographs of the fabricated lines are also shown in Fig. 2(b). The smallest lines resolved are around 90 nm, which is equivalent to $\lambda_1/3.6$ and $\lambda_2/7.2$, respectively. Note that the spacing between the lines is determined by the period of the λ_2 standing wave.

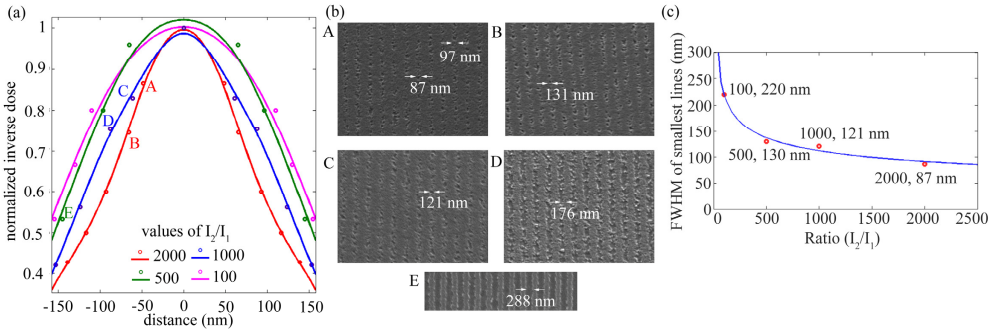

Fig. 2. (a) Mapping of the line-spread function (LSF) for different values of the intensity ratio I_2/I_1. The circles represent the actual exposure results while the solid lines are fits to sinusoids using smoothing spline method. (b) Scanning electron micrographs of the fabricated lines whose measurements were used as the data for the plot shown in part (a). (c) Plot of the FWHM (Full-Width at Half-Maximum) of the smallest lines obtained for each ratio versus the intensity ratio shows the line-width scaling property of AMOL as a function of the intensity ratio of the two wavelengths.

2.2 Conditions for breaking the diffraction limit

In order for AMOL to overcome the diffraction limit, we need to pattern two neighboring features, whose spacing is less than λ/2. This can be achieved by enabling the AML to recover to its original opaque form everywhere after the first feature has been exposed. Subsequently, the sample is displaced and the second feature is patterned. This process has been described previously [17]. However, for this process to work properly, we need to ensure that the AML recovers adequately to its original opaque state. It also requires that the background exposure from λ_1 during each exposure step is minimized. We can refer to this as the contrast of the AML during exposure. This contrast is nonlinearly dependent upon the ratio of peak intensities (I_2/I_1). The question we wanted to answer was, what the minimum ratio, I_2/I_1 is, that is required to enable sufficient contrast in order to overcome the diffraction limit. To answer this question, we performed of UV-Vis absorbance spectroscopy on transparent (fused silica) samples coated with the AML that were exposed to varying ratios I_2/I_1. The results are plotted in Fig. 3.

The samples were first treated with a monolayer of hexamethyldisilazane (HMDS) followed by application of the AML, spin-coated at 730RPM for 60s with subsequent air-drying, for a 650 nm layer. One sample was exposed to uniform λ_1 and λ_2 simultaneously at an I_2/I_1 ratio of ~1000, and its UV-Vis absorbance spectra was monitored after 30min, 60min and 90min of exposure time. Any change in the absorbance spectrum indicates that the photo-stationary state has not been reached, which implies that the ratio (and the contrast) is not high enough. As seen in Fig. 3(a), the absorbance at 325nm reduces with increased exposure time. This means that the opacity of the AML to λ_1 at this ratio (1000) decreases and hence, would contribute to a UV background illumination for the photoresist. This experiment was repeated with $I_2/I_1 = 4000$, and absorbance spectra were taken after 60min and 240min of exposure. As seen in Fig. 3(b), there is no change in the absorbance at 325nm. The absorbance for the 2 samples is plotted as a function of time in Fig. 3(c). It is clear that with $I_2/I_1 = 4000$, one can avoid any background exposure of the photoresist.

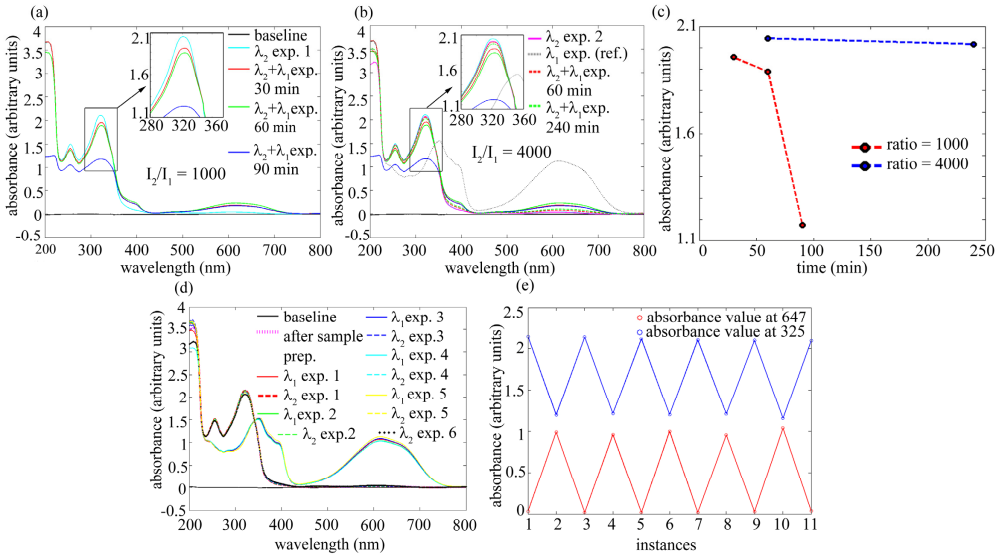

Fig. 3. UV-Vis measurements of the AML layer after simultaneous exposure to the two wavelengths at (a) 1000 intensity ratio, shows the decrease in the opacity of the AML to λ_1, but (b) at 4000 intensity ratio – shows that the opacity of the AML to the λ_1 wavelength is retained. (c) Comparison of the absorbance of the AML at 325 nm for different ratios of simultaneous exposures to λ_1 and λ_2. (d) UV-Vis measurements to show the photo-switch-ability of the AML layer. (e) Absorbance values at the λ_1 and λ_2 wavelengths show that the opacity of the AML layer to λ_1 can be recovered repeatedly.

Another important metric for the AML is its ability to switch between the opaque and transparent states multiple times without any degradation in its absorbance. We monitored the absorbance spectra, while exposing the transparent sample to uniform λ_1 (325nm) illumination at 200μW for 30min (dose approximately equal to the lithographic single exposure dose) and then to uniform λ_2 (647nm) illumination at 200mW for 90min (dose approximately equal to the AML recovery step dose). This is done about 6 times, mimicking 6 exposures. The results plotted in Figs. 3(d) and 3(e) indicate that the AML is indeed able to photo-switch in a repeatable and stable manner.

2.3 Barrier-free AMOL

In order to demonstrate the efficacy of barrier-free AMOL, we built a somewhat simpler Lloyd's-mirror-based interferometer system as illustrated in Fig. 4(a). Lines patterned in S1813 at an intensity ratio (I_2/I_1) = 4000 with an average line-width of ~84 nm are shown in Fig. 4(b). In order to overcome the low sensitivity of the S1813 photoresist, we also developed a process utilizing M91Y, a chemically-amplified resist (CAR) from JSR Micro. This photoresist was sensitized to 325 nm by adding CGI 725 sensitizer (BASF) in the ratio 51:1 by weight. We further verified that this resist is also compatible with toluene, the solvent used for spin-casting the AML. The sensitized M91Y was spun at 6000 RPM for 60s with subsequent baking at 130°C for 90s to create a 450 nm-thick layer. After exposure, the AML layer was first removed by dipping the sample in Toluene for 15 s, then the sample was baked on a hot plate at 130°C for 90 s before being developed in Microposit MF CD-26 developer (0.26N tetramethylammonium hydroxide) for 60s. The sensitized M91Y photoresist has much higher sensitivity than S1813 and also demonstrates significantly lower line-edge roughness as seen by the scanning-electron micrographs in Figs. 4(c). Here, we show lines as thin as 70nm at an intensity ratio of 4000, which is equivalent to $\lambda_1/4.6$ and $\lambda_2/9.2$, respectively. Note that in all cases, no barrier is utilized between the AML and the photoresist.

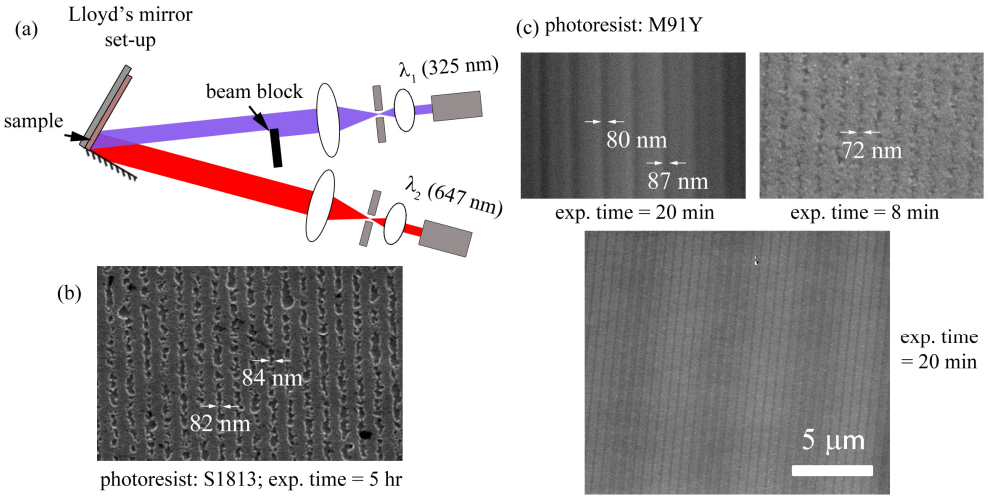

Fig. 4. (a) Modified Lloyd's mirror interferometer for proof-of-principle AMOL exposures. (b) Lines of width ~80 nm fabricated in S1813 photoresist at an intensity ratio of 4000. (c) Lines of width ~70-80nm created in sensitized M91Y photoresist at an intensity ratio of 4000.

It may be noted that the photoresist layer thickness (450-500 nm) is large compared to the achieved linewidths (~70 nm) and this depth will allow for the light at λ_1 to diffract into the depth of the resist layer, with considerable lateral spread. Hence it is evident that in order to fully realize the potential of AMOL and faithfully record the high spatial frequencies in the near-field, ultra-thin photoresist layers are required which agrees well with established literature [22].

3. Conclusion

Here, we demonstrated an approach for optical-super-resolution nanolithography that utilizes an absorbance-modulation layer that is placed directly atop the photoresist layer. By removing the barrier layer that is typically used, we have simplified the lithographic process. Secondly, we utilized this process to demonstrate that the width of an exposed line scales as the ratio of the peak intensities at the nodal and the writing wavelengths. Finally, we performed careful UV-Vis absorbance spectroscopy studies to elucidate the minimum contrast requirements of the AML so as to overcome the diffraction limit via multiple exposures. Combining these advancements with further process optimization will allow for a maskless optical nanopatterning technique that is not only scalable (fast) but also can achieve deep subwavelength resolutions.

Acknowledgment

We would like to thank Brian Van Devener and Paulo Perez for assistance and characterization of the nanostructures, Chaitanya Ullal, for discussion on the experiments and Precious Cantu for helpful insight to the AML. Funding from the NSF Grants #1054899 and #1400142, DARPA award #N660011014065, and the Utah Science Technology and Research (USTAR) initiative are gratefully acknowledged.

CHAPTER 4

MODELING ABSORBANCE MODULATION OPTICAL LITHOGRAPHY

4.1 Motivation

The ability of AMOL to confine light to subdiffraction spots is enabled by a specific nonlinearity that is present in the AMOL system. This is brought about as a combined action of the dual wavelength exposure system and the spectrally selective reversible photochromism of the absorbance modulation layer. In order to fully understand and analyze the technique for further improvement, a comprehensive model is required with robust ability to simulate the AMOL procedure. There have been a few theoretical studies in the past [1-7] with this very specific aim. In this chapter, a brief review of these studies and background information is presented which facilitate the construction of a fully comprehensive AMOL model.

4.2 Background Information

4.2.1 The Menon Model

The use of scalar diffraction theory as an approximation to understanding light-matter interactions has been prevalent in optics literature. The first modelling of the AMOL system by Menon [1] was performed in a similar manner. In that model, the photochromic system was assumed to be in two states, A and B, with specific absorbance values to the two illuminating wavelengths λ_1 and λ_2. The absorbance of

each species is a direct result of the product of the decadic molar absorption coefficient (ε_{ij}) and its concentration ([A] or [B]). The absorption to one of the wavelengths of illumination is thus given by a sum of the absorbance of both the species to that wavelength. This is expressed mathematically as:

$$\alpha_1 = (\alpha_{1A} + \alpha_{1B})l = (\varepsilon_{1A}[A] + \varepsilon_{1B}[B])l \quad (4.1)$$

and

$$\alpha_2 = (\alpha_{2A} + \alpha_{2B})l = (\varepsilon_{2A}[A] + \varepsilon_{2B}[B])l \quad (4.2)$$

where ε_{1A} and ε_{1B} are the decadic molar absorption coefficients of the states A and B to the wavelength λ_1 and [A] and [B] are the concentrations of the two states. l is the thickness of the absorbance modulation layer. Thus, equation 4.1 represents the absorbance of light with wavelength λ_1 and equation 4.2 represents the absorbance of light with wavelength λ_2. The situation is shown in Fig. 4.1 [1, 4].

This set of solutions could be used to numerically solve for the light intensity for the situation shown in Fig. 4.1 to describe the ability of the AMOL system to confine a point spread function (PSF) to subdiffraction dimensions. This approach is simple and gives an overview of the AMOL technique but it does not take into account the effects of diffraction, light polarization, and so forth. A typical solution of Menon's model is shown in Fig. 4.2 [1].

4.2.2 The Pariani Model

Pariani et al. [3] developed another model to simulate the AMOL process. In this approach, the concentration of the transparent state was described using an equation that incorporated the intensity of the exposing light, the concentration of the state, its

quantum efficiency and absorptivity to that wavelength. Following this, Beer-Lambert's law was used to derive the absorption of light intensity through the photochromic layer and calculate the local light intensity at the bottom of the layer. This describes the point spread function. This model was used to simulate the effect of the intensity ratio, the photochromic film thickness, the absorbance cross section and quantum yields on the confinement of the AMOL PSF. However, the approach of this model is too simple since it does not attempt to solve Maxwell's equations, rather only uses the absolute intensity values. Therefore, effects of polarization and diffraction cannot be understood from such a model. At best, this is a very good approximation of the AMOL system.

4.2.3 The Foulkes Model

John Foulkes [4-7] developed another model to implement finite element method (FEM) to solving the AMOL system. In this case, a model of the AMOL exposure stack was built in COMSOL Multiphysics [8] and the built-in optics module of the software was used to solve the propagation of light through this exposure stack. A MATLAB [9] front-end interfaced with COMSOL and contained the primary function to iteratively run the COMSOL model and converge at a solution. Foulkes was thus able to account for the effects of polarization and diffraction. However, Foulkes did not explore the effect of material properties on the AMOL system but went on to investigate other types of sub-diffraction masks and patterning techniques.

4.3 Modeling Approach

4.3.1 Overview of Modeling Approach

In order to effectively describe a nonlinear optical system like AMOL that is dependent both on the illumination conditions of the exposure system as well as material properties heavily, it is very important to incorporate both these aspects into one model. The work of Foulkes set the best way to approach the problem and the work of Pariani allows one to select the scenarios to investigate. Thus, the model described in this dissertation aims to combine the merits of these previous works. The approach to the modelling is followed from the work of Foulkes while attempts are made to simulate the different conditions described in the work of Pariani to gain insight to the effect of material properties on an AMOL system.

4.3.2 Maxwell's Equations

The propagation of electromagnetic waves in a particular medium is expressed traditionally by Maxwell's equations, the differential forms of which when in interaction with matter (Maxwell's macroscopic equations in matter) [10], can be expressed mathematically as follows:

$$\nabla . \boldsymbol{D} = \rho_{\vartheta} \tag{4.3}$$

$$\nabla . \boldsymbol{B} = 0 \tag{4.4}$$

$$\nabla \times \boldsymbol{E} = -\frac{\partial \boldsymbol{B}}{\partial t} \tag{4.5}$$

$$\nabla \times \boldsymbol{H} = \boldsymbol{J} + \frac{\partial \boldsymbol{D}}{\partial t} \tag{4.6}$$

Here, $\boldsymbol{E}$ is the electric field, $\boldsymbol{B}$ the magnetic field, $\boldsymbol{J}$ the current density, ρ_{ϑ} the volume charge density, $\boldsymbol{D}$ the displacement field, and $\boldsymbol{B}$ the magnetizing field.

These equations describe the propagation of light and interaction with matter in

vector form and thus, may be used to completely describe a lithographic exposure system as well as nonlinear photochromic systems like AMOL. This ability is not present in scalar models like those of Menon and Pariani hence they may be treated as approximations to a full vector model. It is obvious that a vector model incorporating the solutions of Maxwell's equations of light-matter interaction would present a more comprehensive description of the AMOL system.

4.3.3 Model Units

The scalar model developed by Menon [1] expressed absorbance as a product of the molar absorptivities of the species and their concentration. However, as will be seen in the next chapter, the confinement of the PSF in AMOL is a direct result of the mole fraction of the species. Hence, it is important to express absorption as an equivalent term. This approach has been adapted from the work of John Foulkes [5], who in turn adapted it from the work of Warner and Blaikie on two-color nonlinear absorption of light in dyes [11].

Warner and Blaikie express the absorbance of one species (α_1) in terms of the Beer length (d_1) and equivalently, as the product of the number density of chromophores (ρ) and the absorption cross-section of the species (Γ_1) [11] as follows:

$$\alpha_1 = \frac{1}{d_1} = \rho\Gamma_1 \qquad (4.7)$$

On the other hand, the generalized expression of the Beer-Lambert law [12] for absorption of light intensity through an absorbing medium is given by the expression [13]:

$$\ln\frac{I_0}{I} = \Gamma m l \qquad (4.8)$$

where l is the distance and m is the number of molecules per unit volume.

The other form of the Beer-Lambert law, using decadic molar absorptivity that is used in Menon's model (ε), concentration of the fluorophores (C) and depth inside the photochromic layer (l) is as follows:

$$\log\frac{I_0}{I} = \varepsilon C l \qquad (4.9)$$

Comparing the above equations, one may equate the two quantities (a) absorption cross-section which is dependent on the number of molecules per volume and (b) decadic molar absorptivity which is dependent on the concentration of species. Avogradro's number is used to interconvert between number of molecules and moles as follows:

$$\frac{\ln\frac{I_0}{I}}{\log\frac{I_0}{I}} = \frac{\Gamma m l}{\varepsilon C l} \qquad (4.10)$$

or

$$2.303 = \frac{\Gamma m}{\varepsilon C} \qquad (4.11)$$

or

$$\Gamma = 2.303\frac{\varepsilon C}{m} = 3.8243 \times 10^{-24}\varepsilon \qquad (4.12)$$

Hence, the model of Menon and Warner have been related and one may convert between the decadic molar absorptivity and absorption cross-section, as per the above equation. This becomes especially important because the modeling described in this work will follow Warner's approach while using the photokinetics of AMOL as stated by Menon.

4.3.4 Vector Modelling in COMSOL

The choice of simulation tool for modeling the AMOL process is COMSOL since it uses finite element method (FEM). One of the primary advantages of FEM is that it

can handle inhomogeneous medium very effectively [14] and is ideally suited for solving nonlinear systems like AMOL. As will be seen later, AMOL is described by a system of differential equations. FEM is able to destruct a given area into many small components and solve numerically, an assigned set of differential equations by converting them into a set of algebraic equations and minimizing the error. Hence, it is not an analytical solution approach. It is a numerical solution method. The solution is calculated at a single frequency per simulation. On the other hand, the one drawback is that since all the values and information must be stored for the entire space over which the solution is being computed at once, inside a large array, it is very computationally intensive with regards to run time and memory usage. However, one may compensate for run time and memory by using meshes with smaller number of individual units.

4.3.5 Example of COMSOL Model – Mach-Zehnder Interferometer

In this section, a simple example of modeling an electromagnetic system is given. A well-known optical system – the Mach-Zehnder Interferometer (MZI) [16, 17] - is modeled in COMSOL and the behavior of this system is simulated. The MZI is also one of the optical setups, a modified version of which is used to perform the AMOL experiments as described in the previous chapter.

In an MZI, a beam of light is split into two arms using a beam splitter and the then combined using a set of beam guiding mirrors to a sample plane, thereby interfering with themselves. This leads to the formation of an interference pattern. The schematic of such a setup is shown in Fig. 4.3 (a). In order to simulate the working of this setup in COMSOL, a model shown in Fig. 4.3 (b) was constructed that closely represents the situation shown in Fig. 4.3 (a). The incident illumination is assumed a

Gaussian beam with an expression for intensity given by equation to resemble the case for a laser beam used in actual experiments. The beam waist is set equal to only 3.5 μm in order to maintain a scale at which to both visualize the Gaussian envelope as well as the interference pattern produced at the sample plane.

In order to solve this model in COMSOL, the beam splitter cube is assigned material properties of glass with refractive index equal to 1.5 + 0i while the mirrors and the half-reflective surface of the beam splitter are assigned refractive index of silver at the operating wavelength of 647 nm (i.e., -16.5 – 1.06i). The surrounding medium is assigned the refractive index of air (i.e., 1 + 0i). The mesh created by COMSOL to solve this model is shown in Fig. 4.4. This demonstrates the ability of FEM to divide a given space into a large number of small elements over which the electromagnetic problem is numerically solved.

The solution to this problem is shown in Fig. 4.5 (a). The beam incident from the left of the beam splitter in the system is split into two arms that are guided by the reflections from the mirrors and made to interfere with each other at the sample plane. The intensity distribution at the sample plane is shown in Fig. 4.5 (b), which clearly demonstrates the interference pattern created within the Gaussian envelope of the beam.

Thus, it is shown that COMSOL can effectively model and simulate EM phenomena using FEM. In the next chapter, the approach to modeling and simulating the AMOL process [18-22] will be discussed with the subsequent chapters presenting the results of the simulation.

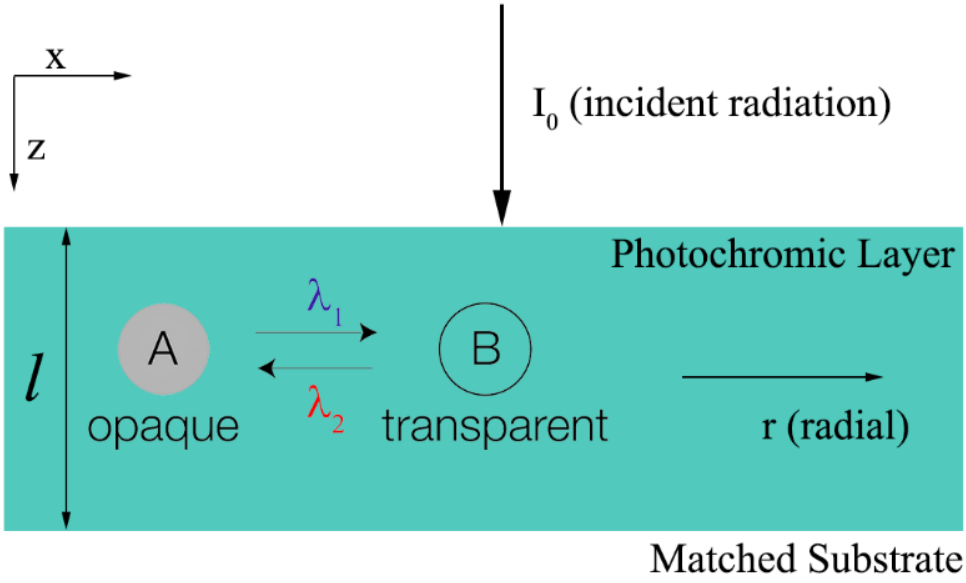

Figure 4.1: Schematic of the system used for solving AMOL by analytical method by Menon [1]. Here, only the incident light intensity I_0 is being considered and its absorption through a depth *l* of the photochromic layer is analyzed.

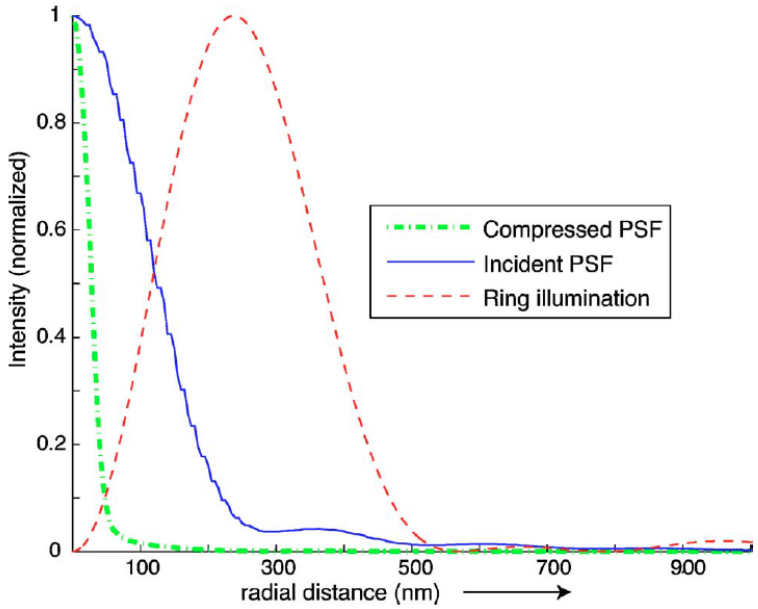

Figure 4.1: Simulation of the confinement of the exposure PSF by AMOL using a ring illumination in the confining beam and a spot illumination in the exposing beam PSF [1].

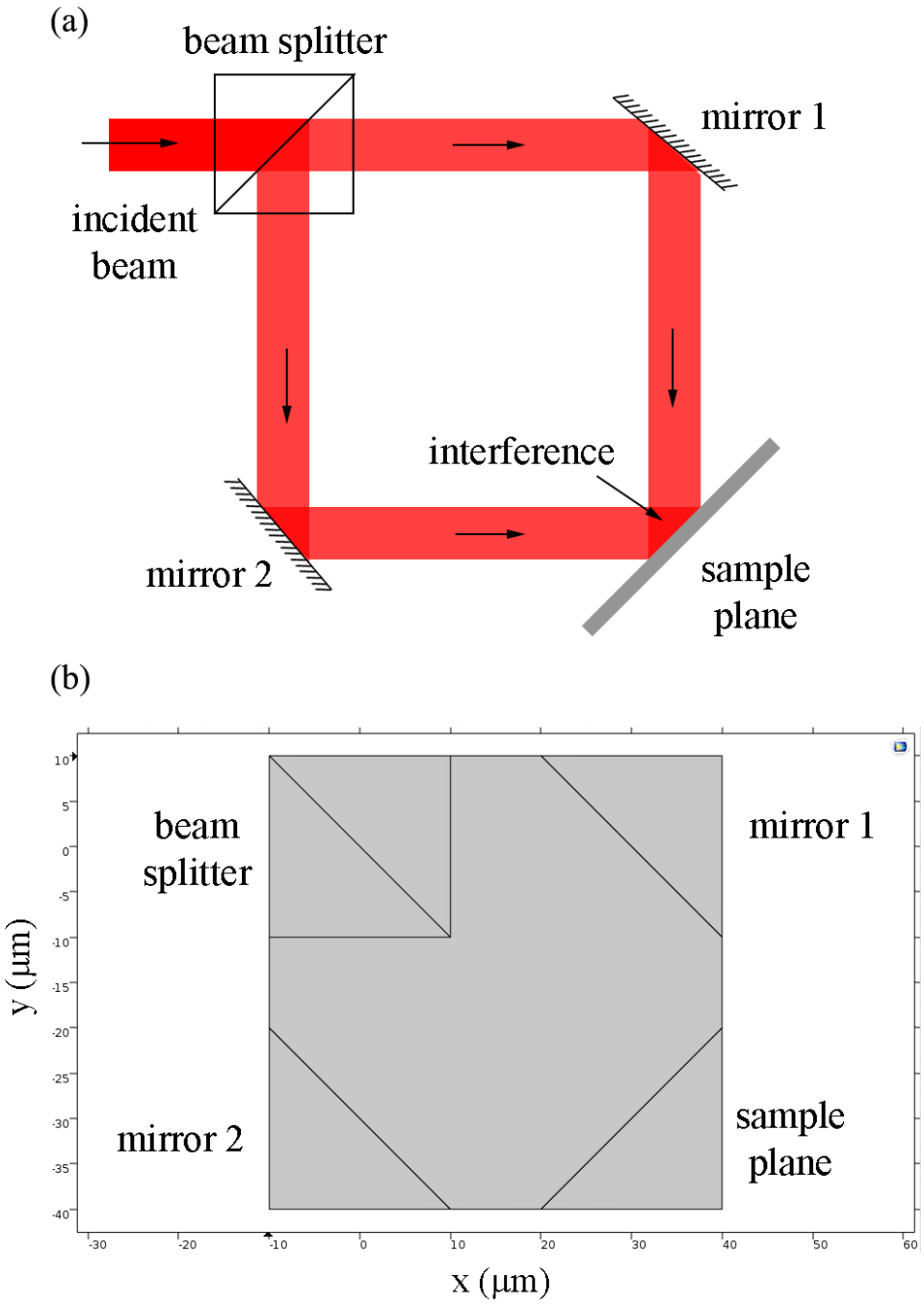

Figure 4.3: Simulation of the Mach-Zehnder interferometer. (a) Schematic of the Mach-Zehnder interferometer. (b) Model constructed in COMSOL with geometry closely resembling the actual interferometer.

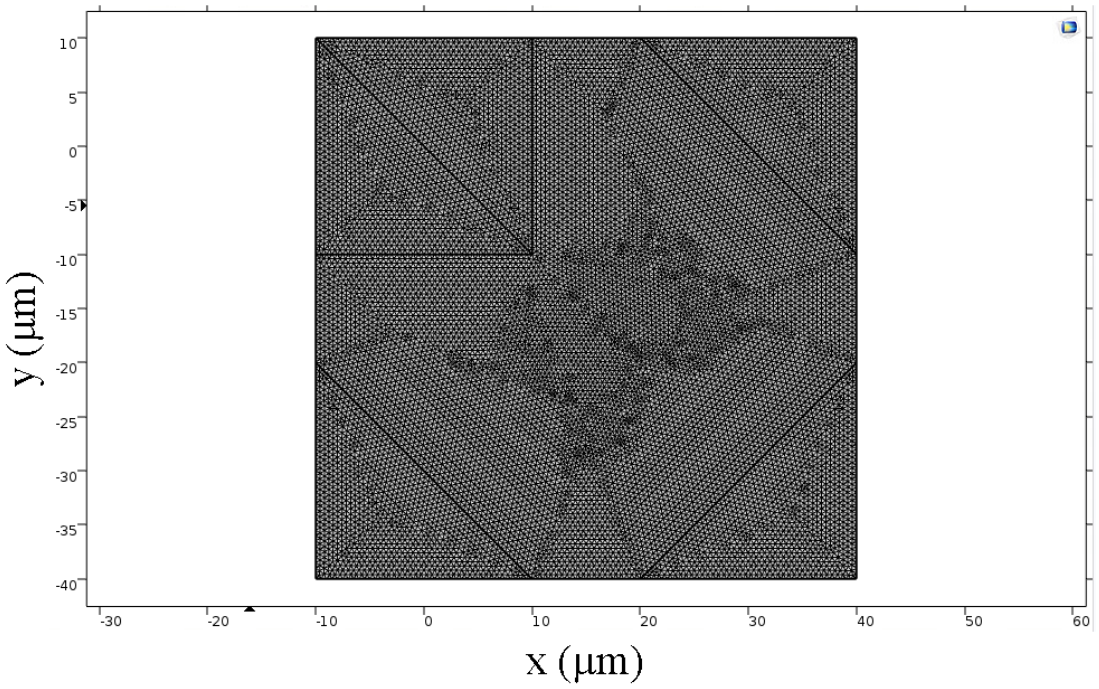

Figure 4.4: Mesh created in COMSOL to solve the Mach-Zehnder Interferometer model.

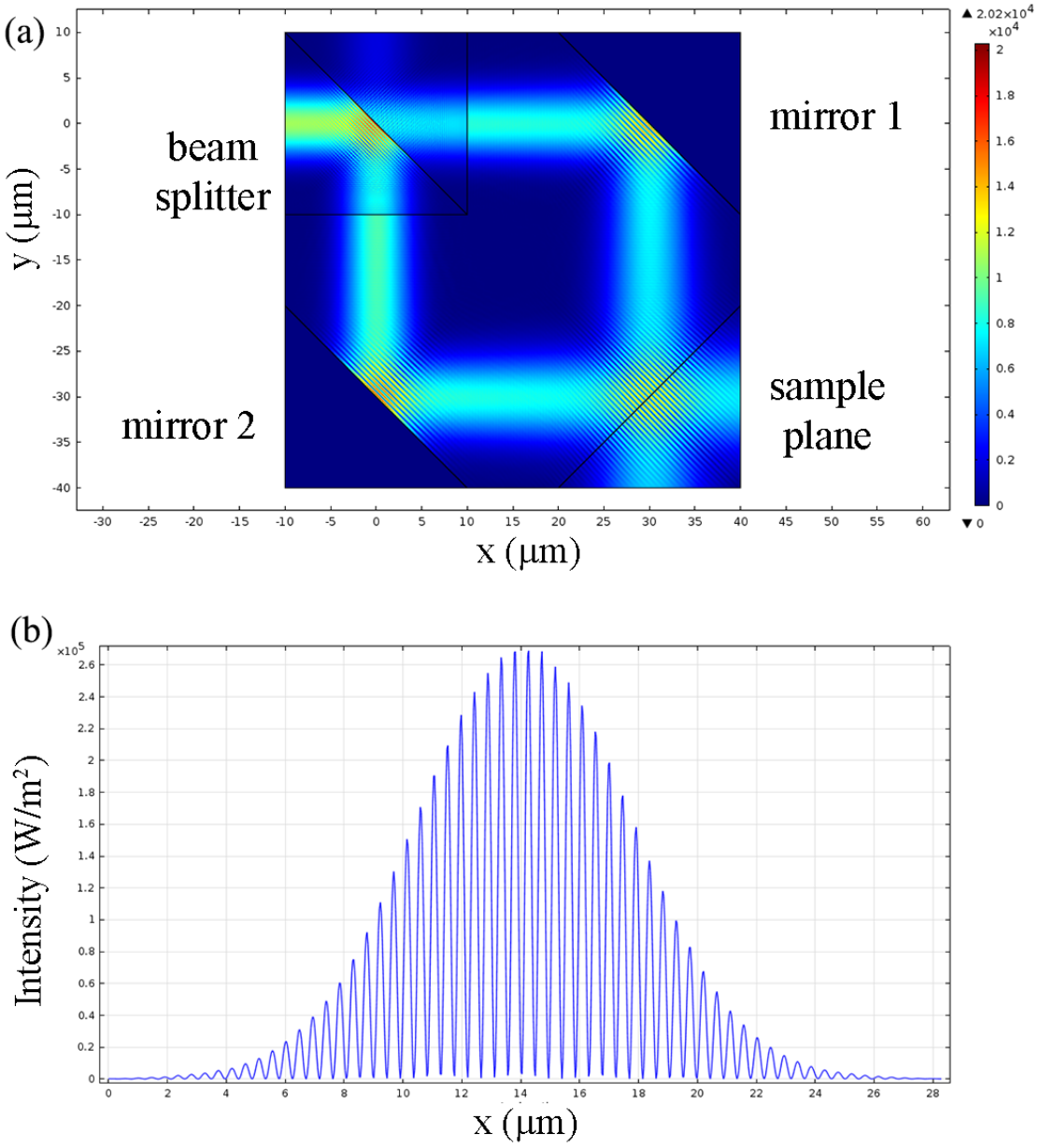

Figure 4.5: Solution of the model for a Mach-Zehnder interferometer in COMSOL. (a) Electromagnetic field distribution in the model showing splitting of the incident beam into two arms by the beam splitter, then being guided by two mirrors to interfere at the sample plane. (b) Intensity distribution at the sample plane showing the interference pattern inside the Gaussian envelope of the incident beam.

4.4 References

1. R. Menon and H. I. Smith, "Absorbance-modulation optical lithography," *J. Opt. Soc. Am. A*, vol. 23, no. 9, Sep. 2006, pp. 2290-2294.

2. R. Menon, H-Y Tsai, and S. W. Thomas III, "Far-field generation of localized light fields using absorbance modulation," *Phys. Rev. Lett.*, vol. 98, no. 043905, Jan. 2007, pp. 043905-1-4. DOI:10.1103/PhysRevLett.98.043905.

3. G. Pariani, R. Castagna, R. Menon, C. Bertarelli, and A. Bianco, "Modeling absorbance-modulation optical lithography in photochromic films," *Opt. Lett.*, vol. 38, no. 16, Aug. 2013, pp. 3024-3027.

4. J. E. Foulkes and R. J. Blaikie, "Influence of polarization on absorbance modulated subwavelength grating structures," *J. Vac. Sci. Tech. B*, vol. 27, 2009, pp. 2941-2946.

5. J. E. Foulkes, "Absorbance modulation optical lithography: Simulating the performance of an adaptable absorbance mask in the near-field," Doctoral Dissertation, University of Canterbury, 2010.

6. J. E. Foulkes and R. J. Blaikie, "Performance enhancements to absorbance-modulation optical lithography. I. Plasmonic reflector layers," *J. Opt. Soc. Am. A*, vol. 28, no.11, Nov. 2011, pp. 2209-2217.

7. J. E. Foulkes and R. J. Blaikie, "Performance enhancements to absorbance-modulation optical lithography. II. Plasmonic reflector superlenses," *J. Opt. Soc. Am. A*, vol. 28, no.11, Nov. 2011, pp. 2218-2225.

8. COMSOL Multiphysics https://www.comsol.com/

9. MATLAB https://www.mathworks.com/products/matlab/

10. M. Born and E. Wolf, *Principles of Optics: Electromagnetic Theory of Propagation, Interference and Diffraction of Light*, 7th ed. London, Cambridge University Press, 2002.

11. M. Warner and R. J. Blaikie, "Two-color nonlinear absorption of light in dye layers," *Phys. Rev. A*, vol. 80, no. 3, Sep. 2009, pp. 033833-1-6.

12. https://en.wikipedia.org/wiki/Beer%E2%80%93Lambert_law\

13. J. R. Lakowicz, *Principles of Fluorescence Spectroscopy*, 2nd ed. New York, Kluwer Academic/Plenum, 1999.

14. C. Mack, *Fundamental Principles of Optical Lithography: The Science of Microfabrication*, 1st ed. Chichester, Hoboken, New Jersey, USA, Wiley, 2007.

15. D. B. Davidson, *Computational Electromagnetics for RF and Microwave*

Engineering, 2nd ed. Cambridge, Cambridge University Press, 2010.

16. L. Zehnder, "Ein neuer Interferenzrefraktor," *Zeitschrift für Instrumentenkunde*, vol. 11, 1891, pp. 275–285.

17. L. Mach, "Ueber einen Interferenzrefraktor," *Zeitschrift für Instrumentenkunde*, vol, 12, 1892, pp. 89–93.

18. T. L. Andrew, "Design and synthesis of organic chromophores for imaging, lithography and organic electronics," Doctoral Dissertation, Massachusetts Institute of Technology, Feb. 2011, pp. 110-115.

19. R. Menon, H-Y Tsai, and H. I. Smith, "Patterning and imaging at the nanoscale with far-field optics via absorbance modulation," *Photonic Metamaterials: From Random to Periodic, OSA Technical Digest*, Optical Society of America, Jackson Hole, Wyoming United States, June 2007, pp. WA3. DOI:10.1364/META.2007.WA3.

20. H-Y. Tsai, G. M. Wallraff, and R. Menon, "Spatial-frequency multiplication via absorbance modulation," *Appl. Phys. Lett.*, vol. 91, no. 9, Aug. 2007, pp. 094103-1-4. DOI:10.1063/1.2775092.

21. F. Masid, T. L. Andrew and R. Menon, "Optical patterning of features with spacing below the far-field diffraction limit using absorbance modulation," *Opt. Exp.*, vol. 21, no. 4, Feb. 2013, pp. 5209-5214.

22. H-Y. Tsai, H. I. Smith, and R. Menon, "Reduction of focal-spot size using dichromats in absorbance modulation," *Opt. Lett.*, vol. 33, no. 24, Dec. 2008, pp. 2916-2918. DOI:10.1364/OL.33.002916.

CHAPTER 5

ABSORBANCE MODULATION MODELING METHOD

5.1 Introduction

In this chapter, the requisite background information for constructing and simulating the performance of AMOL is presented. This information includes the construction of the model in COMSOL, the algorithm used to solve for the EM fields, discussion of the MATLAB front end to change the absorbance parameters of the AML and system equations that are used to solve the overall problem. The work follows the previous work by Menon [1], Foulkes [2], and Warner [3] and shows the effectiveness of the utilization of the FEM to simulating the AMOL process [4].

5.2 Model Construction in COMSOL

The model of the AMOL system is shown in Fig. 5.1. This geometrical structure is set up in COMSOL using the graphic user interface (GUI). It closely resembles an AMOL sample stack. The different layers are as follows (from the bottom up): First, the substrate is modeled as a perfectly matched layer (PML) to mimic the behavior of thin photoresists with antireflection coating (ARC) layers under them or thick photoresist layers, essentially mitigating all forms of reflected light from the substrate. Next, the photoresist layer is present whose refractive index value and thickness can be modified as desired to simulate a wide range of photoresists. Third

is the photochromic layer, again with variable thickness and refractive index values. Lastly, a 500 nm air gap is used to mimic the distance from the laser to the surface of the sample. The light is incident from the top of the sample. Thus, this geometry effectively represents a cross-section of the sample stack used in AMOL experiments [5]. The incident light can be modeled as a plane wave or an interference pattern as per desire. For this work, it is modeled as an interference pattern to represent the peaks and nodes in the AMOL illumination scheme.

The mesh is defined as each element having a size that is $1/5^{th}$ of the shorter wavelength used in the simulation. A representation of the meshing of the model is shown in Fig. 5.1 (c) with enlarged mesh elements to facilitate visualization.

5.3 Boundary Values

The simulation model is assigned periodic boundaries on both sides, left and right. These mimic an infinitely long sample in the x-direction. Indeed, compared to the wavelength of the two illuminations used, the samples used in the experiments that are usually of a few centimeters to millimeters in dimensions can be considered infinitely large. The periodicity changes between periodic and antiperiodic depending on the type of incident illumination. For example, a plane wave would require a periodic condition whereas a sinusoidal intensity distribution, such as an interference pattern, as is the case for AMOL requires antiperiodic conditions.

5.4 Algorithm

The algorithm used to solve the simulations is shown in Fig. 5.2. The initial models for both the wavelengths are first constructed in COMSOL following the geometry discussed in the previous section. All the required material properties are assigned to

the different layers. In order to run the simulation, COMSOL is run as server to MATLAB in order to communicate with the MATLAB front end. First, both the models for the two wavelengths are initialized and the initial run is completed in COMSOL with the desired illumination spatial profile. Next, the light intensity data inside the AML is exported from COMSOL to MATLAB in the form of comma separated values (CSV) files. MATLAB reads this data and saves it as an array. Then the AMOL system equations, which will be described in the next section, are used to calculate the absorbance values within the AML. These absorbance values are also stored in the form of an array. In this case, we divide the AML into 1 nm sized elements, which is considered small enough compared to the wavelengths of the illuminations used. The calculated absorbance values are exported from MATLAB and imported into COMSOL. Then the models are run again. The light intensity values are updated and are exported. This completes one iteration. Since we are solving for AMOL under steady-state conditions, there will be no change in the concentration of the two species of the photochromic material. At every iteration, the change in the concentration is stored. Once this change falls below a certain pre-decided threshold, the simulation is terminated. All results are output and plotted in MATLAB.

5.5 AMOL System Equations

The system equations that govern the AMOL process are discussed here. In general, the behavior of state switching of the photochromic material used in the AML follows first order kinetics. The conversion rate of either species is dependent on four factors: (1) intensity of the illuminating wavelength (I_1 for λ_1 and I_2 for λ_2), (2) instantaneous molar concentration of the species ($[O]$ or $[C]$) , (3) the decadic molar absorptivity at the specific wavelength of illumination (ε_{ij}, e.g., denoted by ε_{1O} for open

form at λ_1) and (4) the quantum yield of the photochemical reactions (φ_{ij}, e.g., denoted by φ_{OC} for conversion from open to closed form) [6]. Thus, for such a photochemical reaction, the rate equation is given as follows:

$$-\frac{\partial[O]}{\partial t} = [O]I_1\varepsilon_{1O}\varphi_{OC} - [C]I_2\varepsilon_{2C}\varphi_{CO} - [C]I_1\varepsilon_{1C}\varphi_{CO} + [O]I_2\varepsilon_{2O}\varphi_{OC} \quad (5.1)$$

However, it is to be noted that λ_2 photons are not sufficiently energetic to induce the open-to-closed transition. Hence, the fourth term in equation 5.1 can be ignored.

In addition, from the conservation of mass, we have:

$$[O] + [C] = [O]_0 \quad (5.2)$$

where $[O]_0$ is the initial concentration of the photochromic molecules inside the AML, under the assumption that the initial state is composed only of the open form which is true for experiments [5].

Thus, at the photostationary state, when $\frac{\partial[O]}{\partial t} = 0$, the equation 5.1 can be reduced to the following form:

$$\frac{[C]}{[O]_0} = x_C = \frac{1}{1 + {}^{I_2}/_{I_1}\,{}^{\varepsilon_{2C}}/_{\varepsilon_{1O}}\,{}^{\varphi_{CO}}/_{\varphi_{OC}} + {}^{\varepsilon_{1C}}/_{\varepsilon_{1O}}\,{}^{\varphi_{CO}}/_{\varphi_{OC}}} \quad (5.3)$$

Here, x_C is the mole fraction of the closed form, whereas $1 - x_C = x_O$ is the mole fraction of the open form.

This system of equations is used in MATLAB to calculate the concentration of the species for every iteration of the simulation. Fig 5.3 shows a representative solution of the aperture formation inside the photohromic layer using this method of simulation. Fig. 5.3 (b) shows the decrease in the change in concentration of the species to a point where it is below a certain threshold. At this point, the conditions of steady state are assumed to have been reached and the simulation is terminated.

The next chapter will present the results of this modeling and simulation and investigate the effect of various parameters in the AMOL process.

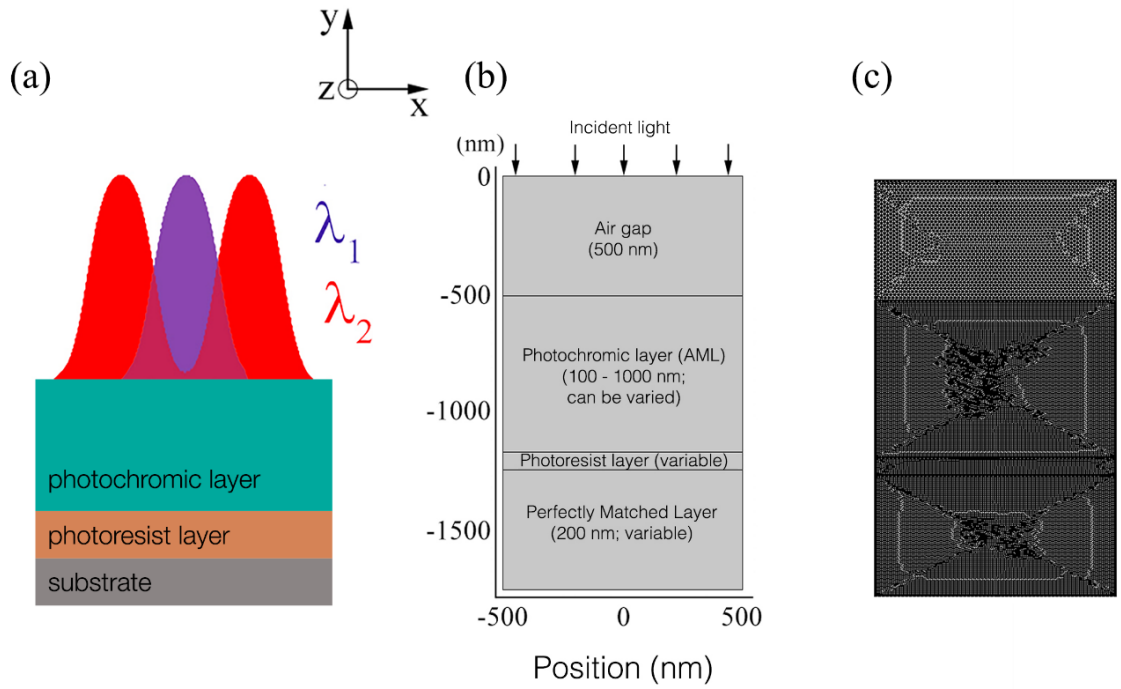

Figure 5.1: AMOL simulation set up. (a) AMOL sample stack used in experiments. (b) Geometry of model constructed in COMSOL to represent the sample stack used in AMOL experiments. (c) Model mesh constructed in COMSOL.

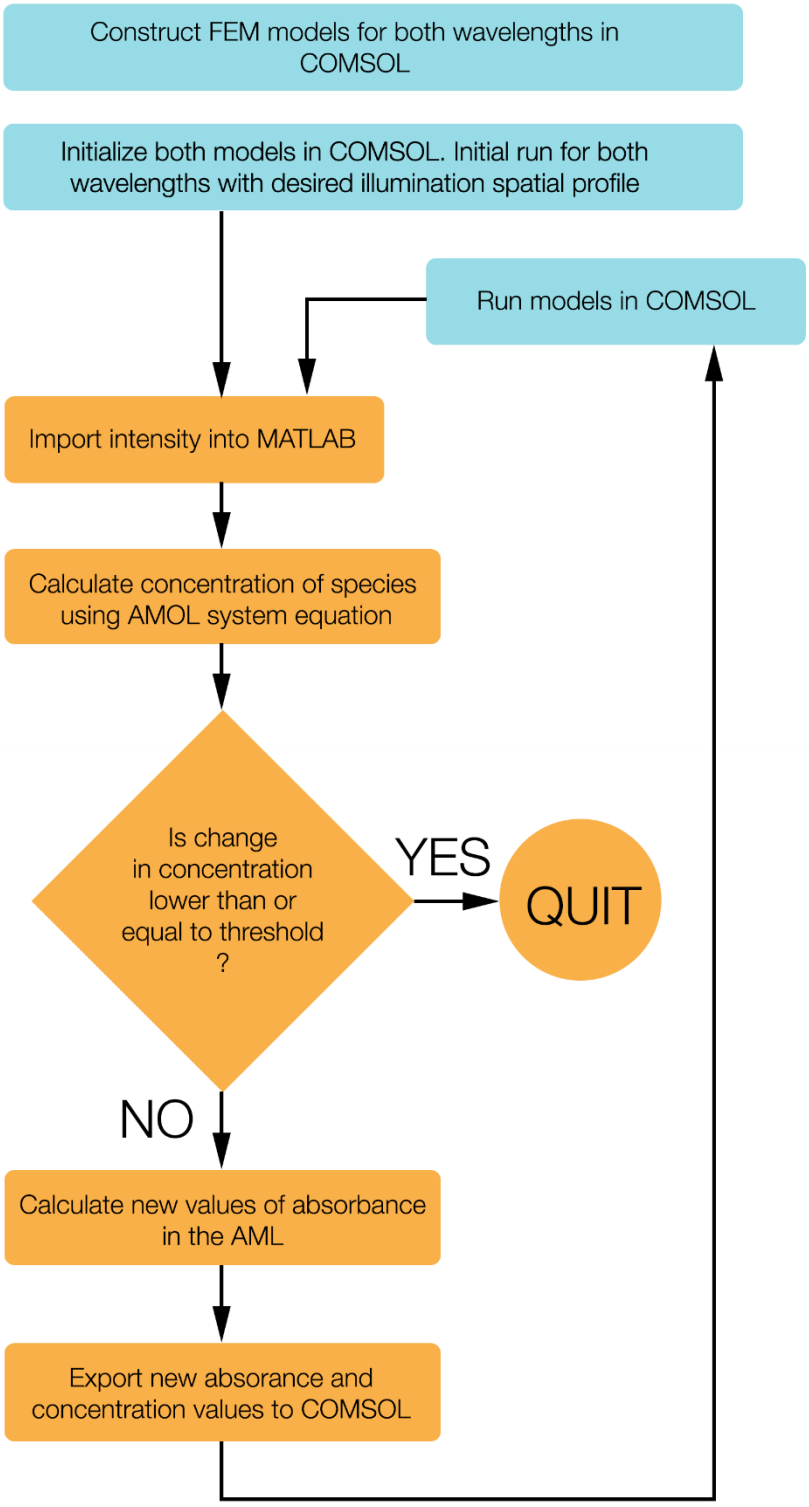

Figure 5.2: Algorithm to run the simulation for AMOL.

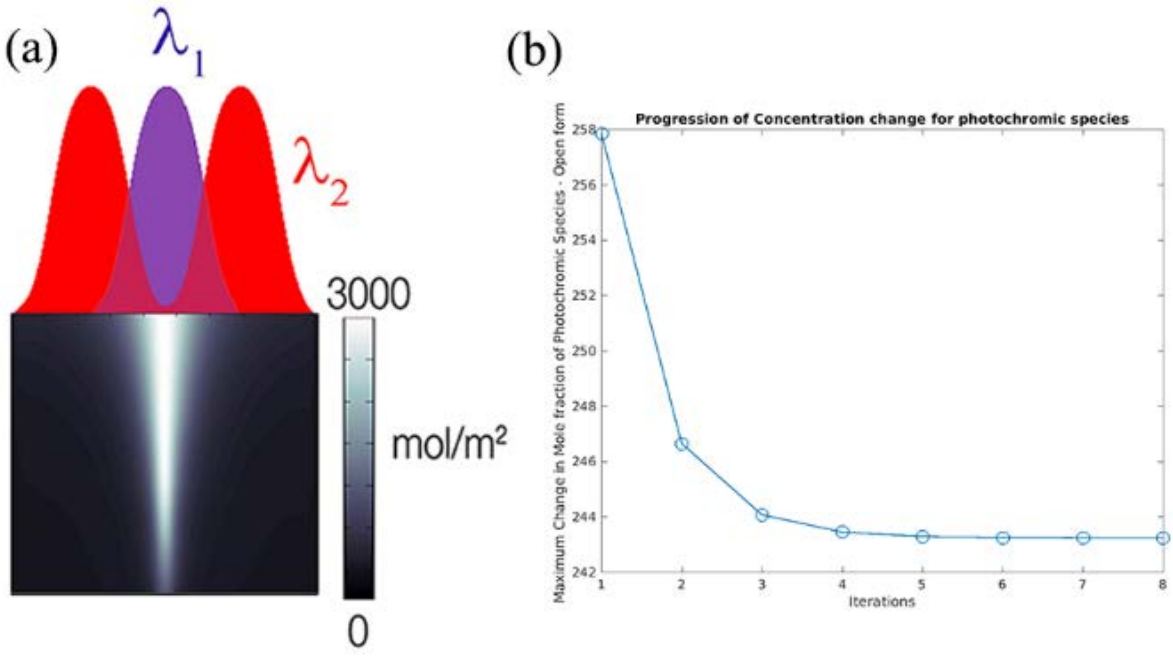

Figure 5.3: Exposure simulation for AMOL. (a) Aperture formation inside the AML. (b) Decrease in the change in concentration of the photochromic species for every iteration till threshold is reached indicating steady state.

5.6 References

1. R. Menon and H. I. Smith, "Absorbance-modulation optical lithography," *J. Opt. Soc. Am. A*, vol. 23, no. 9, Sep. 2006, pp. 2290-2294.

2. J. E. Foulkes, "Absorbance modulation optical lithography: Simulating the performance of an adaptable absorbance mask in the near-field," Doctoral Dissertation, University of Canterbury, 2010.

3. M. Warner and R. J. Blaikie, "Two-color nonlinear absorption of light in dye layers," *Phys. Rev. A*, vol. 80, no. 3, Sep. 2009, pp. 033833-1-6.

4. A. Majumder, P. J. Helms, T. L. Andrew, and R. Menon, "A comprehensive simulation model of the performance of photochromic films in absorbance-modulation-optical-lithography," *AIP Advances*, vol. 6, 035210, Mar. 2016, pp. 035210-1-8.

5. A. Majumder, F. Masid, B. J. Pollock, T. L. Andrew, and R. Menon, "Barrier free absorbance modulation for super-resolution optical lithography," *Opt. Exp.*, vol. 23, no.9, Apr. 2015, pp. 12244-12250.

6. T. L. Andrew, H-Y. Tsai, and R. Menon, "Confining light to deep sub-wavelength dimensions to enable optical nanopatterning," *Science*, vol. 324, no. 5929, May, 2009, pp. 917-921.

CHAPTER 6

A COMPREHENSIVE SIMULATION MODEL OF THE PERFORMANCE OF PHOTOCHROMIC FILMS IN ABSORBANCE-MODULATION-OPTICAL-LITHOGRAPHY

Reprinted with permission from: A. Majumder, P. J. Helms, T. L. Andrew, and R. Menon, "A comprehensive simulation model of the performance of photochromic films in absorbance-modulation-optical-lithography," *AIP Advances*, vol. 6, 035210, Mar. 2016, pp. 035210-1-8.

AIP ADVANCES **6**, 035210 (2016)

A comprehensive simulation model of the performance of photochromic films in absorbance-modulation-optical-lithography

Apratim Majumder,[1] Phillip L. Helms,[1] Trisha L. Andrew,[2] and Rajesh Menon[1,a]
[1]*Department of Electrical and Computer Engineering, University of Utah, Salt Lake City, Utah 84112, USA*
[2]*Department of Chemistry, University of Wisconsin-Madison, Madison, Wisconsin 53706, USA*

(Received 18 December 2015; accepted 2 March 2016; published online 14 March 2016)

Optical lithography is the most prevalent method of fabricating micro-and nano-scale structures in the semiconductor industry due to the fact that patterning using photons is fast, accurate and provides high throughput. However, the resolution of this technique is inherently limited by the physical phenomenon of diffraction. Absorbance-Modulation-Optical Lithography (AMOL), a recently developed technique has been successfully demonstrated to be able to circumvent this diffraction limit. AMOL employs a dual-wavelength exposure system in conjunction with spectrally selective reversible photo-transitions in thin films of photochromic molecules to achieve patterning of features with sizes beyond the far-field diffraction limit. We have developed a finite-element-method based full-electromagnetic-wave solution model that simulates the photo-chemical processes that occur within the thin film of the photochromic molecules under illumination by the exposure and confining wavelengths in AMOL. This model allows us to understand how the material characteristics influence the confinement to sub-diffraction dimensions, of the transmitted point spread function (PSF) of the exposure wavelength inside the recording medium. The model reported here provides the most comprehensive analysis of the AMOL process to-date, and the results show that the most important factors that govern the process, are the polarization of the two beams, the ratio of the intensities of the two wavelengths, the relative absorption coefficients and the concentration of the photochromic species, the thickness of the photochromic layer and the quantum yields of the photoreactions at the two wavelengths. The aim of this work is to elucidate the requirements of AMOL in successfully circumventing the far-field diffraction limit. [http://dx.doi.org/10.1063/1.4944489]

I. INTRODUCTION

In the micro- and nano-patterning industries the traditional methods of fabricating features close to or below the diffraction limit which is classically defined as about a third of the exposure wavelength,[1] are to employ extreme ultraviolet,[2] multiple exposure-and-etch mechanisms[3] or self-aligned patterning techniques.[4] All of these techniques achieve their goal at the cost of increased the processing time, expense and complexity.[5] Recently the diffraction limit has been broken in optical microscopy by techniques like stimulated-emission-depletion (STED) microscopy,[6] photo-activated-localization microscopy (PALM)[7] and stochastic-optical-reconstruction microscopy

[a]Email: rmenon@eng.utah.edu

(STORM).[8] Primarily inspired by STED, our approach to photolithography, termed absorbance-modulation-optical lithography (AMOL)[9,10] has been experimentally demonstrated[11–13] to possess patterning capabilities beyond the diffraction limit.

Past theoretical studies on AMOL were aimed at analyzing the photochemical processes using a kinetic model of the photochromic reaction.[14] However the role of diffraction of the light upon passage through the AML with complete solutions to Maxwell's equations were ignored. Nevertheless, it was a useful study on the effect of the material parameters on the confinement of the exposing beam PSF. There was also a full-vector finite-element model solved under photostationary conditions to analyze the effect of light polarization on the AMOL process.[15] The paper did not study the effect of changing the material parameters to influence the light absorbance within the AML.

Thus, in order to fully understand the effect of material characteristics in conjunction with the electromagnetic effects within the AML, we have resorted to a full-vector finite-element model that incorporates all the different parameters of interest in AMOL. These include the effects of light polarization and incident illumination patterns, the ratio of intensities of the confining and exposing beams, the thickness of the AML, the concentration of the photochromic species, the photoreaction quantum yields of the two states of the photochromes and their relative absorbances at the two wavelengths. Hence the model described here presents the most comprehensive picture to date, of the lithographic process in AMOL and its governing factors.

II. MODELING AND SIMULATION

The photochromic compounds used in AMOL that comprise the AML, switch between a form (closed form) that is transparent to an exposure wavelength (λ_1) and one (open form) that is opaque to it by exposure to a second wavelength (λ_2), as shown in Fig. 1(a). A lithographic exposure in AMOL is described using the geometry illustrated in Fig. 1(a). Typically the substrate is a silicon wafer on top of which a thin layer of photoresist is spun. The photoresist is the recording medium of the latent image of λ_1 (exposing beam). The AML is spun on top of this photoresist layer. Following sample preparation, two standing waves of λ_1 and λ_2 (confining beam) are incident on the sample such that the peaks of λ_1 are collocated with the nodes of λ_2. Under this illumination scheme, the competing action of the two beams converts the AML into the opaque state everywhere except at the node of the λ_2 beam and allows spatially confined photons of λ_1 to penetrate through this aperture and expose the photoresist layer. This two-dimensional geometry is consistent with our experiments.[13] In order to model and solve the photochemical reactions and the light-material interactions in this geometry, the finite-element method (FEM) (provided by commercial FEM software COMSOL, interfaced with MATLAB) was chosen due to its ability to effectively handle dispersive media and material-based inhomogeneities, and solve Maxwell's equations based on user defined material properties.

In modelling the photochemical reactions that occur within the AML, the following general hypotheses[11] are considered that have been separately verified in the past by experiments. The

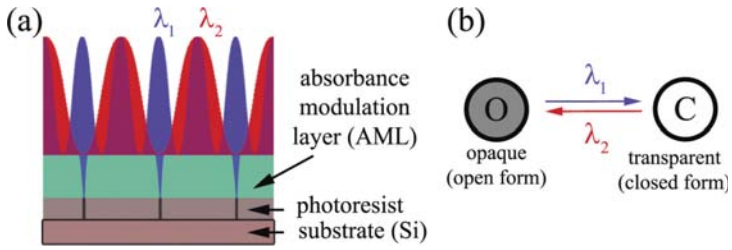

FIG. 1. (a) Schematic of AMOL showing simultaneous illumination of the AML by standing waves of λ_2 at 647 nm and λ_1 at 325 nm to render the AML opaque to only the regions under the λ_2 peaks. This system in conjunction with the photochemical interconversion of the two species shown above allows the photoresist to be exposed by only λ_1 photons that are restricted to dimensions below the diffraction limit. (b) UV-Vis spectrophotometry data showing the absorbance of the two forms (open and closed) at different wavelengths.

conversion from the open form of the photochrome (denoted by O) to the closed form (denoted by C) and the reverse reaction are only light driven upon the absorbance of wavelengths λ_1 and λ_2 respectively. Both states exhibit thermal stability as verified by previous experiments.[11–13] The absorbance data for these photochromes is shown in Ref. 16. In general, this conversion reaction follows first-order kinetics and the conversion rate of either species within the AML is dependent on the instantaneous molar concentration of the species (denoted $[O]$ or $[C]$), the intensity of the wavelength (I_1 for λ_1 and I_2 for λ_2), the molar absorptivity at the specific wavelengths (ε_{ij}, e.g. denoted by ε_{1O} for open form at λ_1) and the quantum yield of the photochemical reactions (φ_{ij}, e.g. denoted by φ_{OC} for conversion from open to closed form). Thus, assuming the two states are in dynamic equilibrium and following the approach adopted in previous work,[11,17] the rate equation for the photo-transition reaction is expressed as $-\frac{\partial[O]}{\partial t} = [O]I_1\varepsilon_{1O}\varphi_{OC} - [C]I_2\varepsilon_{2C}\varphi_{CO} - [C]I_1\varepsilon_{1C}\varphi_{CO}$. From the conservation of mass, we have $[O] + [C] = [O]_0$, where $[O]_0$ is the initial concentration under the assumption that the initial state is composed only of the open form. Solving this equation for the photostationary state where $\frac{\partial[O]}{\partial t} = 0$, the following expressions can be derived:

$$\frac{[C]}{[O]_0} = x_C = \frac{1}{1 + I_2/I_1\varepsilon_{2C}/\varepsilon_{1O}\varphi_{CO}/\varphi_{OC} + \varepsilon_{1C}/\varepsilon_{1O}\varphi_{CO}/\varphi_{OC}} \tag{1}$$

where x_C is the mole fraction for the closed form. The mole fraction of the open form is thus $x_O = (1 - x_C)$. It can be clearly seen that the material parameters that influence how much of the two photochromic species undergo conversion are not only the intensity ratio (I_2/I_1), but also the ratio of the molar absorptivity ($\varepsilon_{2C}/\varepsilon_{1O}$ and $\varepsilon_{1C}/\varepsilon_{1O}$) and the ratio of the quantum yields of the photochemical reactions ($\varphi_{CO}/\varphi_{OC}$). The overall absorbance ($\alpha_{\lambda i}$) at each wavelength can now be derived from the absorbance of the individual species ($\alpha_{\lambda iO}$ and $\alpha_{\lambda iC}$) as $\alpha_1 = \alpha_{1O}x_O + \alpha_{1C}x_C$ and $\alpha_2 = \alpha_{2O}x_O + \alpha_{2C}x_C$. This translates to the imaginary part of the refractive index for the AML for λ_1 as $k_1 = \alpha_1\lambda_1/4\pi$ and for λ_2 as $k_2 = \alpha_2\lambda_2/4\pi$. Additionally, the intensity of light for either wavelength inside the photochromic layer is given by Beer Lambert's law of the general form $\log\frac{I_1}{I_1} = \varepsilon cl$, where c and l are concentration and depth respectively. The different parameters corresponding to the AML are presented in Ref. 16.

III. RESULTS

A representative solution of the model constructed in COMSOL is shown in Fig. 2(a) with 100 nm thick AML and 60 nm thick photoresist and an intensity ratio of 2000. The full vector solutions of Maxwell's equations inside the AML reveals the exact light pattern, while the AMOL governing equations show the distribution of the photochromic species inside the depth of the AML. This knowledge cannot be acquired by scalar modelling considering only the intensity distribution on the top of the AML.[14] In order to explore the effect of light polarization and the incident illumination pattern on AMOL aperture formation, the polarization for λ_1 is varied between TE and TM. For λ_2 the polarization is kept fixed as TE for the highest contrast standing wave formation. The period for the λ_2 standing wave is taken as 325 nm, consistent with previous experiments.[11]

For λ_1, four types of spatial patterns are considered to demonstrate the effect of spatial arrangement of the two beams in AMOL: uniform illumination, standing waves with periods twice, equal to and half that of the λ_2 standing wave. Figs. 2(b) and 2(c) show the confinement achieved for the λ_1 PSF for these different illumination schemes and for different λ_1 polarizations. Exact variations of the λ_1 PSF with the intensity ratio for both polarizations is shown in Ref. 16. Good confinement can only be achieved with TM polarized writing beam, consistent with what has been previously reported.[15] Varying the period of λ_1 does not affect the final Full-width-half-maximum (FWHM) for either polarization to a great extent for TM polarization. The model shows that the system is able to resolve isolated features down to ~ 20 nm separated by the period of λ_2 standing wave. However multiple exposures can increase pattern resolution. A detailed discussion is presented in Ref. 16.

Although Fig. 2 indicates that the final FWHM value of the transmitted PSF of the exposing beam (λ_1) is independent of the spatial pattern of the incident beams, the FEM model reveals that for λ_1 period being half that of λ_2, suppressed peaks are formed (Fig. 3(a)) wherever peaks of both

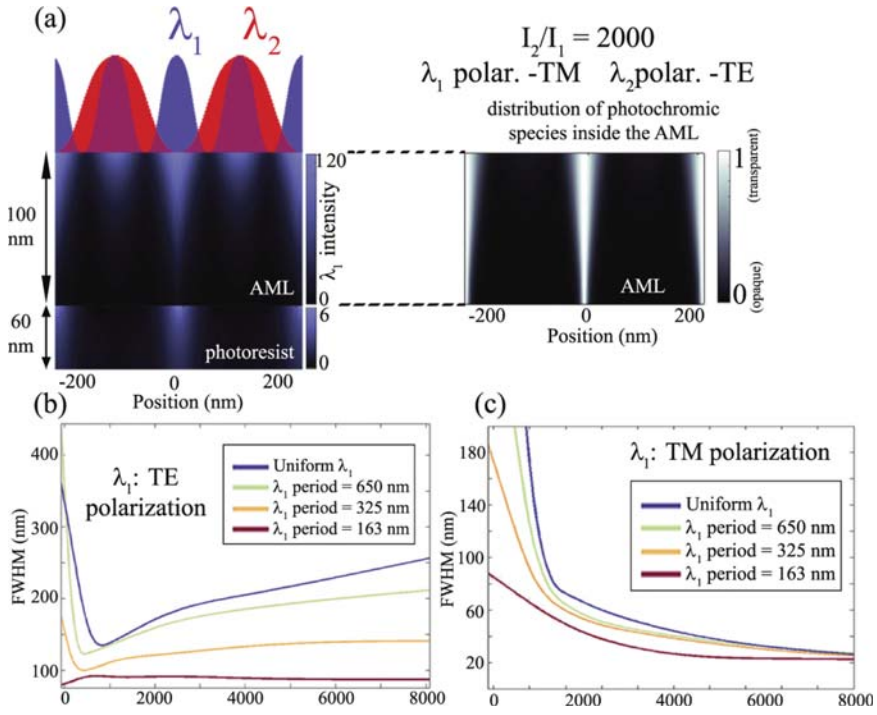

FIG. 2. (a) Results of the FEM model showing the λ_1 intensity and corresponding distribution of the photochromic species inside the AML for an intensity ratio of 2000 and TM polarized λ_1. (b)-(c) FWHM of transmitted PSFs of the λ_1 v/s different intensity ratios for TE and TM polarizations.

beams coincide. This was previously observed experimentally[11] and this is the first time it is being demonstrated with theoretical modelling. Three-dimensional PSFs that are of importance when patterning aperiodic two dimensional structures are provided in Ref. 16.

Uniform illumination seems to provide the sharpest PSF at the loss of some contrast (Fig. 3(d)). Hence it can be seen that the most important factor that governs the lithographic process in AMOL and allows for sub-diffraction confinement of the exposing beam is the ratio of the intensities i.e. I_2/I_1, predicting a FWHM linewidth of about 20-30 nm for an intensity ratio of about 6000. This is the most critical governing factor in AMOL and is similar to the scaling trend in STED microscopy. Unlike conventional photolithography, where the feature sizes scale with absolute intensity of the exposing beam, in AMOL the scaling occurs with respect to the intensity ratio. This introduces the nonlinearity effect required to successfully carry out double exposures without in between etch steps.

Since the absorption of λ_1, ideally at all locations other than the exact vicinity of the optical node at λ_2 is critical to improving the contrast of the lithographic procedure, clearly the concentration of the open form and hence the film thickness of the AML is expected to play an important role. A plot of the thickness of the AML versus the FWHM of the transmitted dose, for two intensity ratios 1000 and 4000 is shown in Fig. 4(a). Contrary to previous work using scalar theory[14] the FEM results reveal that the PSF FWHM does not monotonically decrease with increasing thickness but instead decreases till a certain thickness value before increasing again. The reason for this may be due to the fact that past a certain thickness even though the aperture in the AML shrinks to a FWHM of a few nanometers, there is not enough difference in the imaginary part of the refractive index between the open and closed forms for the light to shrink down further as shown in Fig. 4(c). Past this point the light behaves as if simply propagating through an effective medium and actually spreads out with an accompanied loss in contrast. Exact PSF scaling as shown in Ref. 16 also shows that the suppressed peaks are also observed to become more prominent. Figures 4(b) shows the

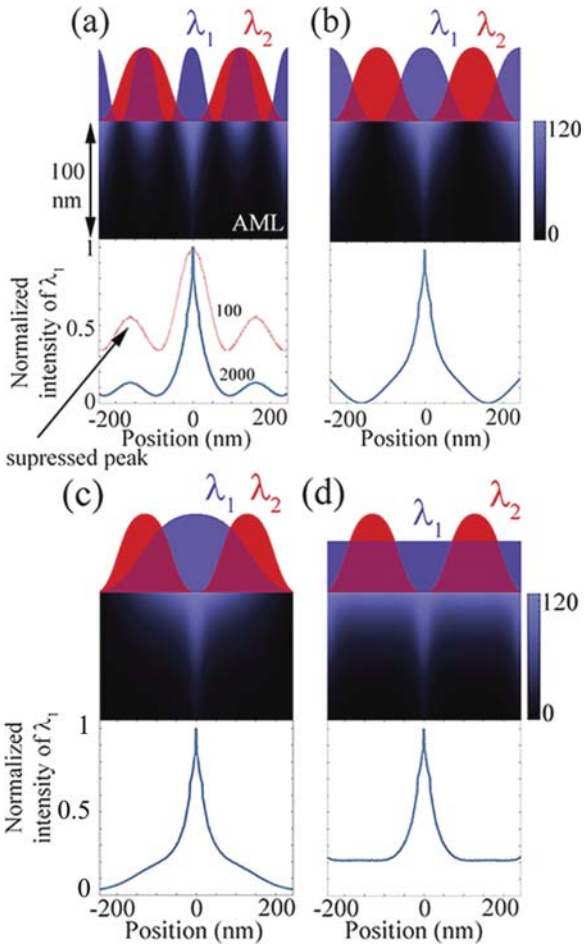

FIG. 3. (a)-(d) FEM solutions for different illumination schemes where the period λ_1 standing wave is varied. Suppressed peaks form where the peaks of both beams coincide. Contrast loss occurs for uniform λ_1 illumination.

effect of increasing the concentration of the photochromes in the AML. Increased concentration can achieve narrow PSFs at much lower AML thickness and intensity ratios. This work is currently being pursued using evaporated thin films of the photochromes[18] and photochromic polymers.

The third factor of interest are the two quantum yields of the photoreaction - from the open to the closed form and vice versa, i.e. φ_{OC} and φ_{CO}. It is indicated that good confinement can be achieved with intensity ratio as small as 10 provided that $\varphi_{CO}/\varphi_{OC}$ is high, as presented in Fig. 5(a), for a fixed AML thickness of 100 nm. Exact PSF behavior as shown in Ref. 16. However so far only the photochrome 1,2-bis(5,5' –dimethyl-2,2'-bithiophen-4-yl)perfluorocyclopent-1-ene (otherwise referred to as BTE) of the diarylethene family has been used in successful experiments and for that the φ_{CO} of 8.8×10^{-4} is several orders of magnitude lower than the φ_{OC} of 0.24. Synthesis of other diarylethene based molecules with more closely matched quantum yields in the future can yield better results in AMOL. Interestingly, at higher intensity ratios with higher values of $\varphi_{CO}/\varphi_{OC}$, the FWHM actually first decreases sharply and then increases since the aperture inside the AML approaches a negligible width and this appears simply as an effective medium to λ_1 photons, as shown in Fig. 5(b) where the distribution of the photochromes inside the AML are compared for intensity ratios of 10 and 100 and $\varphi_{CO}/\varphi_{OC}$ values of BTE and a hypothetical value of 0.2.

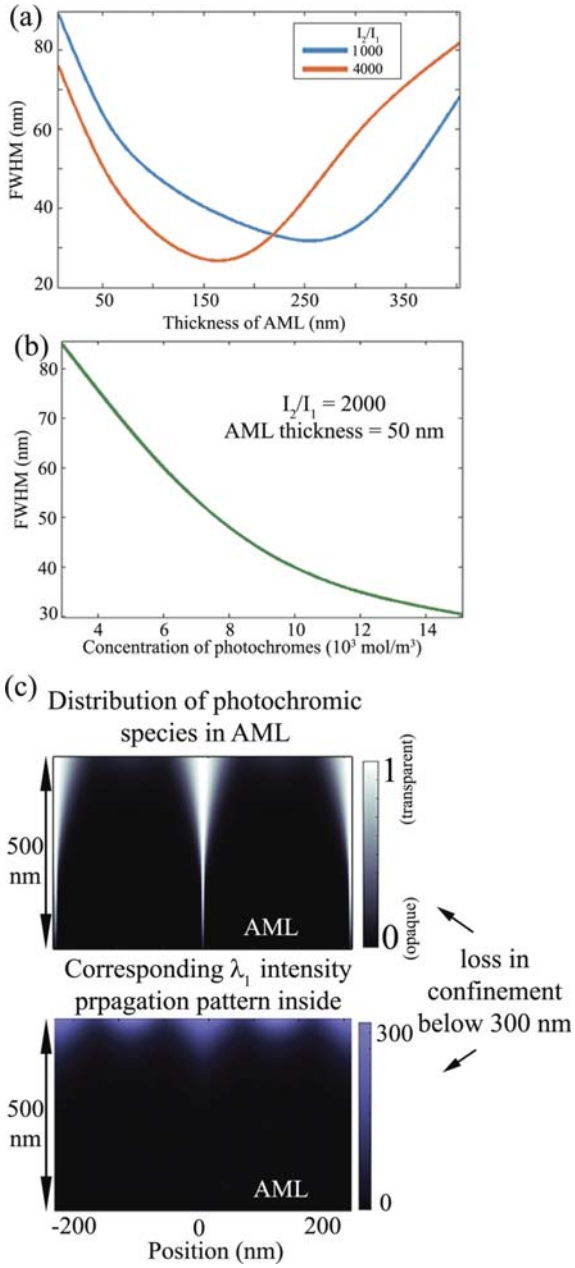

FIG. 4. (a) FWHM of λ_1 PSF v/s AML thickness. Contrary to previous work[14] FWHM does not monotonically decrease with increased AML thickness, rather reaches a minimum and then increases. (b) FWHM of λ_1 PSF v/s concentration of photochromes for an intensity ratio of 2000 and AML thickness of 50 nm. (c) FEM solutions showing the depth profile inside the AML for the AMOL aperture and corresponding exposing beam intensity. Loss of light confinement occurs at depths greater than 300 nm where the opacity difference becomes negligible.

The last parameter of interest, the molar absorptivity at the exposing wavelength shows the same trend as that seen in the case of quantum yield, contrary to previous work.[14] Basically increasing $\varepsilon_{1C}/\varepsilon_{1O}$ (the ratio of absorbances of the two species at the exposing beam) at first improves the contrast before the aperture inside the AML becomes negligible small for the light to guide through.

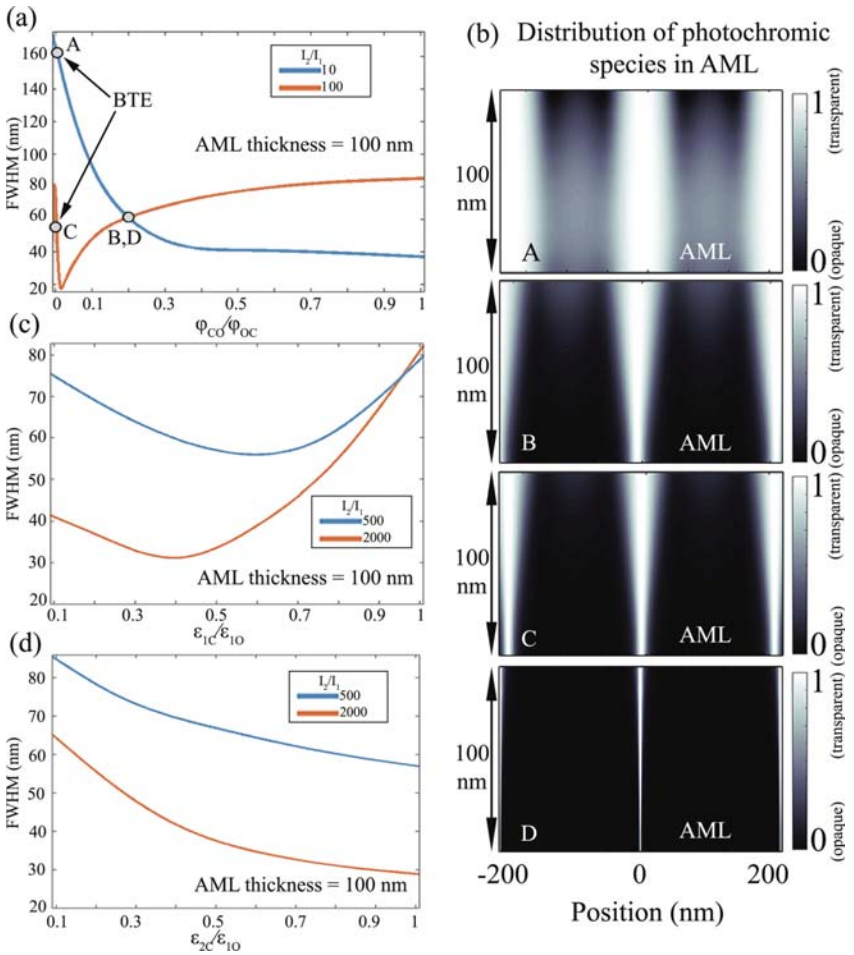

FIG. 5. (a) FWHM of λ_1 PSF v/s ratio of quantum yields. Contrary to previous work[14] FWHM does not monotonically decrease with increased quantum yield ratio for higher intensity ratios, rather reaches a minimum and then increases. (b) FEM solutions showing the depth profile inside the AML for the AMOL aperture and corresponding exposing beam intensity. (c) FWHM of λ_1 PSF v/s $\varepsilon_{1C}/\varepsilon_{1O}$. (d) FWHM of λ_1 PSF v/s $\varepsilon_{2C}/\varepsilon_{1O}$.

However the FWHM appears to monotonically decrease with increasing $\varepsilon_{2C}/\varepsilon_{1O}$ though the effect is far less pronounced since as equation (1) shows, the effect of this parameter is largely scaled by the intensity ratio, the value of which has a more profound influence on the AMOL process.

IV. CONCLUSION

This is most comprehensive and explanatory modelling of the AMOL process that clearly demonstrates the effect of the various parameters on the process. Increasing the intensity ratio of the two beams allows for greater confinement of the PSF but the effect can also be achieved at lower intensity ratios using photochromic material better suited to the process. The aim is to synthesize such materials with better matched quantum yields for the photokinetics.

ACKNOWLEDGEMENT

We would like to thank Benjamin J. Pollock at the University of Wisconsin-Madison and Farhana Masid and Precious Cantu at the University of Utah for helpful insight to the AML.

Financial support from NSF, DARPA and the Utah Science, Technology and Research (USTAR) initiative are also gratefully acknowledged.

[1] E. Abbé, Arch. Mikrosk. Anat. Entwichlungsmech **9**(1), 413–418 (1873).
[2] O. Wood *et al.*, Proc. SPIE **7271**, 727104 (2009).
[3] B. Haran *et al.*, Electron Devices Meeting (IEDM), 2008 IEEE International, 1-4 (2008).
[4] S. Natarajan *et al.*, Electron Devices Meeting (IEDM), 2014 IEEE International, 3.7.1-3.7.3 (2014).
[5] P. Zimmerman, SPIE Newsroom, 10.1117/2.1200906.1691, 1-3 (2009).
[6] S. W. Hell and J. Wichmann, Opt. Lett. **19**(11), 780–782 (1994).
[7] E. Betzig, J. K. Trautman, T. D. Harris, J. S. Weiner, and R. L. Kostelak, Science **251**(5000), 1468–1470 (1991).
[8] M. Rust, M. Bates, and X. Zhuang, Nature Methods **3**(10), 793–796 (2003).
[9] R. Menon and H. I. Smith, J. Opt. Soc. Am. A **23**(9), 2290-2294 (2006).
[10] R. Menon, Hsin-Yu Tsai, and S. W. Thomas III, Phys. Rev. Lett. **98**(4), 043905-1-4 (2007).
[11] T. L. Andrew, H.-Y. Tsai, and R. Menon, Science **324**, 917-921 (2009).
[12] F. Masid, T. L. Andrew, and R. Menon, Opt. Exp. **21**(4), 5209-5214 (2013).
[13] A. Majumder, F. Masid, B. J. Pollock, T. L. Andrew, and R. Menon, Opt. Exp. **23**(9), 12244-12250 (2015).
[14] G. Pariani, R. Castagna, R. Menon, C. Bertarelli, and A. Bianco, Opt. Lett. **38**(16), 3024-3027 (2013).
[15] J. E. Foulkes and R. J. Blaikie, J. Vac. Sci. Tech. B **27**, 2941-2946 (2009).
[16] See supplementary material at http://dx.doi.org/10.1063/1.4944489 for detailed analyses of photochromic behavior.
[17] M. Warner and R. J. Blaikie, Phys. Rev. A **80**(3), 03833 (2009).
[18] P. Cantu, T. L. Andrew, and R. Menon, App. Phys. Lett. **105**, 193105 (2014).

A comprehensive simulation model of the performance of photochromic films in Absorbance-Modulation-Optical-Lithography

Apratim Majumder,[1] Phillip L. Helms,[1] Trisha L. Andrew,[2] and Rajesh Menon[1,a)]

[1]*Department of Electrical and Computer Engineering, University of Utah, Salt Lake City, Utah 84112, USA*

[2]*Department of Chemistry, University of Wisconsin-Madison, Madison, Wisconsin 53706, USA*

Supplemental Material

I Absorbance Spectrum of the photochromic molecules

The photochromic molecules that comprise the AML in AMOL have the property of interconverting between a closed and an open form based on the absorbance of c (647 nm) or λ_1 (325 nm). The absorbance spectrum of these molecules along with the molecular composition of a specific type (1,2-bis(5,5' –dimethyl-2,2'-bithiophen-4-yl) perfluorocyclopent-1-ene (otherwise referred to as BTE, of the diarylethene family) that is used in our experiments is shown in Fig. S1.

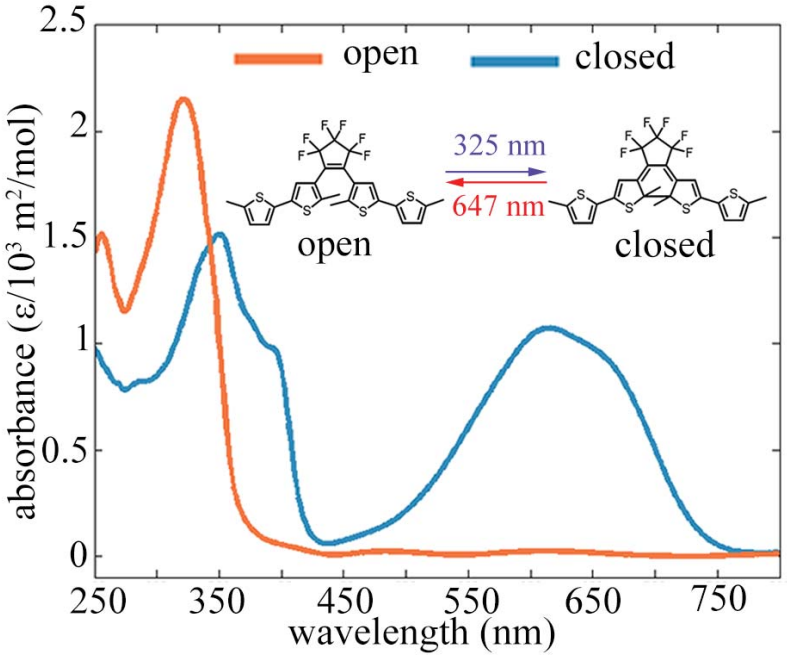

Fig. S1. UV-Vis spectrophotometry data showing the absorbance of the two forms (open and closed) at different wavelengths for BTE. (Inset) The molecular composition of BTE.

II Parameters of the AML

The different parameters that describe the AML such as the photoreaction quantum yields of the two states of the photochromes and their relative absorbances at the two wavelengths, the thickness of the AML, the concentration of the photochromic species, etc. are provided in Table SI.

Fig. SI. Different parameters of the AML

AML parameter	Value
Absorbance of open form to λ_1	$\varepsilon_{1O} = 3113.6\, m^2/mol$
Absorbance of closed form to λ_1	$\varepsilon_{1C} = 1052.1\, m^2/mol$
Absorbance of open form to λ_2	$\varepsilon_{2O} = 15.8\, m^2/mol$
Absorbance of closed form to λ_2	$\varepsilon_{2C} = 2003.5\, m^2/mol$
Photoreaction quantum yield (open to closed)	$\varphi_{OC} = 0.24$
Photoreaction quantum yield (closed to open)	$\varphi_{CO} = 8.8 \times 10^{-4}$
Concentration of photochromes	$6000\, mol/m^3$
Thickness of AML	100 nm

Additionally, the photoresist is modelled as a variable thickness material with a complex refractive index value of 1.6 – 0.5i at λ_1 and 1.6 – 0.005i at λ_2 (negligible absorbance in visible light). The substrate is modelled as a perfectly matched layer to mitigate all reflections. However it has been shown previously that reflective under layers possess the potential of positively influencing the imaging [1, 2].

III Confinement of λ_1 PSF with respect to intensity ratio

The confinement of λ_1 PSF with respect to intensity ratio is shown in Fig. S2. It can be seen that for a fixed spatial pattern as shown in Fig. 2, the PSF is confined to deep sub-diffraction dimensions for increasing intensity ratio between the confining and exposing beams. This confinement however depends on the polarization of λ_1 and is only possible when λ_1 is TM polarized. TE polarization offers no confinement. The dose required to expose the photoresist increases monotonically with increase in confinement as shown in Fig. S2(c).

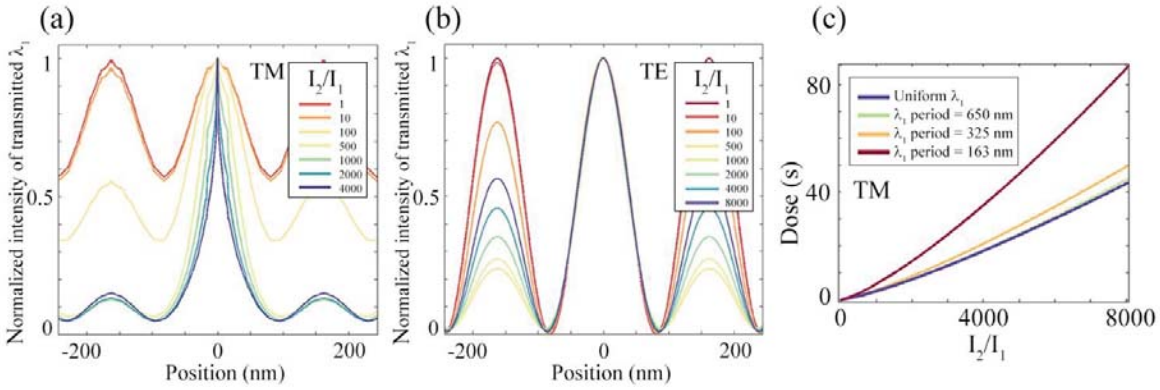

Fig. S2. (a-b) Transmitted PSFs of λ_1 for different intensity ratios for TM and TE polarizations respectively. (c) Photoresist dose v/s intensity ratio for TM polarized λ_1.

In order to pattern arbitrary aperiodic two dimensional structures, the arrangement of the two beams can be changed to a focal spot of λ_1 and a ring shaped spot of λ_2. This is similar to STED illumination arrangements. In that case the 3D PSF configuration becomes important. Fig. S3 shows how the λ_1PSF is confined in 3D.

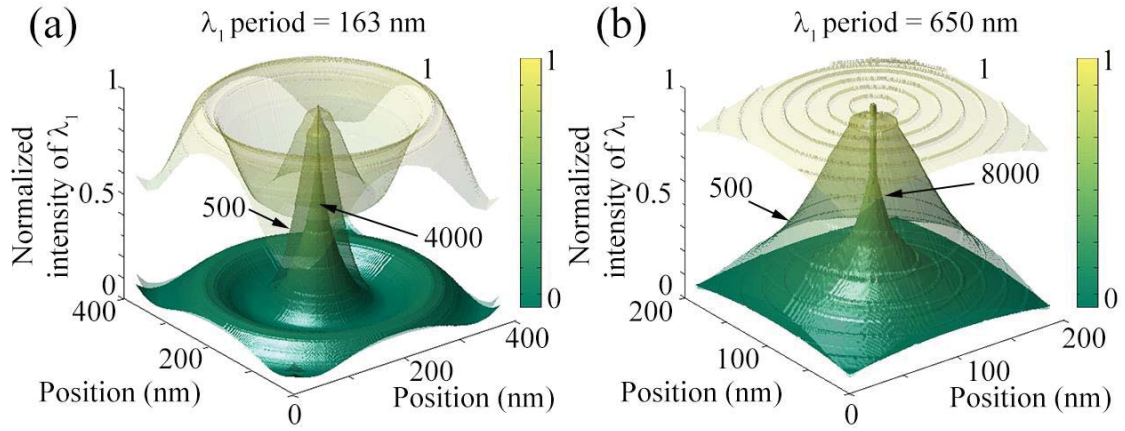

Fig. S3. (a-b) 3D PSFs for two of the four cases of illumination (Fig. 3(a-d)) showing how the PSF is confined for intensity ratios of 1, 500 and 4000 or 8000 respectively.

In the case of AMOL, as has been previously discussed [3] the diffraction limit should be defined with regards to λ_2 if λ_1 is uniform since the spatial pattern information is then contained only in the λ_1 beam. If however both the beams are patterned, i.e. in the form of standing waves with different periods, then the most robust definition of the diffraction limit would be with respect to both the wavelengths and since $\lambda_2 > \lambda_1$ then the limit is defined as $\lambda_1/2$. This translates to an absolute value of about 160 nm considering the exposure wavelengths used in our experiments. The model shows that the system is able to resolve isolated features down to ~ 20 nm. This has

also been previously experimentally demonstrated [4, 5]. Confining the PSF of the exposure down to these scales and restricting the light that illuminates the surrounding regions opens up the possibility of performing multiple exposures by simply translating the sample. In that case, multiplication of the patterns shown here (~20 nm features spaced $\lambda_2/2$ apart) can be achieved, thereby reducing the two-line resolution. Such work is currently being pursued for presentation in future.

IV Confinement of λ_1 PSF with respect to thickness of AML and concentration of photochromes

The confinement of λ_1 PSF with respect to increasing AML thickness for a fixed intensity ratio of 1000 is shown in Fig. S4(a). It can be seen that the PSF FWHM decreases till a certain thickness beyond which it increases. The explanation for this phenomenon can be found by inspecting the light pattern inside the AML as shown in Fig. 4. On the other hand the FWHM of the PSF decreases monotonically with increasing photochrome concentration as is expected. This is shown in Fig. S4(b).

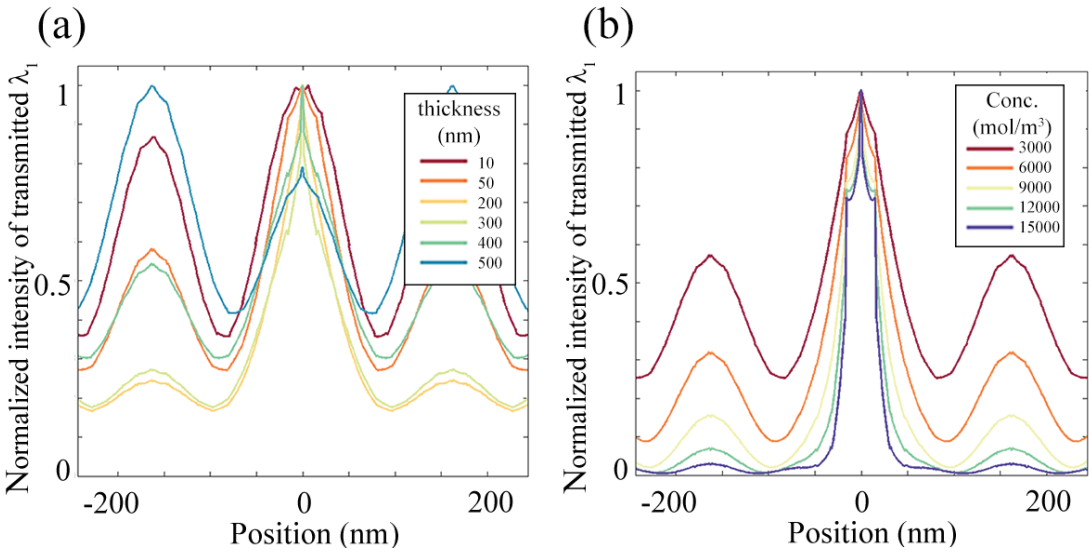

Fig. S4. (a) PSFs for different thickness of AML for a fixed intensity ratio of 1000 (b) PSFs for different concentrations of photochrome in the AML for a fixed intensity ratio of 1000.

IV Confinement of λ_1 PSF with respect to quantum yield of photoreaction

The confinement of the exposing beam PSF for a fixed intensity ratio of 10 and AML thickness of 100 nm is shown in Fig. S5. Good confinement can be achieved with even an intensity ratio as low as 10 given $\varphi_{CO}/\varphi_{OC}$ is sufficiently high.

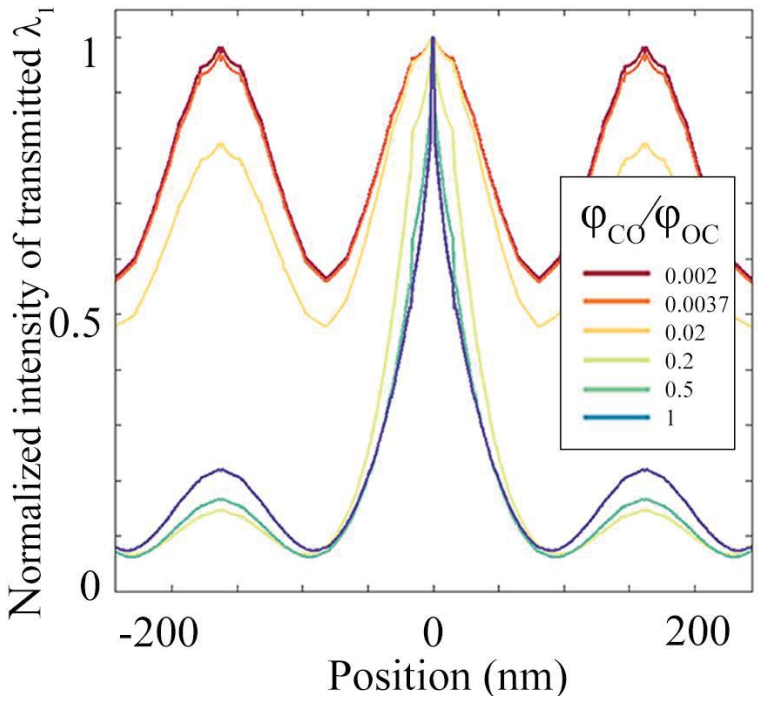

Fig. S5. λ1 PSF v/s $\varphi_{CO}/\varphi_{OC}$ for a fixed AML thickness of 100 nm and $I_2/I_1 = 10$.

References

[1]C. W. Holzwarth, J. E. Foulkes and R. J. Blaikie, Opt. Exp., 19(18) 17790-17798 (2011).
[2]J. E. Foulkes and R. J. Blaikie, J. Opt. Soc. Am. A, 28(11), 2209-2217 (2011).
[3]A. Majumder, F. Masid, B. J. Pollock, T. L. Andrew and R. Menon, Opt. Exp., 23(9), 12244-12250 (2015).
[4]T. L. Andrew, H.-Y. Tsai and R. Menon, Science, 324, 917-921 (2009).
[5]F. Masid, T. L. Andrew and R. Menon, Opt. Exp., 21(4), 5209-5214 (2013).

CHAPTER 7

REVERSE ABSORBANCE-MODULATION-OPTICAL-LITHOGRAPHY FOR OPTICAL PATTERNING AT LOW LIGHT LEVELS

Reprinted with permission from: A. Majumder, X. Wan, F. Masid, B. J. Pollock, T. L. Andrew, and R. Menon, "Reverse absorbance-modulation-optical-lithography for optical patterning at low light levels," *AIP Advances*, vol. 6, no. 065312, Jun. 2016, pp. 065312-1-6.

AIP ADVANCES **6**, 065312 (2016)

Reverse-absorbance-modulation-optical lithography for optical nanopatterning at low light levels

Apratim Majumder,[1,a,b] Xiaowen Wan,[1,b] Farhana Masid,[1] Benjamin J. Pollock,[2] Trisha L. Andrew,[2] Olivier Soppera,[3] and Rajesh Menon[1]

[1]*Department of Electrical and Computer Engineering, University of Utah, Salt Lake City, Utah 84112, USA*
[2]*Department of Chemistry, University of Wisconsin-Madison, Madison, Wisconsin 53706, USA*
[3]*Mulhouse Institute for Material Sciences, CNRS LRC 7228, BP2488, Mulhouse 68200, France*

(Received 12 April 2016; accepted 5 June 2016; published online 13 June 2016)

Absorbance-Modulation-Optical Lithography (AMOL) has been previously demonstrated to be able to confine light to deep sub-wavelength dimensions and thereby, enable patterning of features beyond the diffraction limit. In AMOL, a thin photochromic layer that converts between two states via light exposure is placed on top of the photoresist layer. The long wavelength photons render the photochromic layer opaque, while the short-wavelength photons render it transparent. By simultaneously illuminating a ring-shaped spot at the long wavelength and a round spot at the short wavelength, the photochromic layer transmits only a highly confined beam at the short wavelength, which then exposes the underlying photoresist. Many photochromic molecules suffer from a giant mismatch in quantum yields for the opposing reactions such that the reaction initiated by the absorption of the short-wavelength photon is orders of magnitude more efficient than that initiated by the absorption of the long-wavelength photon. As a result, large intensities in the ring-shaped spot are required for deep sub-wavelength nanopatterning. In this article, we overcome this problem by using the long-wavelength photons to expose the photoresist, and the short-wavelength photons to confine the "exposing" beam. Thereby, we demonstrate the patterning of features as thin as $\lambda/4.7$ (137nm for $\lambda = 647$nm) using extremely low intensities (4-30 W/m^2, which is 34 times lower than that required in conventional AMOL). We further apply a rigorous model to explain our experiments and discuss the scope of the reverse-AMOL process.
[http://dx.doi.org/10.1063/1.4954178]

I. INTRODUCTION

Optical lithography is arguably the key enabling technology of the semiconductor industry.[1–5] The diffraction limit[6] associated with all optical systems, has been circumvented by a number of techniques like self-aligned patterning techniques,[7,8] multiple exposure-and-etch mechanisms[9] and a number of other near-field methods[10–13] that have been inspired by techniques of super-resolution nanoscopy like stimulated-emission-depletion (STED).[14] Most of these techniques suffer from increased cost, complexity[15] or very high intensities.[11–13] Additionally, there has also been advances in pushing the resolution limit by employing plasmonics-based approaches,[16–18]

[a]E-mail: apratim.majumder@utah.edu
[b]These authors contributed equally to this work.

most of which require precise control of sample-mask gap since these are primarily near-field effect based techniques. Our approach to super-resolution nanopatterning, termed absorbance-modulation-optical lithography (AMOL)[19–21] has experimentally demonstrated patterning beyond the diffraction limit,[22–24] by enabling near-field lithography by means of far-field optics.

Traditionally, in AMOL, a thin layer of photochromic molecules called the absorbance modulation layer (AML), with the ability to reversibly photo-transition based on the wavelength of illumination (Fig. 1(a)), is used to achieve super-resolution nanopatterning. As illustrated in Fig. 1(b), a peak in the "exposing" beam (λ_1) and a node in the "confining" beam (λ_2) simultaneously illuminate the AML. The resulting photo-transitions in the AML effectively confine the "exposing" beam to a deep-subwavelength region, which exposes the underlying photoresist. In this case, the photoresist is chosen such that the "confining" beam does not affect it.

Diarylethenes such as 1,2-bis(5,5' –dimethyl-2,2'-bithiophen-4-yl) perfluorocyclopent-1-ene (otherwise referred to as BTE) are ideal molecules for the AML due to their stability. However, the quantum efficiency of the "exposing" reaction is about 3 orders of magnitude larger than that of the "confining" reaction.[22–24] This necessitates the intensity in the "confining" beam to be correspondingly larger for deep sub-wavelength patterning. Here, we avoid this problem by switching the wavelengths used for the "exposing" and "confining" beams, a technique we refer to as reverse-AMOL. The technique is illustrated on the right in Fig. 1(b). In this case, we need to utilize a photoresist that is sensitive to the longer wavelength, λ_2, while not being affected by the shorter wavelength, λ_1. The details of the experimental process are described later.

We first begin by using a previously developed rigorous model[21] to simulate the performance of reverse-AMOL. The model utilizes finite-element-method (FEM) (COMSOL interfaced with MATLAB) to model the photochemical reactions and light propagation that occur inside the AML.

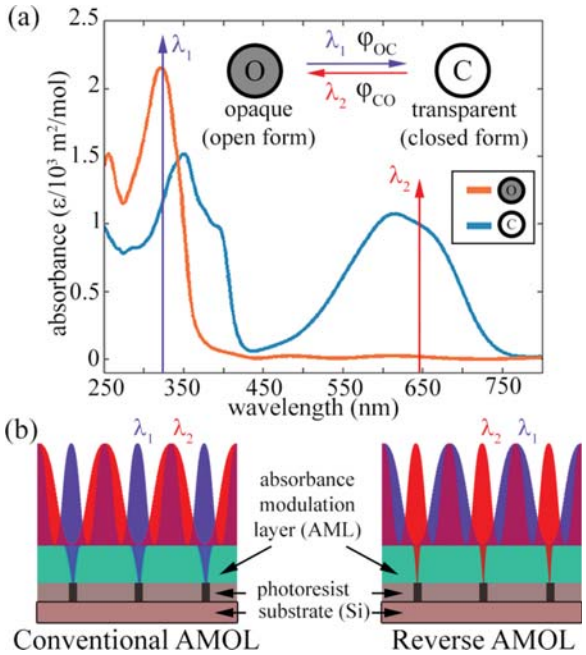

FIG. 1. (a) UV-Vis absorbance spectra of the diarylethene molecule, BTE showing the confining ($\lambda_2 = 647$ nm) and exposing beam ($\lambda_1 = 325$ nm) wavelengths. Reprinted with permission from AIP Advances 6, 035210 (2016). Copyright 2016 Author(s), licensed under a Creative Commons Attribution 4.0 License. (Inset) Scheme of the photoreaction. (b) Schematic of conventional AMOL showing simultaneous illumination of the AML by standing waves of λ_2 and λ_1. Reprinted with permission from AIP Advances 6, 035210 (2016). Copyright 2016 Author(s), licensed under a Creative Commons Attribution 4.0 License. Reverse-AMOL where the illumination scheme is reversed and λ_2 acts as the exposing beam and λ_1 acts as the confining beam.

Such a model has been previously used[21,25,26] to elucidate the effect of the material properties, light polarization, etc. in AMOL and demonstrated to be highly successful in handling dispersive and inhomogeneous media such as the AML and solving Maxwell's equations based on user defined material properties. Details of the model specific to reverse-AMOL and relevant mathematical derivations are described in the supplementary information.[27]

II. SIMULATION RESULTS

The simulation results are summarized in Figs. 2(a), 2(c), 2(e) and 2(f) for conventional AMOL and in Figs. 2(b), 2(d), 2(g) and 2(h), for reverse-AMOL. As has been described previously, the width of the exposed pattern (and thereby, the lithographic resolution) is inversely proportional to the ratio of the intensities in the two beams, I_2/I_1. The nature of this inverse relationship is determined primarily by the ratio of the quantum efficiencies of the two photo-reactions occurring inside the AML. As indicated in Fig. 2(a), $I_2/I_1 > 2000$ is required to achieve a minimum feature size of ~50nm for conventional AMOL. In comparison, a similar minimum feature size can be achieved with $I_1/I_2 = 2$ in the case of reverse-AMOL as indicated in Fig. 2(b). This is due to the fact that the "confining" reaction in this case is much more efficient than the "exposing" reaction and therefore, requires lower intensity in the "confining" beam. Detailed listing of the parameters of the simulations are included in the supplementary information.[27]

However, it is important to note that the ratio of quantum yields is not the only parameter that affects the minimum feature size. The aperture formation inside the AML is affected by two

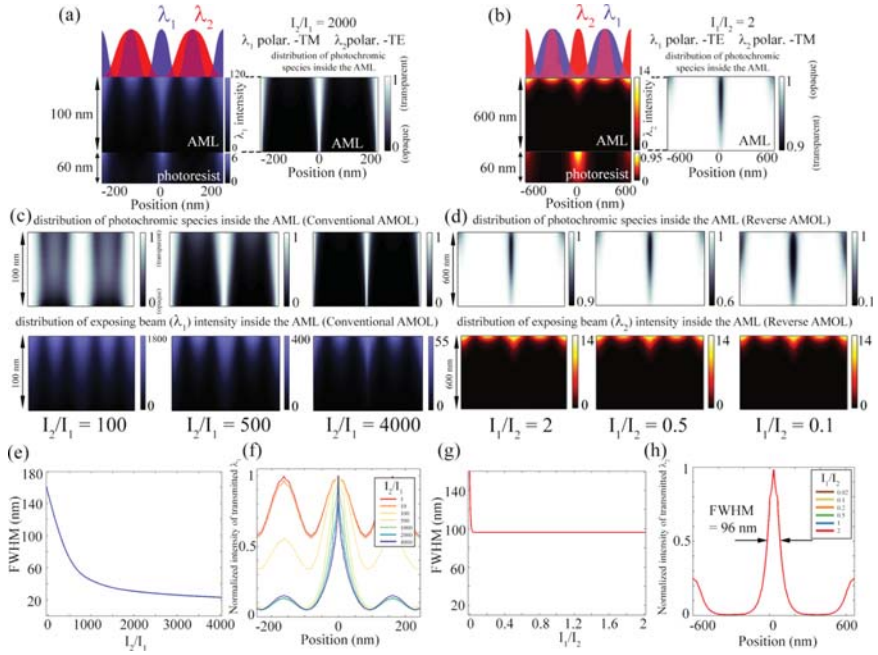

FIG. 2. Simulation results for the (a) conventional AMOL process. Reprinted with permission from AIP Advances 6, 035210 (2016). Copyright 2016 Author(s), licensed under a Creative Commons Attribution 4.0 License. (b) Simulation results for the reverse AMOL process showing the intensity distribution (λ_2) of the writing beam and the distribution of the photochromic molecules inside the AML. Modulation of the writing beam and the photochromic species distribution inside the AML for different intensity ratios for (c) conventional and (d) reverse AMOL. (e) FWMH (nm) v/s I_2/I_1 for conventional AMOL. Reprinted with permission from AIP Advances 6, 035210 (2016). Copyright 2016 Author(s), licensed under a Creative Commons Attribution 4.0 License. (f)Transmitted exposing beam point spread function (PSF) for conventional AMOL. Reprinted with permission from AIP Advances 6, 035210 (2016). Copyright 2016 Author(s), licensed under a Creative Commons Attribution 4.0 License. (g) FWMH (nm) v/s I_2/I_1 for conventional AMOL. (h) Transmitted exposing beam PSF for reverse AMOL.

phenomena. Firstly, the confinement of the writing beam through the AML is due to the modulation of its absorbance. Hence, the confining beam should be absorbed less compared to the writing beam inside the transparent form in order to maintain the aperture. This means that the ratio of molar absorptivities at the two wavelengths for the "confining" state of the AML, $\varepsilon_{1C}/\varepsilon_{2C}$,[27] must be greater than or close to 1 for conventional AMOL. For BTE, $\varepsilon_{1C}/\varepsilon_{2C} = 0.52$ (<1, but still not too low). On the other hand, for reverse-AMOL, this ratio is $\varepsilon_{2O}/\varepsilon_{1O} = 0.00507$, which turns out to be too low to create good absorbance contrast and a well-defined aperture in the AML for minimum features below about 96nm.

The second important parameter is the absorbance contrast at the exposing wavelength at the two states of the AML. This parameter is determined by the molar absorptivity ratio at the writing beam, which is $\varepsilon_{1C}/\varepsilon_{1O} = 0.33$ for BTE (conventional AMOL)[27] and $\varepsilon_{2O}/\varepsilon_{2C} = 0.0078$ for BTE (reverse-AMOL). Due to the lower absorbance contrast for reverse-AMOL, the achievable minimum feature size is limited to about 96nm for the parameters that we used in our experiments. Detailed explanations of the effect of these parameters on the AMOL process were discussed previously.[21] Figs. 2(c)-2(h) shows the combined effect of these parameters on the conventional and reverse-AMOL process. For conventional AMOL, the FWHM is modulated by I_2/I_1 effectively, with decreasing FWHM value for increasing I_2/I_1. However, this comes at the cost of high intensity ratios. For the reverse-AMOL process, confinement can be achieved down to ~100 nm at very low ratios.

Fig. 2(c) and 2(d) present comparisons between the apertures formed inside the AML for the conventional and reverse AMOL cases for different intensity ratios. Lastly, the modulation of the FWHM with intensity ratio is clearly observed in Fig. 2(e) for conventional AMOL, where sub-50 nm confinement can be achieved for $I_2/I_1 > 2000$, whereas, for reverse-AMOL in Fig. 2(g), ~ 90 nm FWHM is obtainable even with $I_1/I_2 < 1$, but no further modulation is possible. Fig. 2(f) and 2(h) show the actual point spread function (PSF) data corresponding to Fig. 2(e) and 2(g), respectively.

From the numerical analysis, we expect that in conventional AMOL very high intensities may be employed to minimum feature sizes down to ~ 30 nm.[22–24] However, due to the reasons laid out above, this is not strictly true for reverse-AMOL. As a result, the best confinement we can hope to achieve is about 96nm in reverse-AMOL, which corresponds ~ $\lambda_2/6$. It is very interesting to note that confinement in reverse-AMOL can be achieved even for $I_1/I_2 < 1$ (and therefore, very low powers), and this has been experimentally confirmed as described below.

III. EXPERIMENTAL RESULTS

The samples used in our experiments were prepared in two parts, one consisting of the BTE layer and the other with the photoresist as shown in Fig. 3(a). These two parts were prepared separately and then adhered to each other. Here, a 60 nm thick film of polyvinyl alcohol (PVA) served as the

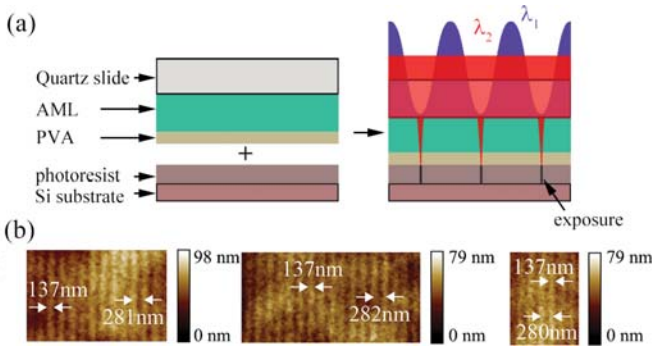

FIG. 3. (a) Schematic of the sample stack. The photoresist is spun onto silicon substrates and the AML is spun on quartz substrates with a thin layer of PVA on top of the AML acting as a barrier layer. The two parts are brought into close contact and then subjected to exposure in the dual wavelength AMOL system. (b) Atomic Force Microscope (AFM) images of the 1D gratings fabricated by reversed AMOL. For all three images, λ_1 to λ_2 peak intensity ratio I_1/I_2 is 0.139.

barrier layer between the two parts. PVA was chosen as the barrier layer material since it is mostly transparent in the entire wavelength range of interest[28] and can act as an excellent separating layer, while being chemically inert to both the AML and the photoresist. For the first part, a quartz substrate was spin-coated with a monolayer of hexamethyldisilazane (HMDS), 670 nm of AML and 60 nm of PVA acting as barrier layer. The second part of the sample was prepared by spin coating a layer of photoresist (details of the chemical composition of the photoresist have been presented in Ref. 27) on to silicon substrate. The photoresist layer could not be pre-baked, and remained a liquid film. The two parts were then adhered together prior to exposure and then separated after the exposure was concluded. The details of sample preparation and development are described in the supplementary information.[27]

The experiments were performed in a dual-wavelength Lloyd's-mirror interferometer with a standing wave created at λ_1 = 325nm with a period of ~280nm, and a uniform illumination at λ_2 = 647nm.[27] Fig. 3(b) shows atomic-force micrographs of the lines patterned using reverse-AMOL. Three different images were obtained from three different regions of the same sample. The average width of the lines is 137 nm, which is about one fifth of the exposing wavelength (647 nm). The intensity ratio (I_1/I_2) used was 0.139. This demonstrates that even with $I_1/I_2 < 1$, light confinement could be achieved by reverse-AMOL. Our simulations indicate that with this ratio, the printed feature should be about 100nm. We believe the discrepancy between the experiment and simulation is due to the fact that we do not obtain intimate contact between the AML and the photoresist, which allows the confined beam to diffract slightly before encountering the photoresist. Additionally, we performed simulations to study the effect of line-width broadening for the PSF due to the presence of the PVA barrier layer. This is presented in Fig. S2,[27] which shows considerable spread of the PSF due to increasing barrier layer thickness. When we consider the thickness of the PVA barrier layer (60 nm) and the resulted FWHM broadening, experimental results match pretty well with simulation predications that reversed AMOL can achieve a feature size below 150 nm. Note that the light intensity used here is 29 W/m^2 for λ_2 and 4 W/m^2 for λ_1, which is far smaller than that used in a typical AMOL process (~1kW/m^2 at λ_2).

IV. CONCLUSION

Due to the limitations of available photochromic molecules, AMOL requires high intensity ratios for sub-diffraction-limited patterning. Here, we demonstrate that this constraint can be overcome by simply reversing the wavelengths of the confining and exposing beams, a technique we refer to as reverse-AMOL. We performed careful simulations to elucidate the key parameters that impact the lithographic resolution of reverse-AMOL and gain the insight that the limiting factor for reverse-AMOL is different than that for conventional AMOL. We further performed experiments by choosing a "red-print" photoresist that exposes in the visible wavelength, but is unaffected by the UV wavelength. Our simulations and experiments suggest that in order to achieve feature sizes below 100nm, further optimization of the absorbance contrast of the photochromic molecule is necessary. Nevertheless, reverse-AMOL is able to achieve feature sizes of about $\lambda_2/5$ with intensities that are over a magnitude smaller than is required in conventional AMOL.

ACKNOWLEDGEMENTS

We would like to thank Chaitanya Ullal for helpful discussions regarding the AML and Brian Baker and Paulo Perez at the University of Utah for assistance with sample imaging. Support from NSF (Grant Number: 1054899) and the Utah Science, Technology and Research (USTAR) initiative are also gratefully acknowledged.

[1] K. Jain, IEEE Elect. Dev. Meeting **3**(1), 53-55 (1982).
[2] J. G. Maltabes *et al.*, SPIE Proc. **1262**, 2 (1990).
[3] W. Hinsberg *et al.*, J. Vac. Sci. Technol. B **16**, 3689 (1998).
[4] H. I. Smith, R. Menon, A. Patel, D. Chao, M. Walsh, and G. Barbastathis, Microelectron. Eng. **83**, 956-961 (2006).
[5] S. Owa, A. J. Hazelton, and H. H. Magoon, Microlithogr. World **16**, 4 (2007).
[6] E. Abbé, Arch. Mikrosk. Anat. Entwichlungsmech **9**(1), 413–418 (1873).

[7] J. Wu *et al.*, Langmuir **31**(17), 5005-5013 (2015).
[8] S. Natarajan *et al.*, Electron Devices Meeting (IEDM), 2014 IEEE International (2014) pp. 3.7.1-3.7.3.
[9] B. Haran *et al.*, Electron Devices Meeting (IEDM), 2008 IEEE International (2008) pp. 1-4.
[10] F. Huo *et al.*, Nature Nanotech **5**, 637-640 (2010).
[11] T. F. Scott *et al.*, Science **324**, 913-917 (2009).
[12] L. Li, R. R. Gattass, E. Gershgoren, H. Hwang, and J. T. Fourkas, Science **324**, 910-913 (2009).
[13] Z. Gan, Y. Cao, R. A. Evans, and Min Gu, Nature Comm. 4 **2061**, 1-7 (2013).
[14] S. W. Hell and J. Wichmann, Opt. Lett. **19**(11), 780–782 (1994).
[15] P. Zimmerman, SPIE Newsroom 1-3 10.1117/2.1200906.1691 (2009).
[16] X. Luo and T. Ishihara, Appl. Phys. Lett. **84**, 4780 (2004).
[17] X. Fang *et al.*, Science **308**, 534-537 (2005).
[18] P. Gao *et al.*, Appl. Phys. Lett. **106**, 093110 (2015).
[19] R. Menon and H. I. Smith, J. Opt. Soc. Am. A **23**(9), 2290-2294 (2006).
[20] R. Menon, Hsin-Yu Tsai, and S. W. Thomas III, Phys. Rev. Lett. **98**(4), 043905-1-4 (2007).
[21] A. Majumder, P. Helms, and R. Menon, AIP Advances **6**, 035210-1-8 (2016).
[22] T. L. Andrew, H.-Y. Tsai, and R. Menon, Science **324**, 917-921 (2009).
[23] F. Masid, T. L. Andrew, and R. Menon, Opt. Exp. **21**(4), 5209-5214 (2013).
[24] A. Majumder, F. Masid, B. J. Pollock, T. L. Andrew, and R. Menon, Opt. Exp. **23**(9), 12244-12250 (2015).
[25] J. E. Foulkes and R. J. Blaikie, J. Vac. Sci. Tech. B **27**, 2941-2946 (2009).
[26] M. Warner and R. J. Blaikie, Phys. Rev. A **80**(3), 03833 (2009).
[27] See supplementary material at http://dx.doi.org/10.1063/1.4954178 for details on mathematics related to simulations, sample preparation, optical setup and other details.
[28] S. D. C. Lowrey and R. J. Blaikie, J. Micro/Nanolith. **14**(4), 043510 (2015).

Reverse-Absorbance-Modulation-Optical Lithography for optical nanopatterning at low light levels

Apratim Majumder,[1,a),b)] Xiaowen Wan,[1,b)] Farhana Masid,[1] Benjamin J. Pollock,[2] Trisha L. Andrew,[2] Olivier Soppera[3], and Rajesh Menon[1]

[1]*Department of Electrical and Computer Engineering, University of Utah, Salt Lake City, Utah 84112, USA*

[2]*Department of Chemistry, University of Wisconsin-Madison, Madison, Wisconsin 53706, USA*

[3]*Mulhouse Institute for Material Sciences, CNRS LRC 7228, BP2488, Mulhouse 68200, France*

Supplemental Material

I Mathematical derivations required for construction of the AMOL model in COMSOL

It has been previously demonstrated [1] that TE polarized confining beam and TM polarized exposing beam is the optimum illumination scheme for the AMOL system. The only assumptions considered are that the photoreactions are light driven and that either species is thermally stable [2]. The conversions follow first order kinetics and the conversion rate of either species within the AML is dependent on the instantaneous molar concentration of the species (denoted [O] or [C]), the intensity of the two beams (I_1 and I_2), the molar absorptivity at the specific wavelengths (ε_{ij}, e.g. denoted by ε_{1O} for open form at λ_1) and the quantum yield of the photochemical reactions (φ_{OC} and φ_{CO}). For the case of conventional AMOL, assuming the two states are in dynamic equilibrium and following the approach adopted in previous work [1-4], the rate equation for the photo-transition reaction is expressed as $-\frac{\partial[O]}{\partial t} = [O]I_1\varepsilon_{1O}\varphi_{OC} - [C]I_2\varepsilon_{2C}\varphi_{CO} - [C]I_1\varepsilon_{1C}\varphi_{CO} + [O]I_2\varepsilon_{2O}\varphi_{OC}$, where initial concentration is assumed to be composed of only the open form $[O]_0$ i.e. $[O] + [C] = [O]_0$. In addition, it has been confirmed [2] that λ_2 photons are not sufficiently energetic to trigger the open-to-closed photoreaction; hence $[O]I_2\varepsilon_{2O}\varphi_{OC} = 0$. Solving this equation for the photo-stationary state where $\frac{\partial[O]}{\partial t} = 0$, the following expressions can be derived:

$$\frac{[C]}{[O]_0} = x_C = \frac{1}{1+{}^{I_2}/_{I_1}\,{}^{\varepsilon_{2C}}/_{\varepsilon_{1O}}\,{}^{\varphi_{CO}}/_{\varphi_{OC}} + {}^{\varepsilon_{1C}}/_{\varepsilon_{1O}}\,{}^{\varphi_{CO}}/_{\varphi_{OC}}} \qquad (1)$$

where x_C is the mole fraction for the closed form. The mole fraction of the open form is thus $x_O = (1 - x_C)$.

---

a) Email: apratim.majumder@utah.edu

b) These authors contributed equally to this work.

Now if the scheme of illumination was to be reversed, i.e. the ratio of the intensity of confining to exposing beam becomes I_1/I_2 as shown in Fig 1(b) and the assumptions accordingly updated so that the initial composition comprised only of the closed form: $[O] + [C] = [C]_0$, the above rate equation can be accordingly changed to $-\frac{\partial[C]}{\partial t} = [C]I_2\varepsilon_{2C}\varphi_{CO} - [O]I_1\varepsilon_{1O}\varphi_{OC} - [O]I_2\varepsilon_{2O}\varphi_{OC} + [C]I_1\varepsilon_{1C}\varphi_{CO}$. Again since $[O]I_2\varepsilon_{2O}\varphi_{OC} = 0$, solving for the photo-stationary state yields the solution:

$$\frac{[O]}{[C]_0} = x_O = \frac{I_1/I_2 + \varepsilon_{2C}/\varepsilon_{1C}}{I_1/I_2 + \varepsilon_{2C}/\varepsilon_{1C} + I_1/I_2 \; \varepsilon_{1O}/\varepsilon_{1C} \; \varphi_{OC}/\varphi_{CO}} \qquad (2)$$

Again $x_C = (1 - x_O)$. Now, following the method in [3, 4] the absorbance of the individual species ($\alpha_{\lambda iO}$ and $\alpha_{\lambda iC}$) is derived, and from the relations $\alpha_1 = \alpha_{1O}\, x_O + \alpha_{1C} x_C$ and $\alpha_2 = \alpha_{2O}\, x_O + \alpha_{2C} x_C$, the overall absorbances ($\alpha_{\lambda i}$) at each wavelength is calculated. Next, the imaginary part of the refractive index, responsible for light absorption inside the AML is calculated for λ_1 as $k_1 = \alpha_1\lambda_1/4\pi$ and for λ_2 as $k_2 = \alpha_2\lambda_2/4\pi$. Beer Lambert's law is used to derive the intensity of light for either wavelength inside the photochromic layer as $\log\frac{I_0}{I} = \varepsilon c l$, where c and l are concentration and depth respectively. For simulation purposes, the AML was modeled using values measured for BTE. The values are presented in Section III.

In order to realize the reversed illumination scheme for AMOL (reverse-AMOL), a photoresist was required that could be exposed at λ_2 = 647 nm. The photoresist used here consisted of the photoinitiator Methylene Blue that has strong absorbance at λ_2. It also has some though not significant absorbance at λ_1. Based on the UV-Vis spectrophotometry response of the photoinitiator, the photoresist was hence, modeled as a variable thickness material with a complex refractive index value of 1.6 – 0.7i at λ_2, which is now the exposing beam and 1.6 – 0.05i at λ_1, the confining beam in this case.

II Absorbance Spectrum of photoinitator Methylene Blue

The reverse-AMOL requires a pattern recording medium at λ_2 = 647 nm. Hence, the photoresist used here consisted of the photoinitiator Methylene Blue [5, 6] that has strong absorbance at λ_2. It also has some though not significant absorbance at λ_1. The UV-Vis spectrophotometry response of Methylene Blue is shown in Fig. S1.

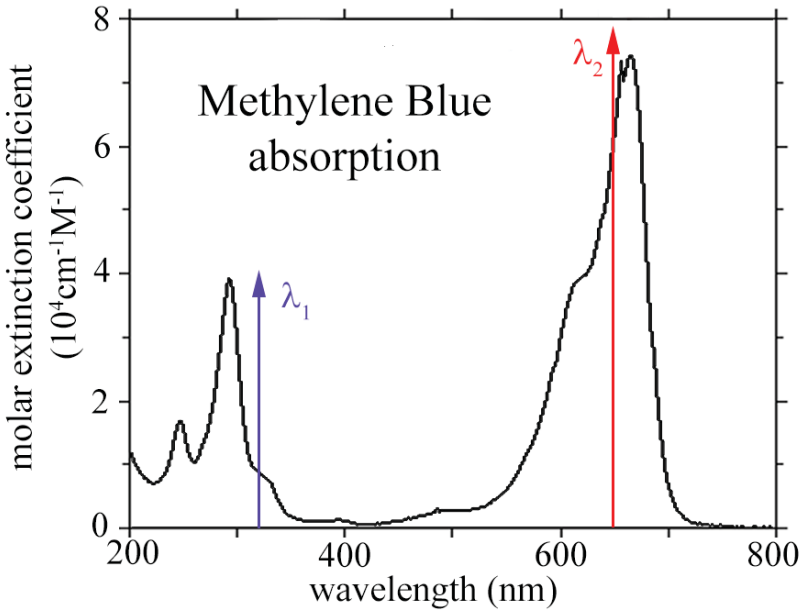

Fig. S1. (a) UV-Vis absorbance spectra of the photoinitiator Methylene Blue showing high absorbance at λ_2 with peak absorbance at 656 nm. There is some though not significantly enough absorbance at λ_1 (325 nm).

III Parameters of the AML

The different parameters that describe the AML have been tabulated in Table SI. These parameters primarily describe the response of the material to the exposing and confining beams and include their relative absorbances at the two wavelengths, the photoreaction quantum yields of the two states of the photochromes, the thickness of the AML, the concentration of the photochromic species, etc.

The substrate is modelled as a perfectly matched layer to mitigate all reflections. However it has been shown previously that reflective under layers possess the potential of positively influencing the imaging [7, 8].

Table SI. Different parameters of the AML.

AML parameter	Value
Molar absorptivity of open form to λ_1	$\varepsilon_{1O} = 3113.6\ m^2/mol$
Molar absorptivity of closed form to λ_1	$\varepsilon_{1C} = 1052.1\ m^2/mol$
Molar absorptivity of open form to λ_2	$\varepsilon_{2O} = 15.8\ m^2/mol$
Molar absorptivity of closed form to λ_2	$\varepsilon_{2C} = 2003.5\ m^2/mol$
Photoreaction quantum yield (open to closed)	$\varphi_{OC} = 0.24$
Photoreaction quantum yield (closed to open)	$\varphi_{CO} = 8.8 \times 10^{-4}$
Concentration of photochromes	$6000\ mol/m^3$
Thickness of AML	600 nm

IV Absorbance Modulation Layer (AML) formulation

The photochromic molecule 1,2-bis(5,5' –dimethyl-2,2'-bithiophen-4-yl) perfluorocyclopent-1-ene (BTE) was synthesized following methods previously described [2]. In order to spin cast the molecule as the absorbance modulation layer (AML) it was required to suspend the molecule in a polymer matrix. Polystyrene was chosen as this polymer matrix due to its low absorbance to the two beams. The absorbance peaks of polystyrene occur below 300 nm [9-10]. A solution of 30 mg/mL of Polystyrene in Toluene was first prepared. Next, to this the BTE molecule was doped at 93.63 weight percent.

V Details of sample preparation

The sample used in the experiments were prepared in two parts. A barrier layer was required to be present between the AML and the photoresist layer since the photoresist is attacked by the solvent of the AML, Toluene. Here, a 60 nm thick film of polyvinyl alcohol (PVA) served as the barrier layer between the two parts. Detailed analyses of the effect of the barrier in the system in presented in Section VII.

The photoresin used in the experiments is a type of molecularly imprinted polymers (MIP) acting as red-print photoresist (exposes at 647 nm – the exposing beam). MIPs are widely applied in biosensors [11, 12], chemical sensors [13] and drug delivery [14]. Here, the selected red-light-sensitive photoresin includes three components: methylene blue (MB) as the initiator, N-methyldiethanolamine (MDEA) as the co-initiator and dipentaerythritol pentaacrylate (SR399) as the monomer. The initiator MB has an absorption peak at around 656 nm, as described in Section II, which indicates that the photoresin is sensitive to red light. The wavelength of the red light we

used for reversed AMOL exposures is 647 nm, which matches well with the absorption peak of MB initiators. A photo induced free radical polymerization (FRP) takes place when the red-print photoresin is exposed by red light [11]. FRP is a three-step process, which includes initiation, propagation and termination. In the first step, free radicals are generated due to light initiation and photoreactions occur between initiator (MB) and co-initiator (MEDA). Then free radicals are added onto SR399 monomers to form chain-initiating radicals. In the propagation step, more and more monomers are added onto intermediate radicals until high-molecule-weight macromolecules are formed. Macromolecules becomes bigger and bigger until the polymerization terminates. The resulting polymer has a different solubility than that of unpolymerized photoresin. Therefore, patterns can be printed.

Prior to sample preparation, the quartz and silicon substrates were subjected to cleaning using RCA and Piranha agents.

As shown in Fig. 3(a) the sample used in the experiments consisted of two parts:

1. Part with AML: This was prepared by using quartz as the substrate. Quartz was chosen as the substrate for the part of the sample with AML due to its low absorbance to the two wavelengths of interest. The quartz substrate was spin-coated with a monolayer of Hexamethyldisilazane (HMDS) at 6000 RPM for 60 s, followed by the AML at 730 RPM for 60 s to form a 670 nm layer. The AML was air dried for 10 min. Lastly PVA (dissolved in water at 4 percent by weight) was spun on top at 6000 RPM for 60 s to form a 60 nm thick barrier layer.

2. Part with photoresist: The photoresist was directly spun onto the silicon substrate at 6000 RPM for 60 s. Due to the nature of the chemistry of the photoresist, it could not be baked but remained as a liquid film.

VI Sample development

After the reversed AMOL exposures, the AML part and the photoresist part were separated from each other. The photoresist part was then post baked on a hotplate at 180℃ for 10 mins. After the post bake, the photoresist part was immersed in ethanol (anhydrous, ≥ 99.5%) for 1min to be developed. Finally, the photoresist part was rinsed in DI water for 15 s and dried.

VII Effect of PVA barrier layer on the reverse-AMOL process

In order to illustrate the effect of the barrier layer in the system we incorporated a layer of PVA of refractive index 1.5 + 0i and variable thickness into the simulation model and recalculated the light fields transmitted through it. Fig. S2(a) illustrates that the evanescent high-spatial frequency components decay exponentially away from the AML aperture into the PVA layer thereby both increasing the FWHM linewidth as well as decreasing the peak intensity exponentially, thereby leading to a tremendous loss in contrast. This is shown in Fig. S2(b). Hence, for best results it is imperative that the barrier layer be kept as thin as possible.

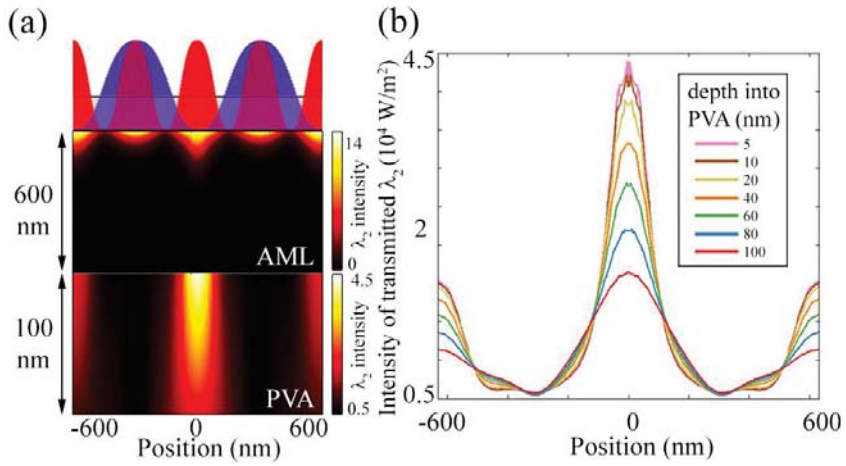

Fig. S2. (a) Intensity distribution inside the barrier layer (PVA). (b) Cross-sections of the λ_2 intensity inside different depths of the barrier layer.

VIII Details of the optical set-up used to perform reversed AMOL lithographic exposures

The schematic of optical setup for reversed AMOL is shown in Fig. S3. The well-known Lloyd's mirror interferometer setup was used for generating λ_1 standing wave. Specifically, half of the incident uniform UV light (325 nm) arrived at the mirror while the other half at the substrate. The former half was reflected by the mirror and interfered with the latter one to generate UV standing wave on the sample substrate surface. The period of the λ_1 standing wave = $\lambda_1/2n\sin\theta$, where n is the refractive index of the medium that the light is travelling through and θ is the angle between the mirror and the incident beam. Here, n = 1, and $\theta = 37°$. The period of UV standing wave is calculated to be 270 nm. Uniform λ_2 (647 nm) was generated by blocking half of the red light spot. Note that spatial filters were introduced to collimate, expand and clean the laser beams. We used uniform λ_2 instead of standing wave in order to simplify the experimental set-up and avoid critical

standing wave alignment procedures. It has been demonstrated previously through extensive simulations [1] as well as experiments [2] that the effect of changing the period of the exposing beam on the final AMOL point spread function (PSF) in the photoresist is negligible.

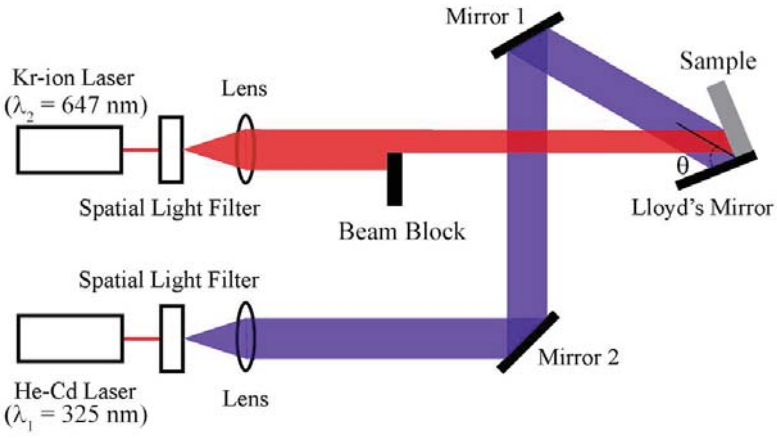

Fig. S3. Schematic of the Lloyd's mirror interferometer setup to perform reversed AMOL exposures.

References

[1]A. Majumder, P. Helms and R. Menon, AIP Advances, 6, 035210-1-8 (2016).
[2]T. L. Andrew, H.-Y. Tsai and R. Menon, Science, 324, 917-921 (2009).
[3]J. E. Foulkes and R. J. Blaikie, J. Vac. Sci. Tech. B, 27, 2941-2946 (2009).
[4]M. Warner and R. J. Blaikie, Phys. Rev. A, 80(3), 03833 (2009).
[5]Y. Fuchs, O. Soppera and K. Haupt, Analytica Chemica Acta, 717, 7–20 (2012).
[6]K. S. Padon and A. B. Scranton, J. Polym. Sci. Part A: Polymer Chemistry, Vol. 38, 2057–2066 (2000).
[7]C. W. Holzwarth, J. E. Foulkes and R. J. Blaikie, Opt. Exp., 19(18) 17790-17798 (2011).
[8]J. E. Foulkes and R. J. Blaikie, J. Opt. Soc. Am. A, 28(11), 2209-2217 (2011).
[9]T. Li, C. Zhou and M. Jiang, Polymer Bulletin, 25, 211-216 (1991).
[10]A. Majumder, F. Masid, B. J. Pollock, T. L. Andrew and R. Menon, Opt. Exp., 23(9), 12244-12250 (2015).
[11]K. Haupt, K. Noworyta and W. Kutner, Anal. Commun. 36, 391 (1999).
[12]P. Cywinski, M. Sadowska, A. Danel, W.J. Buma, A.M. Brouwe and B. Wandelt, J. Appl. Polym. Sci. 105, 229 (2007).
[13]K. Haupt and K. Mosbach, Chem. Rev. 100, 2495 (2000).
[14]N.X. Wang, H. A. von Recum, Macromol. Biosci. 11, 321 (2011).

CHAPTER 8

AMOL AT LOW LIGHT INTENSITY USING QUANTUM YIELD MATCHED PHOTOCHROMES

8.1 Introduction

One of the main drawbacks of AMOL is the fact that the confining beam requires very high intensity in order to effectively confine the exposing beam to dimensions smaller than the far-field diffraction limit. This is because in diarylethene, the species of photochromic molecules most commonly used in AMOL, the quantum yield of the photoreaction is highly dissimilar, leading to the requirement of high illumination intensities. However, it was shown in Chapter 6 and [1] that molecules with closely matched quantum yields may be able to confine light more efficiently in AMOL, leading to the usage of low intensity light levels. In this chapter, the structures and properties of other photochromic species that have better tuned quantum yield values and different responses to different wavelength regions are described with accompanying simulation and modelling data are provided to demonstrate their potential applicability to AMOL. Some experimental results are also presented.

8.2 Photochromic Molecules with Better Matched Quantum Yields

From equations 5.1 and 5.3, it is clear that lower intensity ratios can be used to achieve the phenomenon of subdiffraction patterning in AMOL if the quantum yields

of the two photoreactions are favorably balanced. Recently it has become possible by the efforts of Trisha L. Andrew and Benjamin J. Pollock at the University of Massachusetts Amherst to synthesize a new photochromic molecule [1,2-bis(2-methyl-5-(p-cyanophenyl)-3-thienyl)-3,3,4,4,5,5-hexafluoro-1-cyclopentene] (otherwise referred to as cPTE) with favorable quantum yields. Fig 8.1 shows the structure of this molecule in the open and closed states and its UV-Vis spectrophotometry response. cPTE has a quantum yield of the closed-to-open (φ_{CO}) reaction of 1.4×10^{-3} and a quantum yield for the open-to-closed reaction (φ_{OC}) of 6.5×10^{-2}. The mismatch is at least an order of magnitude less than for BTE. This has profound influence on an AMOL exposure using cPTE as the photochromic species in the AML.

8.3 Simulation Results

In order to simulate the effect of the better quantum yield matching of the cPTE molecule, compared to BTE, the simulation model used previously in Chapters 4-7 was reused and the case for using cPTE was simulated. Fig 8.2 shows the results of FEM simulations using conventional AMOL exposure scheme, with the AML fitted with parameters for cPTE. For the cPTE, the values for the molar absorptivity used are as follows: $\varepsilon_{1O} = 3240\, m^2/mol$, $\varepsilon_{1C} = 1920\, m^2/mol$, $\varepsilon_{2O} = 0$, $\varepsilon_{2C} = 960\, m^2/mol$. Initial concentration of photochromes and thickness of the photochromic layer are kept same. It can be seen in Fig. 8.2 (a) that the intensity ratio required to pattern features below 50 nm is about 500-1000 whereas this was usually 3000 to 6000 and higher for the BTE. This means that if the exposing (λ_1) intensity is kept fixed, one needs about 1/3rd to 1/4th the intensity in the confining (λ_2) beam to produce the same confinement effect. The effective PSF at the bottom of the AML for the cPTE is shown

in Fig. 8.2 (b) with the FWHM decreasing for higher values of the intensity ratio. This fact is illustrated additionally in Fig. 8.2 (c) and (d), which show the results of the FEM simulation predicting the intensity of λ_1 and the distribution of the photochromic species in the closed form for cPTE and BTE at an intensity ratio of 400 and 500 respectively. Clearly, even at lower intensity ratios, cPTE offers better confinement.

It can be seen that good confinement of the exposing beam can be achieved even at a quarter of the intensity ratio required for similar confinement with the BTE. This is an ideal situation in realizing low-power portable super resolution AMOL systems. The primary factor in achieving this is the better matched quantum yield values of cPTE. Also, it must be noted that for BTE $\varepsilon_{1C} < \varepsilon_{2C}$, whereas for cPTE $\varepsilon_{1C} > \varepsilon_{2C}$ which means that the confining beam is absorbed less in the closed form regions, thereby helping to maintain better confinement and hence overall better contrast at a lower intensity ratio. Also, the absorption contrast at the exposing wavelength which is dependent on the molar absorptivity ratio at λ_1, i.e. $\varepsilon_{1C}/\varepsilon_{1O}$ has a higher value in cPTE (0.59) compared to that in BTE (0.3) and hence as indicative in equation (1), provides for better confinement at a lower intensity ratio.

8.4 Experimental Results

This section presents some experimental results of patterning using a cPTE based AML. The cPTE is dissolved at 96% by weight in a 3% by weight PMMA-in-Anisole solution and spun onto the photoresist layer. Since Anisole adversely affects photoresists, a thin (~ 8 nm) layer of polyvinyl alcohol (PVA) was used as a barrier layer. In the future, suitable combinations of photoresist and cPTE based AML must be identified to remove the barrier layer. However, at present, the merits of the cPTE

outweigh the demerits of the presence of the barrier layer. The optical set up and all sample processing steps are the same as described in [2]. Fig. 8.3 shows some experimental results of lithographic patterning with an AML composed of cPTE molecules. Fig. 8.3 (a) shows scanning electron micrographs of patterned lines. Fig. 8.3 (b) shows the linewidth scaling trend that matches closely with the simulations. Lastly, Fig. 8.3 (c) large area patterning.

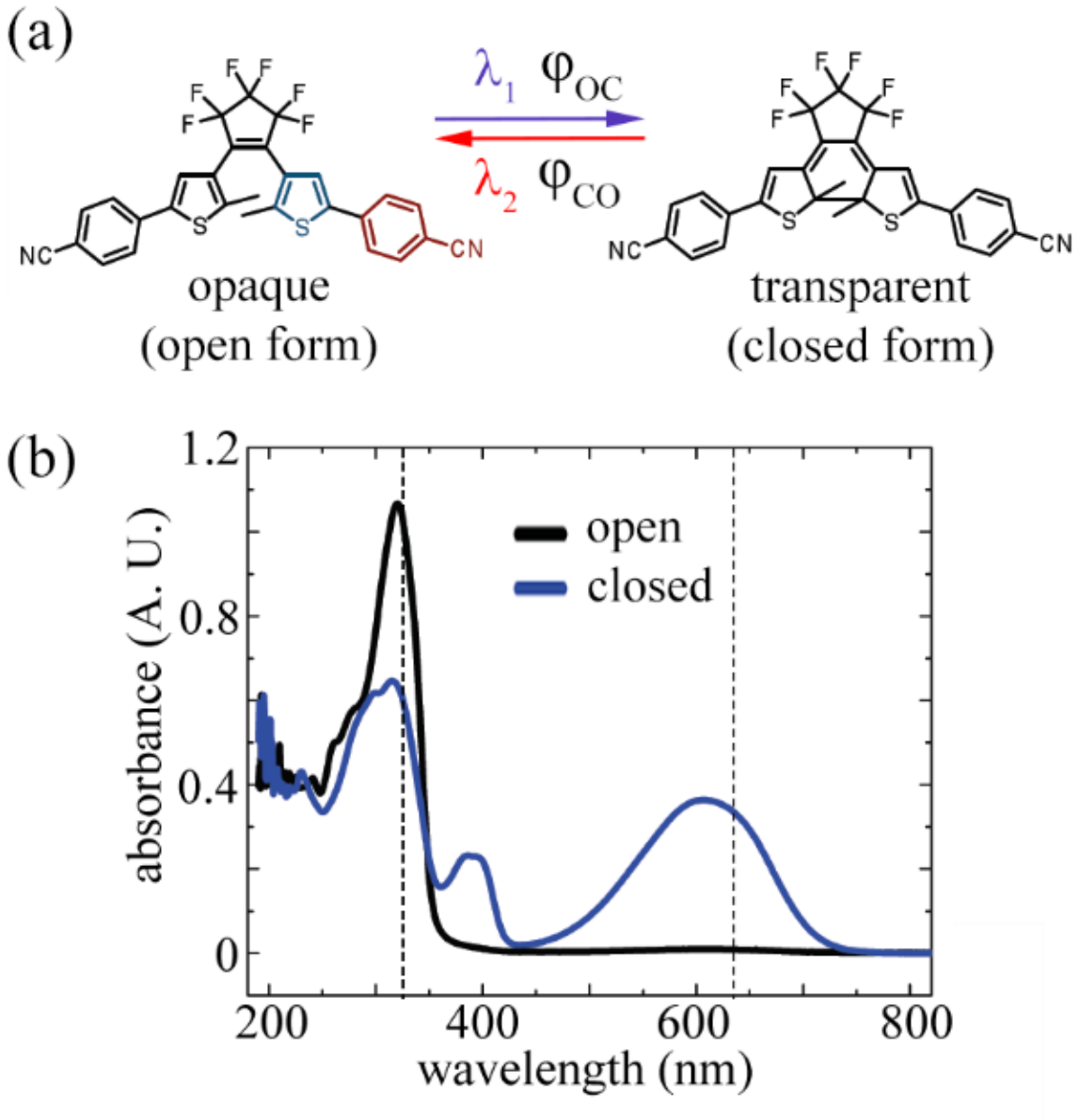

Fig. 8.1: The cPTE molecule. (a) Structures of the open and closed forms of the cPTE molecule. (b) UV-Vis spectrophotometry data of the cPTE measured for a 92% solution by weight of cPTE molecules dispersed in polystyrene.

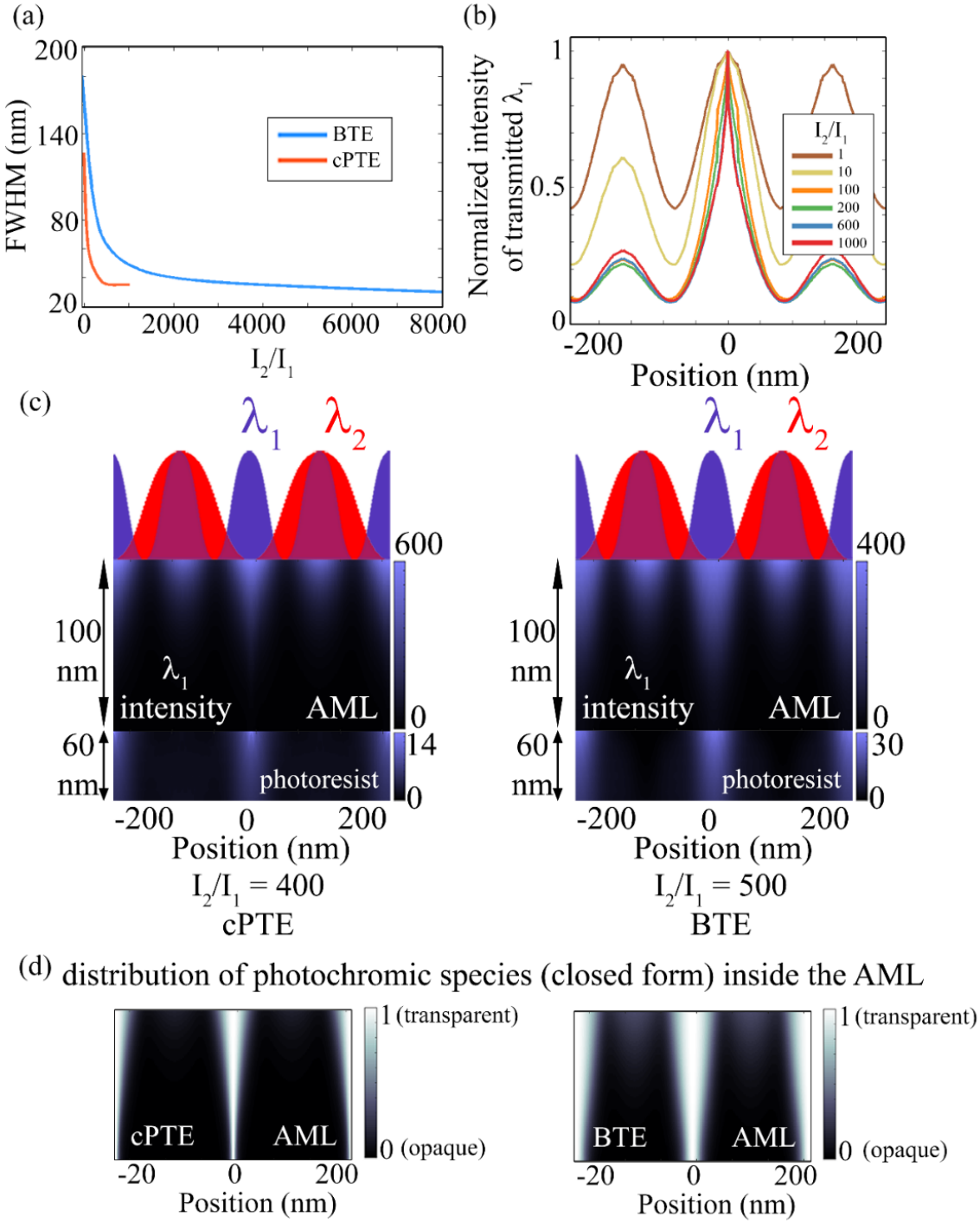

Fig. 8.2: Simulation results. (a) Results of the FEM simulation showing the scaling trend for cPTE compared to BTE. (b) AMOL PSF for cPTE with variation in FWHM versus increasing intensity ratio. (c) Results of FEM simulation showing the light field distribution inside the AML for the exposing beam for an AML composed of cPTE at intensity ratio 400 and for an AML composed of BTE at an intensity ratio of 500. (d) Results of FEM simulation showing the distribution of photochromic species inside the AML for the same illumination scheme as in (c).

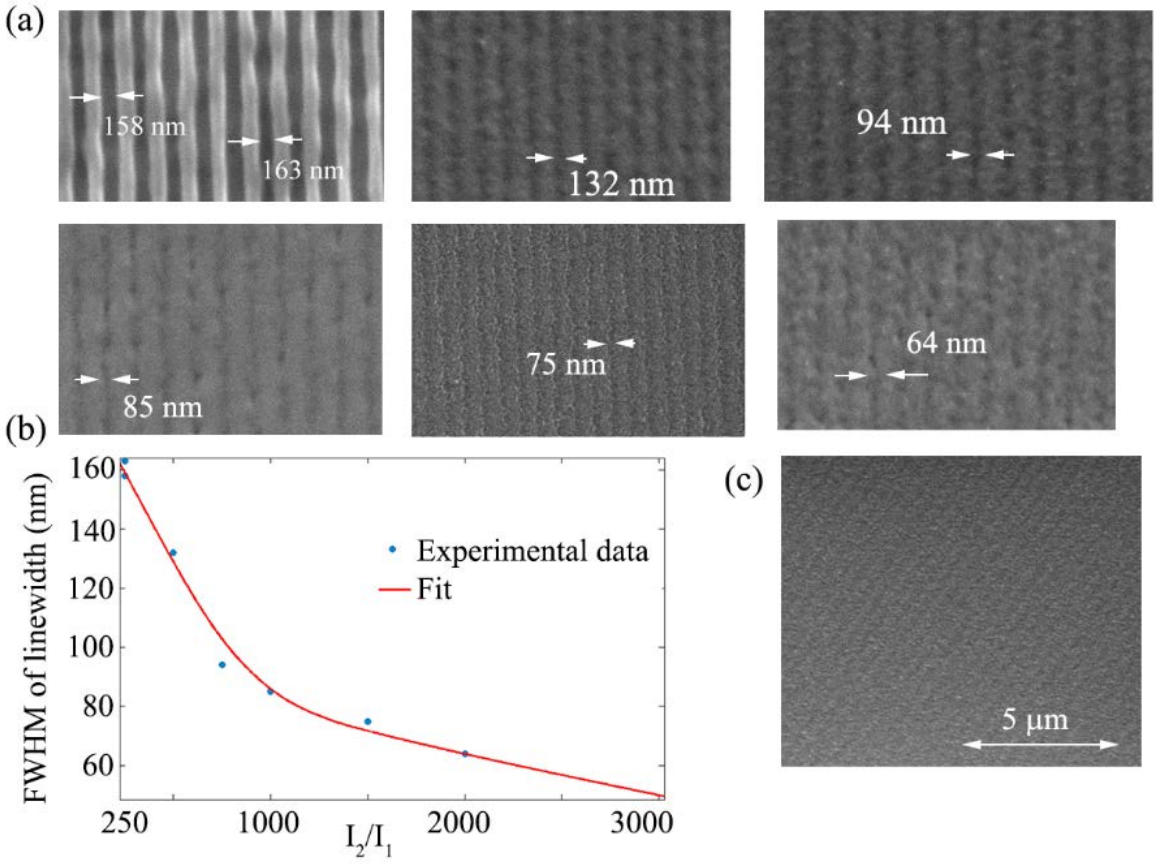

Fig. 8.3: Experimental results. (a) Lithographic patterning results using cPTE based AML. (b) Scaling trend. (c) Large area patterning.

8.5 References

1. A. Majumder, P. J. Helms, T. L. Andrew, and R. Menon, "A comprehensive simulation model of the performance of photochromic films in absorbance-modulation-optical-lithography," *AIP Advances*, vol. 6, 035210, Mar. 2016, pp. 035210-1-8.

2. A. Majumder, F. Masid, B. J. Pollock, T. L. Andrew and R. Menon, "Barrier free absorbance modulation for super-resolution optical lithography," *Opt. Exp.*, vol. 23, no.9, Apr. 2015, pp. 12244-12250.

CHAPTER 9

OPTICAL SETUP FOR PERFORMING TWO-DIMENSIONAL OPTICAL PATTERNING USING AMOL

This chapter presents the details of an optical setup that is designed and built to perform arbitrary two-dimensional patterning using the AMOL process.

9.1 Introduction

In order to realize the full potential of AMOL to patterning subdiffraction features it is necessary to extend the approach to patterning arbitrary two-dimensional features. So far, the work described in the previous chapters dealt with optical setups that were only capable of generating periodic patterns. In this chapter, an optical setup is designed, built and characterized that may be used to pattern aperiodic features. The optical setup and important components of the setup are discussed in detail with system-level descriptions.

9.2 Description of Optical Setup

The approach to super-resolution nanoscopy as adapted by STED [1-3] is the primary inspiration to the method of realizing aperiodic patterning with AMOL. A schematic of the optical setup is shown in Fig. 9.1. The beam from a Kr-ion laser (λ_2 at 647 nm) was spatially filtered and the collimated using a collimating lens. The

beam was then guided through a series of mirrors to pass through first a vortex phase plate with a 2π phase shift that is responsible for imparting a spiral phase to the beam and secondly through a 4f correlator system made using two lenses (Lenses 1 and 2). The 4f correlator is responsible for imaging the vortex phase plate (VPP) on to the back focal plane of the objective lens. The beam also passed through a beam splitter that split the beam into two arms. This beam splitter was also responsible for collecting the reflected light from the sample plane and imaging it on to a charge coupled device (CCD) sensor with the help of a third lens (Lens 3) in order to monitor the focusing of the beam. The exposing beam was from a He-Cd laser (λ_1 at 325 nm) as shown in Fig. 9.1 or from a UV LED (λ_1 at 325 nm) as shown in Fig. 9.2. Either source is appropriate for the system. Both the sources were tested to work effectively. In the case that the HeCd laser was used the beam was spatially filtered and then collimated using a collimating lens. In either case, the λ_1 beam was guided by a set of mirrors and onto a dichroic mirror. The λ_2 beam was also in turn guided on to the same dichroic mirror. The dichroic mirror allows the λ_2 beam to be transmitted while reflecting the λ_1 beam by 90 degrees. Therefore, the two beams are combined. The system was then iteratively aligned following well-established procedures [3, 4]. The combined beams were passed through an objective lens (Olympus UMPLAN FLUAR 40x 0.5 NA) and focused on the sample plane. The sample was mounted onto a three-axis stage that was controlled by a software developed in LabView [5] to perform the patterning. In the next sections, the important elements of the set-up will be discussed in detail.

9.3 Three-Axis Scanning Stage

The three-axis scanning stage used in the setup is the Nano3D 200 from Mad City Labs [6] as shown in Fig. 9.3 (a). It has a total motion range in the three axes for 200 μm per axis and a movement resolution of 1 nm. The stage is controlled by a closed loop piezoelectric control circuit and made of an aluminum body to lend stability. It is also extremely compact, and can be integrated with a coarse alignment stage fitted with micrometer actuators for coarse alignment of the sample with the beams as shown in Fig. 9.3 (b). The fact that the stage motion is addressed by a closed loop piezoelectric circuit allows the stage to maintain high stability and achieve nanometer movement resolution.

A software with user interface was written in LabView to control the movement of the stage and integrate it with shutters placed in the paths of the two beams to synchronize the stage movement with the on and off switching of the two beams to write patterns in a raster dot-matrix fashion. The user interface of this LabView software is shown in Fig. 9.4. The user can load any design using this interface and the design is converted to pixels and x-and-y motion of the stage. Then the user is allowed to specify the exposure time and step size of the pixels and start the exposure. The position of the stage in the x and y axes is continuously monitored and displayed in real time in graphical method in the two position indicator graphs on the right half of the interface as shown in Fig. 9.4.

9.4 Dichroic Mirror

A dichroic mirror is used to combine the two beams as shown in Fig. 9.1 and Fig. 9.2. The specific mirror used is the DMLP505 Long Pass dichroic mirror from Thorlabs [7]. It has above 90% transmission in the 505-750 nm wavelength range and above

50% reflection in the 300-350 nm range and close to 100% reflection in the 350-500 nm range. The cutoff wavelength is 505 nm. Hence, it was ideally suited for our application. The reflectance and transmission data for the mirror is shown in Fig. 9.5 [7].

9.5 Optical Vortex

The optical null that is required in the confining beam (λ_2) in AMOL was created using a vortex phase plate (VPP). When a plane wave passes through a VPP, the plane wave is twisted along its axis of propagation and when this is focused with a lens, such as the objective lens in the setup, the focused spot has an optical null at the center. This is called an optical vortex. The idea that it is possible to create phase singularities in optical waves was first reported in the seminal paper by John Nye and Michael Berry [8] in 1974. Since then an entire field of optics has focused its research efforts into this type of optical phenomenon. Since the optical null at the center of the spot is of zero intensity and is caused by a phase singularity, this subfield of optics research is also called "singular optics." There has been a number of publications over the years on different techniques of producing this unique phenomenon and characterizing the structure of optical vortices [9-15]. Of these several techniques that have been reported in the past, the use of a spiral phase plate or a vortex phase plate (VPP) is adapted in this work.

A VPP works by means of converting a plane wavefront into one that spirals continuously around the axis of travel of the wave. At the very center of the beam, the phase is singular and "since any nonzero optical amplitude must have a well-defined phase, the axis of the vortex is always dark" [16]. After passing through the VPP, light is twisted around its axis so that the light waves at the center cancel each other out

creating a dark null. When projected on a surface or imaged using a lens, this has the appearance of a ring with a dark node at the center. A VPP requires a maximum phase step of 2π. This corresponds to a maximum depth d given by [17]:

$$d = \frac{\Delta l_{max}}{(2\pi)}\ \varphi \qquad (9.1)$$

where Δl_{max} is the thickness of the phase step that provides 2π phase shift and φ is the azimuthal angle. Also, Δl_{max} corresponding to a 2π phase shift for the wave when traveling inside a medium of refractive index n and surrounding medium as air, is related to the wavelength of light and the refractive index n by the following equation

$$\Delta l_{max} = \frac{\lambda}{(n-1)} \qquad (9.1)$$

For a twisted light wave, the number of twists it goes through for one wavelength travel is defined as its topological charge. This number is always an integer and can be negative or positive depending on the direction of the twist. The size of the null increases with the value of the topological charge.

9.6 Optical Vortex Formation Using Vortex Phase Plate

A phase step of 2π that is required to produce an optical vortex is shown in Fig. 9.6 (a) and (b). This can be realized as a variation in height of a material of refractive index other than air such that the maximum height step corresponds to the maximum phase shift of 2π. However, it is difficult and almost impossible to fabricate a material with such a smooth height gradient. So instead, this height gradient is discretized into a number of steps like a spiral staircase as shown in Fig. 9.6 (c) and (d) and this can be fabricated by prevalent microfabrication techniques like grayscale photolithography. Of course, it is obvious that the more number of steps, the closer

this approximated model gets to the ideal case. The pattern in Fig. 9.6 (c) can be used as a mask in a grayscale photolithography exposure tool and easily fabricated.

A phase step of 2π that is required to produce an optical vortex is shown in Fig. 9.6 (a) and (b). This can be realized as a variation in height of a material of refractive index other than air such that the maximum height step corresponds to the maximum phase shift required. In order to fabricate a VPP corresponding to the height profile as shown in Fig. 9(d), we used the μPG101 Pattern Generator from Heidelberg Instruments GmbH. This instrument is a direct laser writer photolithography tool that is capable of grayscale lithography. The substrate used is quartz. The substrate is cleaned using RCA1 and Piranha cleaning techniques. Then a monolayer of HMDS and a 2 μm thick layer of positive photoresist with refractive index ~ 1.68 at 647 nm are spun on. This sample is then exposed to the pattern shown in Fig. 9(d). The laser writer varies its dose as per the gray level at different locations of the pattern. Therefore, the photoresist gets a variation in dose and once developed using standard 352 developer, produces the steps of varied heights. The process of grayscale photolithography is shown as a schematic in Fig. 9.7 (a).The optical micrograph and atomic force micrograph of the fabricated VPP are shown in Fig. 9.7 (b). The atomic force micrograph clearly shows a maximum step height difference of 1 μm which corresponds to 2π phase shift in this case.

The VPP once incorporated into the optical setup can be tested for behavior. A number of tests for imaging the vortex are shown in Fig. 9.8. In the first case, a high dynamic range (HDR) composite photograph of the optical vortex projected from the objective lens is shown in Fig. 9.8 (a). The optical null can be clearly observed. In Fig. 9.8 (b), a photograph of the optical vortex when projected onto a screen after being passed through a spatial filter is shown. Again, the optical vortex and the sinc function

envelope due to spatial filtering can be seen. Lastly, the vortex is imaged on to a CCD using the objective lens. This is shown in Fig. 9.9 (a). This imaging is done slightly away from the focus as the light intensity at the focus is too high and saturates the CCD sensor. Intensity cross-sections along both x and y axis are shown in Fig. 9.9 (b) and (c), respectively, and a 3D reconstruction of the intensity distribution is shown in Fig. 9.9 (d). All of these images conclusively show the successful creation of an optical vortex of high quality.

9.7 Examples of Patterning

In this section, some preliminary results of patterning with this system are presented. Fig. 9.10 (a) shows some patterns that were generated using this setup, without the AMOL process and using only photoresist and UV illumination. This proves the successful patterning ability of the system, though the size of the patterns is not very small. Fig. 9.10 (b) shows some isolated dots that were produced using this system and AMOL with the samples and processes as mentioned in [18].

9.8 Conclusions and Future Work

This chapter presented the design and construction of an optical system that is capable of patterning arbitrary aperiodic 2D patterns. In the future, it may be readily integrated with the AMOL system to pattern subdiffraction feature sizes.

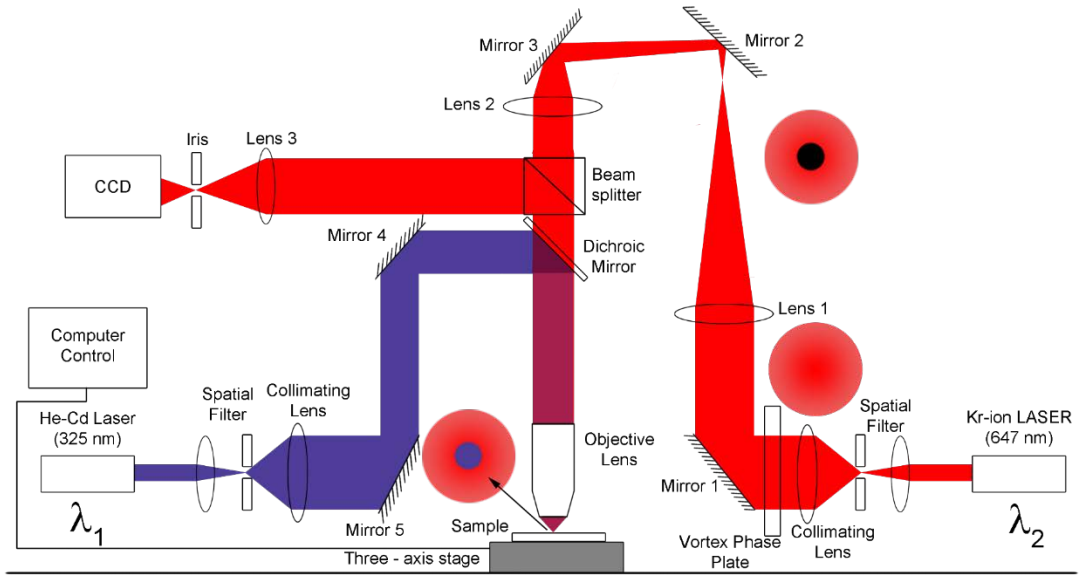

Figure 9.1: Optical setup to perform aperiodic two-dimensional AMOL exposures.

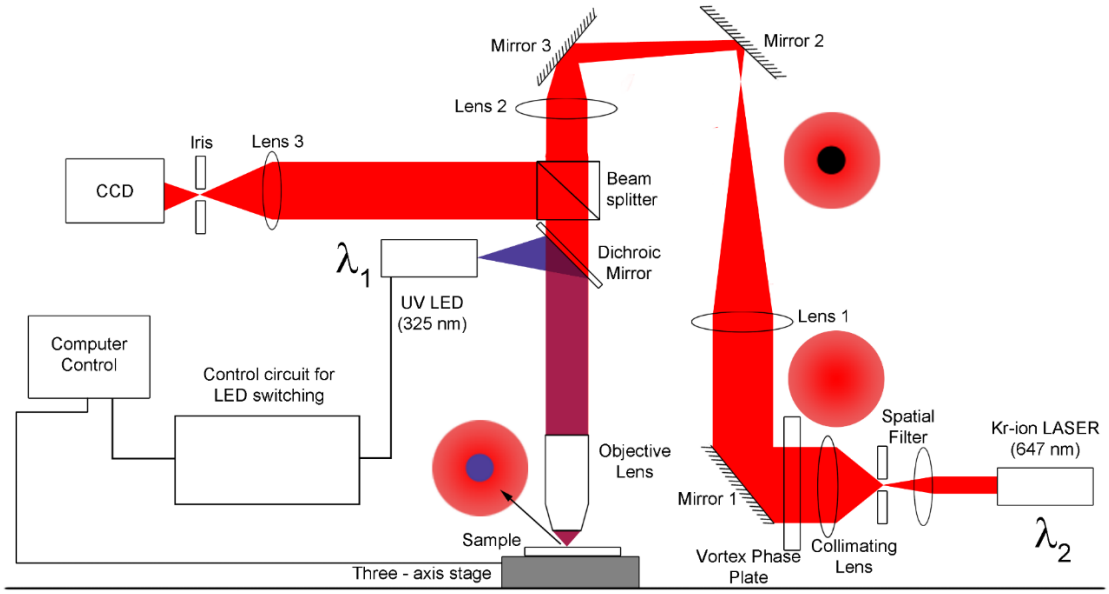

Figure 9.2: Optical setup to perform aperiodic two-dimensional AMOL exposures. Here the λ_1 source has been replaced by a UV LED and its accompanying control circuit, in place of the HeCd laser as shown in Fig. 9.1.

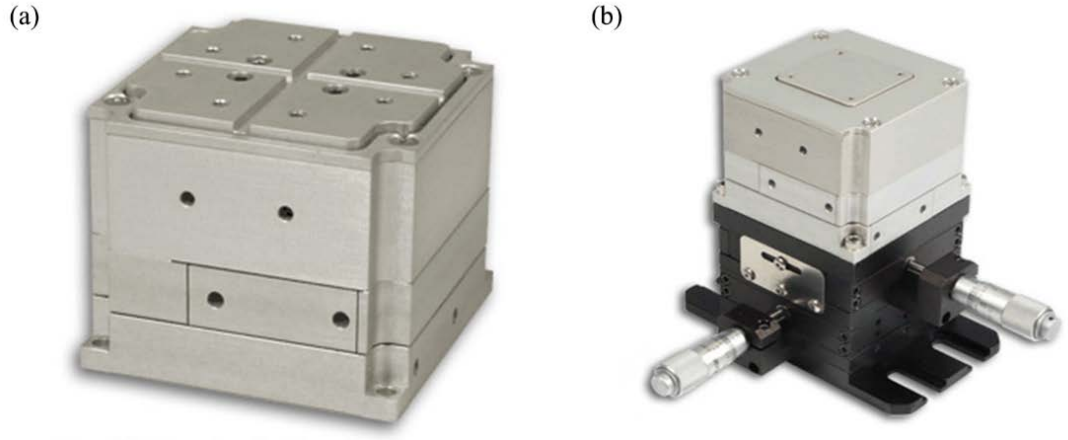

Figure 9.3: Three-axis stage. (a) Three-axis scanning stage from Mad City Labs [6] – the Nano3D 200. (b) Integration of the stage with a second stage that is fitted with manually operated micrometer actuators for coarse alignment.

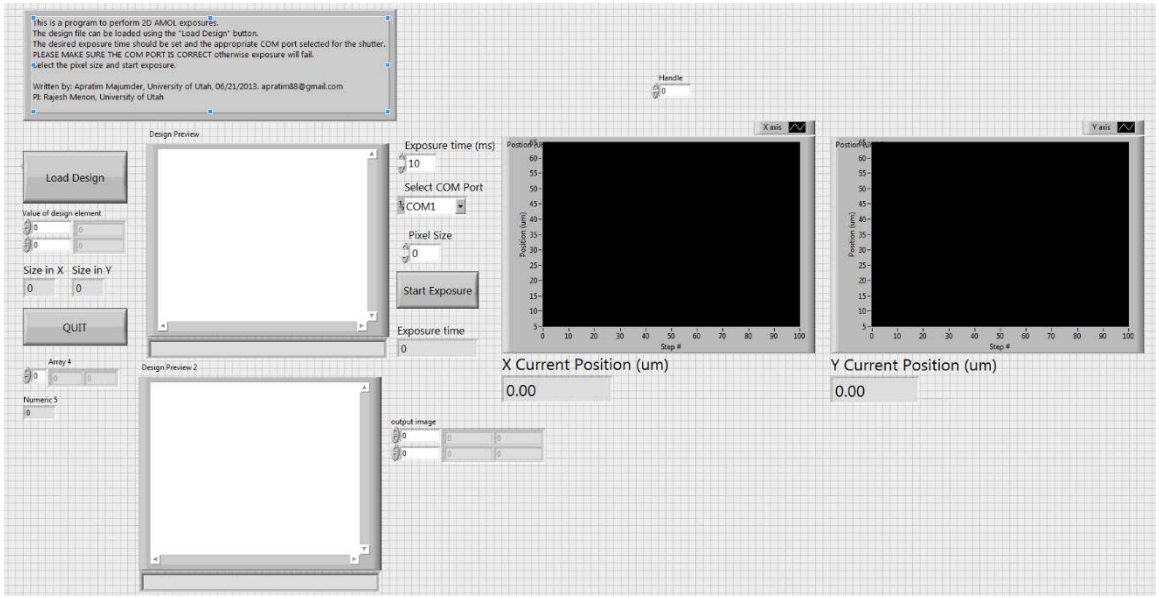

Figure 9.4: User interface of software written in LabView to perform two-dimensional AMOL exposures.

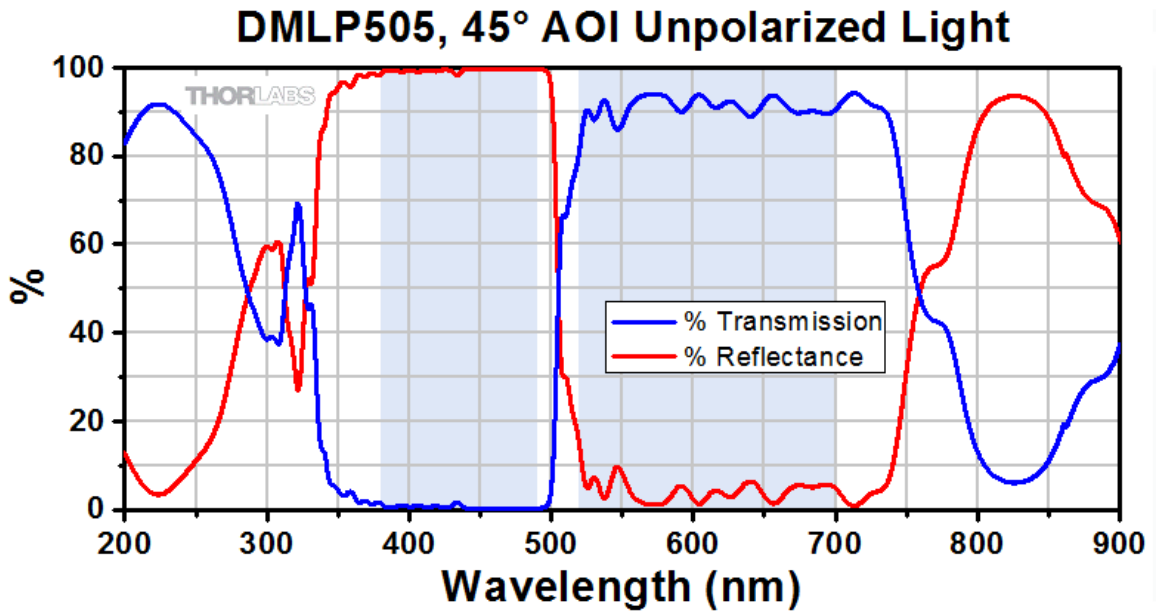

Figure 9.5: Reflectance and transmission data for the DMLP505 dichroic mirror from Thorlabs [7].

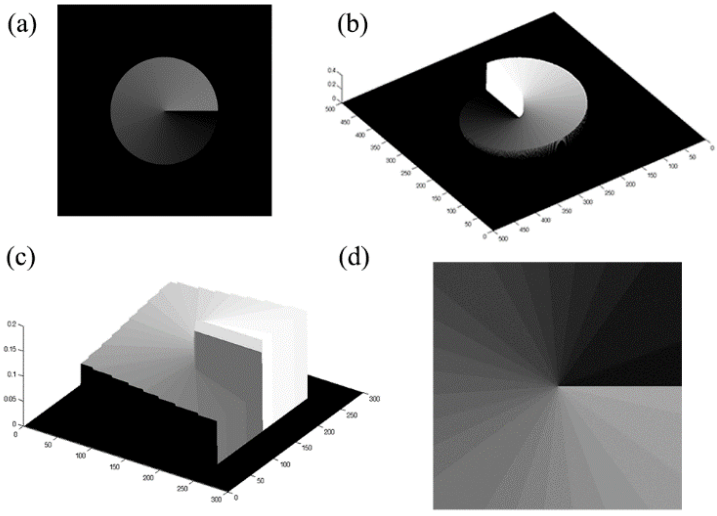

Figure 9.6: Vortex phase plate. (a) Ideal spiral height step of a VPP. (b) 3D representation of (a). (c) Discretized approximated version of (b). (d) 2D representation of (c).

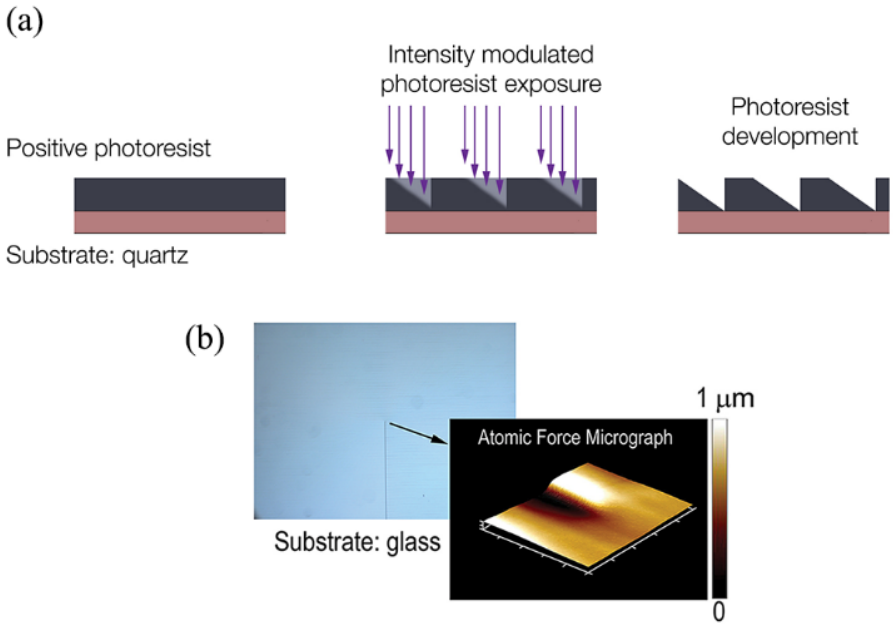

Figure 9.7: Fabrication of VPP. (a) Schematic showing the process of producing varied heights in photoresist using grayscale photolithography. (b) Optical micrograph and atomic force micrograph of the fabricated VPP.

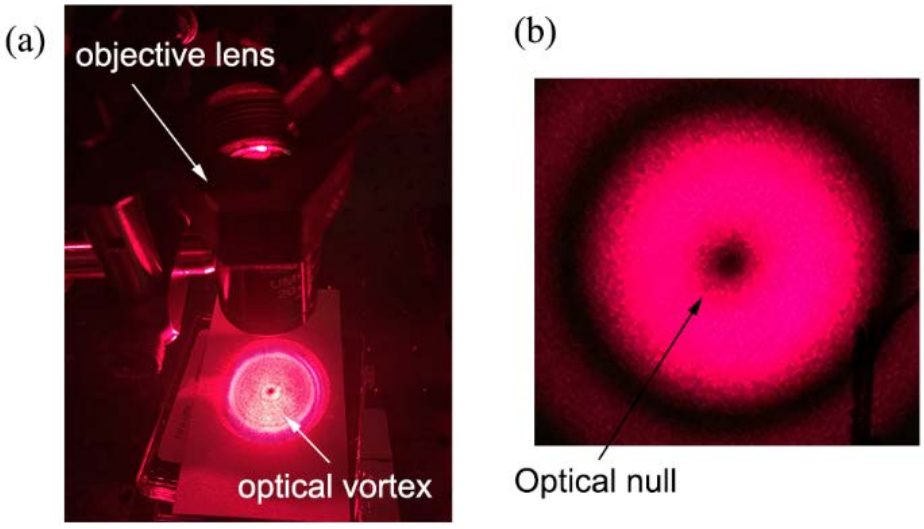

Figure 9.8: Optical null creation. (a) High dynamic range (HDR) composite photograph of the optical vortex projected from the objective lens. (b) Optical vortex projected onto a screen after being passed through a spatial filter.

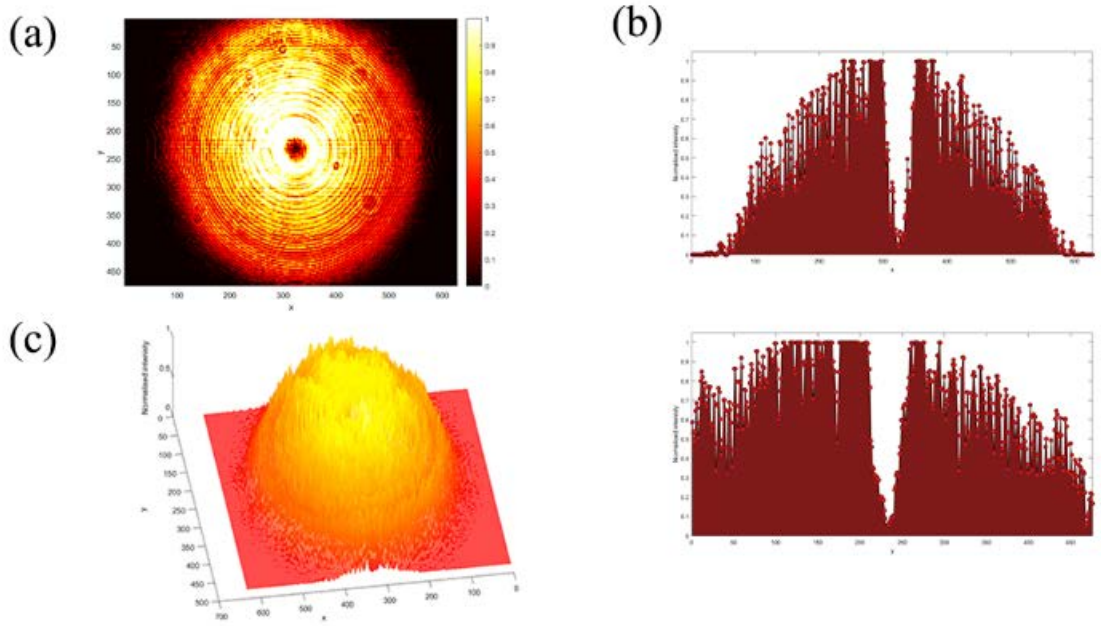

Figure 9.9: Optical null analysis. (a) Optical vortex imaged on to a CCD using the objective lens slightly away from the focus. (b) Intensity cross-sections along x and y axis. (c) 3D reconstruction of the intensity distribution.

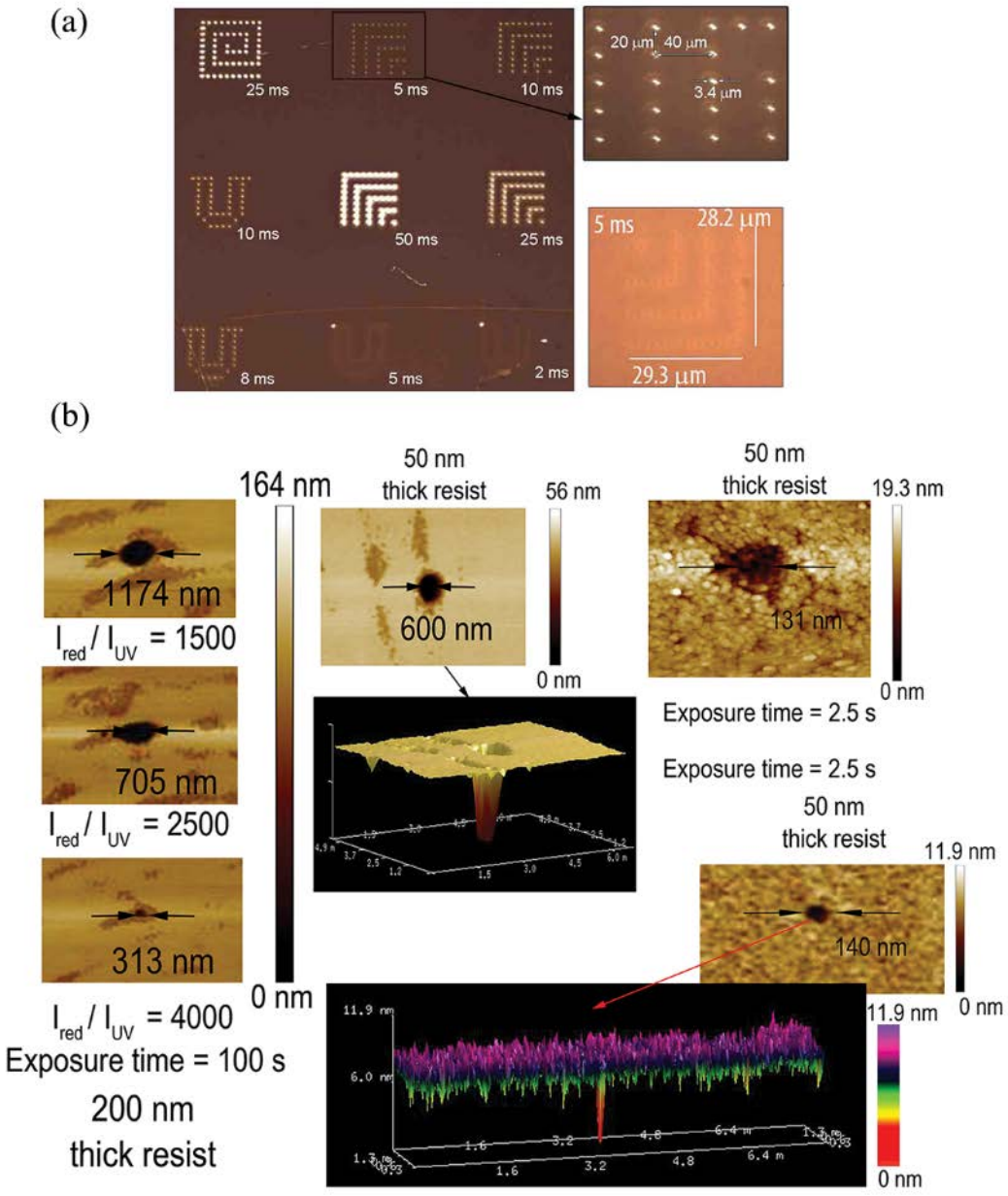

Figure 9.10: Experimental results. (a) Preliminary 2D patterning without AMOL. (b) Isolated dot patterns recorded in photoresist using this system and AMOL.

9.9 References

1. S. W. Hell, and J. Wichmann, "Breaking the diffraction resolution limit by stimulated emission: Stimulated-emission-depletion fluorescence microscopy," *Opt. Lett.*, vol. 19, no. 11, Jun. 1994, pp. 780–782.

2. D. Wildanger, J. Bückers, V. Westphal, S. W. Hell, and L. Kastrup, "A STED microscope aligned by design," *Opt. Lett.*, vol. 17, no. 18, Aug. 2009, pp. 16100-16110.

3. K. I. Willig, B. Harke, R. Medda, and S. W. Hell, "STED microscopy with continuous wave beams," *Nat. Methods*, vol. 12, 2015, pp. 827-830.

4. M. E. Walsh, "On the Design of lithographic interferometers and their application," Doctoral Dissertation, Massachusetts Institute of Technology, 2004.

5. http://www.ni.com/labview/

6. http://www.madcitylabs.com/nano3d200.html

7. https://www.thorlabs.com/thorproduct.cfm?partnumber=DMLP505

8. J. F. Nye and M. V. Berry, "Dislocations in wave trains," *Proc. Royal Soc. of London, Series A*, vol. 336, no.1605, 1974, pp. 165–190.

9. J. E. Curtis and D. G. Grier, "Structure of optical vortices," *Phys. Rev. Lett.*, vol. 90, no.13, 2003, pp. 133901-1-4.

10. I. D. Maleev and G. A. Swartzlander Jr., "Composite optical vortices," *J. Opt. Soc. Am. B.,* vol. 20, no. 6, Jun. 2003, pp. 1169-1176.

11. F. S. Roux, "Dynamical behavior of optical vortices," *J. Opt. Soc. Am. B.*, vol. 12 no. 7, Jul. 1995, pp. 1215-1221.

12. S. G. Garanin, F. A. Starikov, and Yu. I. Malakhov, "Adaptive optics and optical vortices", *Adapt. Opt. Prog.*, Dr. Robert Tyson (Ed.), InTech, 2012.

13. J. Vickers, M. Burch, R. Vyas, and S. Singh, "Phase and interference properties of optical vortex beams," *J. Opt. Soc. Am. A.*, vol. 25, no. 3, Mar. 2008, pp. 823-827.

14. X. Hao, C. Kuang, T. Wang, and X. Liu, "Effect of polarization on the de-excitation dark focal spot in STED microscopy," *J. Opt.*, vol. 12, no. 11, Oct. 2010, pp. 115707-1-5.

15. N. R. Heckenberg, R. McDuff, C. P. Smith, and A. G. White, "Generation of optical phase singularities by computer-generated holograms," *Opt. Lett.*, vol. 17, no.3, Feb. 1992, pp. 221-223.

16. M. D. Levenson, T. J. Ebihara, G. Dai, Y. Morikawa, N. Hayashi, and S. M. Tan, "Optical vortex masks for via levels," *J. Microlith., Microfab. and Microsyst.*, vol. 3, Apr. 2004, pp. 293. DOI: 10.1117/1.1683304.

17. E. Karimi, G. Zito, B. Piccirillo, L. Marrucci, and E. Santamato, "Hypergeometric-Gaussian modes," *Opt. Lett.*, vol. 32, no. 21, Nov. 2007, pp. 3053-3055.

18. A. Majumder, F. Masid, B. J. Pollock, T. L. Andrew, and R. Menon, "Barrier free absorbance modulation for super-resolution optical lithography," *Opt. Exp.,* vol. 23, no.9, Apr. 2015, pp. 12244-12250.